Unveiling Cosmic Reionisation: Improvements in Understanding Interferometric Systematics

Aman Chokshi
ORCiD 0000-0003-1130-6390

November, 2024

A thesis submitted in complete fulfilment
of the requirements for the degree of

Doctor of Philosophy
Physics
The University of Melbourne

"The story so far:
In the beginning the Universe was created.
This has made a lot of people very angry and been widely regarded as a bad move."

— Douglas Adams, *The Restaurant at the End of the Universe*

Abstract

The Epoch of Reionisation (EoR) spans a critical era in the Universe's past, encompassing the ignition of the first luminous objects which triggered a final phase transition from neutral to its current completely ionised state. Largely unexplored and as of yet undetected, measurements of the EoR will encode a multitude of astrophysical and cosmological tracers, which promise to aid in the unravelling of mysteries surrounding the birth of the first stars and galaxies, their nature, and their influence on the evolution of the Universe. The 21-cm signal from neutral Hydrogen can be leveraged to tomographically map large cosmological volumes, tracing the ionisation morphology of the early Universe. Low-frequency radio interferometers, such at the Murchison Widefield Array (MWA), observe large cosmological volumes and possess the theoretical sensitivity to make a statistical detection of the 21-cm EoR signal. Astrophysical and terrestrial foregrounds dominate the EoR signal by factors exceeding five orders-of-magnitudes, and couple with complex instrumental systematics to impede a detection. Unprecedented precision is required at all levels to unveil the EoR signal; from instrumental understanding to astrophysical modelling. Current measured upper-limits are a couple of orders-of-magnitude higher than cutting-edge EoR models. A first EoR detection is on the horizon.

In this thesis we explore the impact of complex interferometric systematics, in particular primary beam models, on a future EoR detection. We design and implement an experiment to measure the all-sky dual-polarised beampatterns of 14 MWA receiving elements (tiles), using communication satellites. Unexpected inter-tile side-lobe variations were measured at a $\sim 10\%$ level, attributed to a variety of environmental factors. We develop a physically motivated model of beam deformation, and explore their impact on an EoR power spectrum detection and MWA polarisation science. Our simulations indicate that including measured instrumental beams into calibration frameworks could reduce foreground coupling into EoR sensitive measurement modes by factors exceeding ~ 1000, potentially putting a first EoR detection within grasp. We outline the steps required to make our deformed beam calibration framework applicable to measured data, and discuss its impact on the next-generation SKA-Low observatory.

Declaration

This page certifies that:

- This thesis contains only original work towards a Doctor of Philosophy, except where indicated in the preface
- Due acknowledgement has been made in the text to all other material used
- This thesis is fewer than 100 000 words in length, exclusive of tables, figures, bibliographies, and appendices

Aman Chokshi

Preface

Here and henceforth, "the author" refers to Aman Chokshi, the author of this thesis. This thesis is an original work by the author reporting research done alone or in collaboration with other authors. This section provides a chapter-by-chapter summary of the author's contributions and the publication status of all material.

Chapter 1 is an introduction to the history of the Universe, and the Epoch of Reionisation. It is an original work of the author, with editing from N. Barry and R. Webster, and has not and will not be submitted for publication.

Chapter 2 is an introduction to low-frequency interferometry, and the Murchison Widefield Array. It is an original work of the author, with editing from N. Barry and R. Webster, and has not and will not be submitted for publication.

Chapter 3 is based on the published work *A. Chokshi, J. L. B. Line, N. Barry, D. Ung, D. Kenney, A. McPhail, A. Williams, R. L. Webster, Monthly Notices of the Royal Astronomical Society, Volume 502, Issue 2, April 2021, Pages 1990–2004.* It was written primarily by the author, with scientific input and editing from the co-authors. The author was responsible for data acquisition and data analyses. All figures and tables are the work of the author.

Chapter 4 is based on the published work *A. Chokshi, N. Barry, J. L. B. Line, C. H. Jordan, B. Pindor, R. L. Webster, Monthly Notices of the Royal Astronomical Society, Volume 534, Issue 3, November 2024, Pages 2475–2484.* It was written primarily by the author, with scientific input and editing from the co-authors. The author was responsible for generating the simulations and data analyses. All figures and tables are the work of the author.

Chapter 5 is based on a draft of work to be published *A. Chokshi, N. Barry, B. Pindor, J. L. B. Line, C. J. Riseley, X. Zhang, R. L. Webster, Publications of the Astronomical Society of Australia.* It was written primarily by the author, with scientific input and editing from the co-authors. The author was responsible for generating the simulations and data analyses. All figures and tables are the work of the author.

Chapter 6 summarises the work in the previous chapters. It includes some exploratory future directions for the work in this thesis. It was written by the author, with editing from N. Barry and R. Webster.

The author also contributed to eleven other publications during their PhD candidature, which are not included for examination in this thesis but are listed here for completeness:

- *Prabhu, K., Raghunathan, S., Millea, M., ... **Chokshi, A.**, ... et al. [SPT Collaboration], Testing the ΛCDM Cosmological Model with Forthcoming Measurements of the Cosmic Microwave Background with SPT-3G, The Astrophysical Journal, Volume 973, Number 1, September 2024.*

- *Gupta, A., Trott, C. M., ... Chokshi, A. [12 authors], MOSEL survey: Spatially offset Lyman-continuum emission in a new emitter at z=3.088, The Astrophysical Journal, Volume 973, Number 2, Septemer 2024.*

- *Coerver, A., Zebrowski, J. A., Takakura, S., ... **Chokshi, A.**, ... et al. [SPT Collaboration], Measurement and Modeling of Polarized Atmosphere at the South Pole with SPT-3G, arXiv:2407.20579, July 2024*

- *C. J. Riseley, E. Bonnassieux, T. Vernstrom, T. J. Galvin, **A. Chokshi**, ... et al [24 authors], Radio fossils, relics, and haloes in Abell 3266: cluster archaeology with ASKAP-EMU and the ATCA, Monthly Notices of the Royal Astronomical Society, Volume 515, Issue 2, September 2022, Pages 1871–1896.*

- *N. Barry, **A. Chokshi**, The Role of the Instrumental Response in 21 cm Epoch of Reionization Power Spectrum Gridding Analyses, The Astrophysical Journal, Volume 929, Number 1, April 2022.*

- *M. Rahimi, B. Pindor, ... **A. Chokshi**, ... et al. [31 authors], Epoch of reionization power spectrum limits from Murchison Widefield Array data targeted at EoR1 field, Monthly Notices of the Royal Astronomical Society, Volume 508, Issue 4, December 2021, Pages 5954–5971.*

- *C. M. Trott, C. H. Jordan, ... **A. Chokshi**, ... et al. [32 authors], Constraining the 21 cm brightness temperature of the IGM at z = 6.6 around LAEs with the murchison widefield array, Monthly Notices of the Royal Astronomical Society, Volume 507, Issue 1, October 2021, Pages 772–780.*

- *S. Yoshiura, B. Pindor, ... **A. Chokshi**, ... et al. [32 authors], A new MWA limit on the 21 cm power spectrum at redshifts 13-17, Monthly Notices of the Royal Astronomical Society, Volume 505, Issue 4, August 2021, Pages 4775–4790.*

- ***A. Chokshi**, J. L. B. Line, B. McKinley, EMBERS: Experimental Measurement of BEam Responses with Satellites, The Journal of Open Source Software, November 2020*

- *Z. Zheng, J. C. Pober, ... **A. Chokshi**, ... et al. [30 authors], The impact of tandem redundant/sky-based calibration in MWA Phase II data analysis, Publications of the Astronomical Society of Australia, November 2020*

- *C. M. Trott, C. H. Jordan, ... **A. Chokshi**, ... et al. [36 authors], Deep multiredshift limits on Epoch of Reionization 21 cm power spectra from four seasons of Murchison Widefield Array observations, Monthly Notices of the Royal Astronomical Society, Volume 493, Issue 4, April 2020, Pages 4711–4727.*

The author was supported by the Melbourne Research Scholarship from the University of Melbourne, which included a fee offset . This research was supported by the Australian Research Council Centre of Excellence for All Sky Astrophysics in 3 Dimensions (ASTRO 3D), through project number CE170100013. This work was supported by resources awarded under Astronomy Australia Ltd's merit allocation scheme on the OzSTAR national facility at Swinburne University of Technology. OzSTAR is funded by Swinburne University of Technology and the National Collaborative Research Infrastructure Strategy (NCRIS). This work was supported by resources provided by the Pawsey Supercomputing Centre with funding from the Australian Government and the Government of Western Australia. This scientific work makes use of the Inyarrimanha Ilgari Bundara Murchison Radio-Astronomy Observatory, operated by CSIRO. We acknowledge the Wajarri Yamatji people as the traditional owners of the Observatory site.

Acknowledgments

I begin by acknowledging the Traditional Owners of the land which has been my home over the past 5 years, and where the majority of this work was performed; the Wurundjeri and Boon Wurrung people of the Kulin Nation, and pay my respects Elders past and present.

The past five years have been a wonderful journey of both personal and scientific growth. It wouldn't have been possible without the support and encouragement of so many of you.

First, I must thank Rachel Webster for her unwavering support and encouragement. She introduced me to the frustrating yet endlessly fascinating field of interferometry, which I've grown to love. She has given me a massive and appreciated amount of freedom and space to grow.

A massive thank you to the most supportive group of postdocs ever – Nichole, Jack and Bart. I arrived clueless, and have learnt so incredibly much from all of you, none of this would have been possible without each one of you. Thank you for constantly indulging my questions, and being the best mentors and colleagues one could hope for.

I'm so grateful to have been a part of the MWA EoR collaboration. Thank you Ronniy, Ruby, Mike, Shintaro, Miguel, Cath and everyone else, for giving me the space to ask and re-ask silly questions till I understood, and never ever feel uncomfortable doing so.

To all the usual suspects on the astro floor: thank you for the curiosity, the friendships, and all the fun times together. Thank you Michele, Christian, Katie and Andrew for your mentoring, encouragement, and interesting chats.

Thank you Pete and Susanne, for welcoming me into your beautiful home.

Thank you, Bethan, for your friendship and the countless happy memories we've made during my time in Australia.

To my loving parents, thank you so much for nurturing curiosity and giving me and Avani so much freedom. For taking us adventuring and shooting-star watching. And thank you Avani, for being the best sister ever. I know you've all always been there for me, no matter what.

Finally, Erin – I'm so happy that we've found each other, and can't wait for our many future adventures together.

Contents

List of figures

List of Tables

Universe shadowed;
starry embers coalesce,
spark curious dreams.

Aman, 2020, *Haiku*

CHAPTER 1

Introduction

Across recorded time, humans have gazed up at the night sky and wondered about their place in the stars. Our curiosity has driven a massive evolution in our understanding of the Universe, teasing from physical observations insights spanning the structure of our Solar System to the very edges of the observable. This thesis represents my small contribution to this growing picture.

The finite nature of the speed of light provides an extraordinary opportunity to peer back into the past, enabling a study into the origin of our Universe. Early observations of galaxies outside the Milky Way revealed that the majority were receding away from us (Hubble, 1929). In fact, Hubble (1929) also showed that recessional velocities were directly proportional to their distance from us, inarguably establishing the fact that the Universe is expanding. Lemaître realised that the Universe must have been smaller at earlier times, which logically meant that there would exist a moment in the past where the entire Universe was compressed into a singularity (Lemaître, 1927) — an idea which marks the birth of Big Bang Cosmology.

This chapter presents a brief history of the Universe, laying the foundation and presenting context for my research. It explores how neutral Hydrogen, the most abundant element in the Universe, can be used as a cosmological tracer to illuminate a critical epoch of the Universe's past which was predominantly dark. Within this darkness primordial matter over-densities coalesced gravitationally, resulting in the ignition of the first luminous objects in our Universe. The resulting intense radiation triggered a universal phase transition of matter from neutral to its current completely ionized state. The Epoch of Reionisation (EoR) spans this critical era, encoding within its light a multitude of astrophysical & cosmological tracers which promise to aid in the unravelling of mysteries surrounding the birth of the first stars and galaxies, their nature, and their influence on the evolution of the Universe.

Chapter 2 discusses low-frequency interferometry, a technique used to build flexible telescopes capable of precisely surveying large cosmological volumes. The rest of this thesis presents new experiments and analysis techniques which improve the prospects of a first detection of cosmological signals from the Epoch of Reionisation.

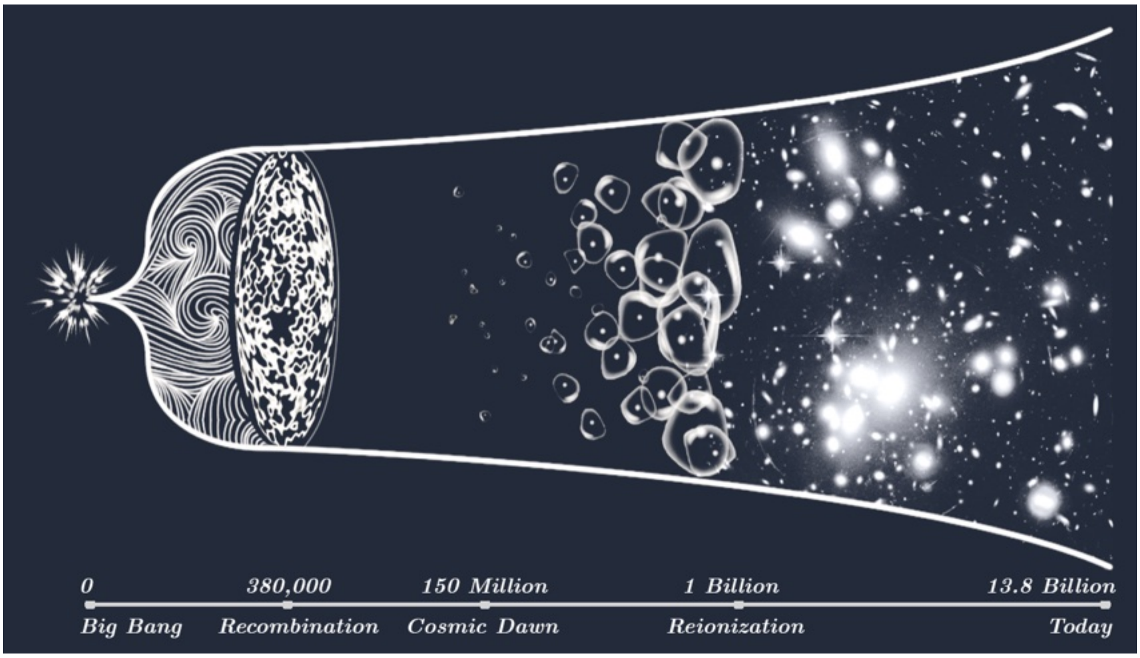

Figure 1.1: An illustration of the history of the Universe. Beginning with the Big Bang to the left, the Universe underwent a period of rapid expansion and cooling. Around $\sim 0.38\,\mathrm{Myr}$ later the Universe had cooled sufficiently for simple nuclei to combine with electrons, resulting in the first phase transition from a opaque ionised plasma to a transparent neutral state. The resulting free streaming photons preserve a snapshot of Universe and is known at the Cosmic Microwave Background. Approximately $\sim 150\,\mathrm{Myr}$ later, at Cosmic Dawn, primordial over-densities have gravitationally coalesced to birth the first luminous sources in the Universe. Ionising radiation produced by these sources expand in bubbles, eventually overlapping to lead to a completely Reionised Universe, approximately $\sim 1\,\mathrm{Gyr}$ after the Big Bang. The period spanning from our Cosmic Dawn through to complete Reionisation is known as the Epoch of Reionisation. In this ionised Universe, through hierarchical mergers or early galaxies, we arrive at our local Universe, approximately $\sim 13.787\,\mathrm{Gyr}$ after the Big Bang.

1.1. A brief History of the Universe

1.1.1. *The Big Bang & the First Three Minutes*

Our Universe was born in a Big Bang, with hot dense matter and light blooming into existence (see Figure 1.1 for an illustration of key milestones of the Universe). Current best estimates put the cataclysmic birth approximately 13.787 ± 0.002 Gyr ago (Planck Collaboration et al., 2020). Within the first fraction of a second it experiences an exponential inflation, resulting in the Universe cooling adiabatically. A mere three minutes later, Big Bang Nucleosynthesis (Alpher et al., 1948) has formed the primary building blocks of the present Universe; the nuclei of Hydrogen, Helium and Lithium. At this stage, the Universe consists of a hot dense soup of photons, protons, neutrons, and electrons. Photons are strongly coupled with electrons via Thomson Scattering due to the high density of the Universe, and the tiny cross-section of scattering. In this energetic and opaque plasma ($k_B T \gg 13.6$eV), any neutral atoms which form are almost immediately dissociated by interactions with photons. The Universe continues expanding and cooling adiabatically, with constantly decreasing photon-electron scattering (due to reduced density and increased mean-free paths), also increasing the longevity of any neutral atom formed.

1.1.2. *Recombination & the Cosmic Microwave Background*

Approximately ≈ 0.38 Myr after the Big Bang, at redshift $z \simeq 1100$*, a critical energy density threshold is achieved ($k_B T \leq 13.6$eV). Neutral Hydrogen atoms which form now persist without being dissociated. This critical milestone in the Universe's past is somewhat confusingly dubbed the "Epoch of Recombination"† (see Figure 1.1). With the comprehensive capture of free electrons by atomic nuclei, the Universe undergoes a rapid phase transition for completely ionised to neutral. This process also frees the photons from their incessant Thomson scattering, enabling them to free stream through the Universe. This relic radiation preserves a precious snapshot of the thermal state of the Universe at the so called "surface of last scattering", when photons decoupled from matter. These photons are redshifted through cosmological expansion and can now be observed at microwave wavelengths as the Cosmic Microwave Background (CMB) (Kamionkowski & Kosowsky, 1999). The existence of this isotropic blackbody radiation is one of the pillars of the Big Bang model, as it implies that photons and baryonic matter existed in a highly interacting thermal state earlier. First detected by Penzias & Wilson (1965), it has now been characterised to have an extremely uniform temperature across the sky $T_{\mathrm{CMB}} = 2.72548 \pm 0.00057$ K (Fixsen, 2009), with spatial temperature anisotropies at the $1/10^5$ level (Planck Collaboration et al., 2016). These minute fluctuations in the nearly uniform CMB are a result of quantum fluctuations in the energy-matter field of the early Universe. These primordial fluctuations are further distorted via

*Redshift (z) serves as a measure of cosmological time. z indicates the factor by which emitted radiation's wavelength is *increased*, due to cosmological expansion. Higher values of z are further in the past, and thus experience larger redshifts. Radiation from the CMB ($z = 1100$) is observed at wavelengths 1101 times longer than those emitted.

†This epoch actually represents the first combination of these particles into stable atoms, in the standard Big Bang model.

interactions with matter along the way to the observer.

1.1.3. The Dark Age, Cosmic Dawn & Reionisation

Post recombination, the Universe enters a period of darkness and contains primarily Hydrogen, with traces of Helium and other heavier elements. At the start of this "Dark Age" the matter distribution is almost homogeneous, exhibiting small fluctuations in density correlated with observed CMB anisotropies. Over the next $\sim 150\,$Myr, regions of above-average densities gravitationally attract matter from neighbouring under-dense regions. This gravitational coalescence around primordial matter fluctuations led to the formation of web-like filamentary structures spanning the cosmos. Giant halos form at intersections within this cosmic web, where gravitational forces can overcome cosmological expansion to finally give birth to the first luminous sources in our Universe. These first stars, black holes and galaxies emitted intense radiation, illuminating the dark ages and heralding a cosmic dawn.

Intense ultraviolet radiation from these first luminous sources propagated into the intergalactic medium (IGM) resulting in bubbles of expanding ionisation. New sources of ionisation came into being while old ionisation bubbles expanded into their neutral surroundings. As first generation ionising sources reached the end of their lives, local pockets of recombination occurred within ionised bubbles due to a lack of an active ionising source. The interaction of old and new ionising sources resulted in a patchy and non-trivial ionisation morphology as the Universe evolves. The eventual overlap of expanding ionisation frontiers led to the inevitable transition of the Universe from neutral to completely ionised. The Epoch of Reionisation (EoR) spans this critical period ($z \approx 20$ to $z \approx 6$), ending almost a billion years after the Big Bang (see Figure 1.1).

The local Universe we observe today consists of a variety of morphologically complex galaxies, organised into large clusters and filaments, embedded in a ionised IGM. The first sources which influenced the formation of this complex structured Universe are suspected to be a combination of first generation stars, quasars and primordial black holes (see e.g. Aghanim et al., 1996; Becker et al., 2015; Mesinger et al., 2015; Madau & Haardt, 2015; Grazian et al., 2018). Many questions surrounding these first sources remain. When and how did they form? And how did they influence the process of reionisation? Irrespective of their nature, their birth changed the nature of the Universe fundamentally, bringing first light to the dark age. Observing the EoR has the scope to revolutionise our understanding of our Universe, and represents one of last major unanswered questions in observational cosmology. Theoretical models of the EoR are advanced and well explored, but remain untested by observations (see Furlanetto et al., 2006; Pritchard & Loeb, 2012, for theoretical EoR models). We also direct curious readers to Park et al. (2019); Mesinger (2019), for reviews on the fundamental astrophysics and cosmology which can be explored using the Epoch of Reionisation signal.

1.2. Neutral Hydrogen as a Cosmological Tracer

Observations of the CMB give us a snapshot of the state of the early Universe around $0.38\,$Myr after the Big Bang ($z \approx 1100$). The next furthest astronomical observation (as of October, 2024) is of JADES-GS-z14-0, a Lyman-break galaxy at $z \simeq 14.32$, almost

290 Myr after the Big Bang (Robertson et al., 2024). Large surveys of galaxies extend out to $z \leq 2$, while systematic surveys of quasars can reach redshifts of $z \leq 3$. A dearth of observations between $3 \leq z \leq 1100$ leave vast volumes of the Universe unexplored (see Figure 1.2).

Fortunately, the most abundant elemental species in the early Universe is neutral Hydrogen (HI), which can be leveraged to map these unexplored cosmological volumes. Neutral Hydrogen emits radiation with a wavelength of 21-cm in the rest frame, which can be cosmologically redshifted to longer wavelengths. This wavelength is in fact one of the most precisely known quantities in astrophysics, measured by Goldenberg et al. 1960 using a Hydrogen maser to 2 parts in 10^{11}! The forbidden spin-flip transition responsible for this radiation arises from the relative spin alignment of the constituent electron and proton, which results in a higher energy triplet state and a lower energy singlet state (Feynman, 1965) (see Figure 1.3). The transition is considered forbidden as it has a mean lifetime of $\sim 10^7$ years, which results in an extremely narrow emission line. Any appreciable concentration of 21-cm radiation implies the existence of massive amounts of neutral Hydrogen due to the almost 10 million year lifetime of the 21-cm spin-flip transition.

The precise correlation between observed wavelength and redshift enables the creation of 3D 21-cm tomographic maps of the Universe. These maps trace the evolution of neutral Hydrogen across Cosmic Dawn and the Epoch of Reionisation (see Figure 1.2), revealing large-scale structure formation, and the growing voids surrounding the first sources of ionisation. This method is in contrast to traditional astronomy which focuses on observing light from stars, galaxies and other relatively small objects of interest. The long wavelength of 21-cm radiation also is not readily absorbed by intervening gas and dust, providing another advantage to 21-cm tomographic mapping as an ideal tool to observe vast volumes of the cosmos.

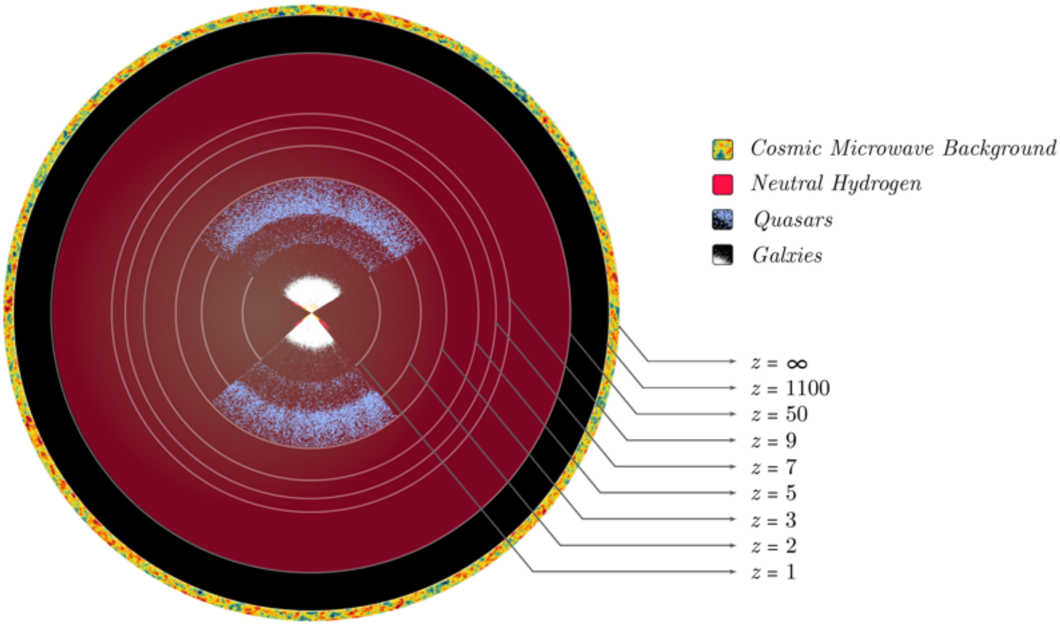

Figure 1.2: How much of the cosmos have we actually observed? This illustration of the Universe to scale shows galactic surveys in white cones near the centre, followed by observations of quasars in purple, and finally bounded by the CMB. Observations of the high-redshift Universe $z \geq 3$ are extremely sparse. Observations of neutral Hydrogen can be leveraged to access orders-of-magnitude higher volumes of the Universe than ever before (see red section). An illustration inspired by Mao et al. (2008), an interpretation by Adrian Liu, using an image of the BOSS survey by Michael Blanton, and the Planck CMB map.

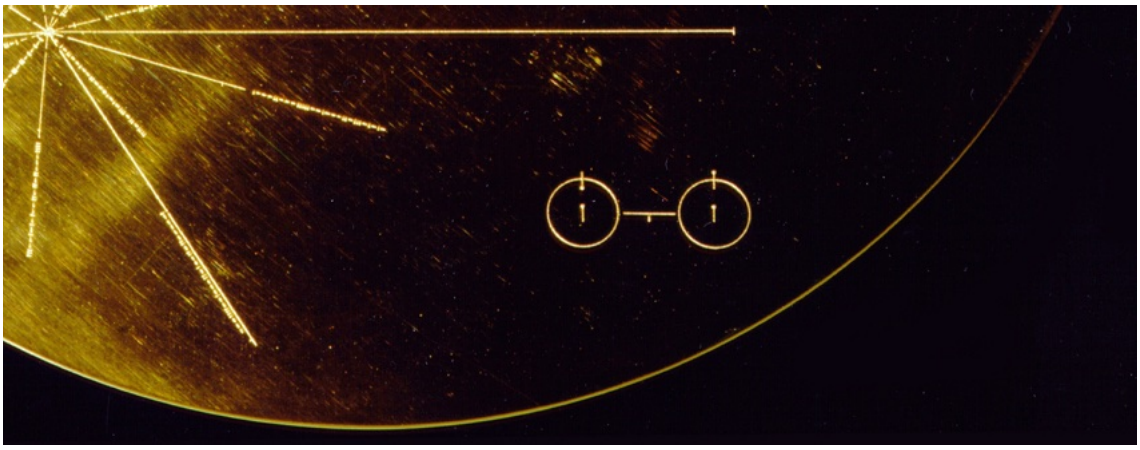

Figure 1.3: The hyperfine transition of neutral Hydrogen, considered so fundamental to the Universe that it was depicted on the Golden Record sent out on the Voyager spacecrafts, and used as the key to decoding all other information from Earth to any intelligent extraterrestrial life form which may find it. This infrequent forbidden spin-flip of a neutral Hydrogen atom emits light with a 21 cm wavelength. Credit: NASA/JPL

1.3. Evolution of the 21-cm signal

A range of physical properties and mechanisms can influence the 21-cm intensity (brightness temperature), including density, velocity, ionisation state, gas temperatures and spin temperatures (Furlanetto et al., 2006). At any redshift, the CMB provided a near isotropic blackbody background for 21-cm radiation emitted from neutral Hydrogen. The variation in brightness temperature due to neutral Hydrogen (HI) in contrast to the background radiation can be quantified by the differential brightness temperature (Morales & Wyithe, 2010) through:

$$\Delta T = 23.8\left(\frac{1+z}{10}\right)^{\frac{1}{2}}[1-\bar{x}_i(1+\delta_x)](1+\delta)(1-\delta_v)\left[\frac{T_s - T_{\rm CMB}}{T_s}\right]\,\mathrm{mK}, \tag{1.1}$$

where $\bar{x}_i$ is the mean ionisation fraction ($\bar{x}_i = 1-\bar{x}_{HI}$), δ is the dark matter density fluctuation, δ_x is the ionisation fraction fluctuation, $\delta_v = (1+z)H^{-1}\partial v_r/\partial r$ is the distortion due to velocity ($\partial v_r/\partial r$ being the radial velocity gradient, and Hubble parameter H), and T_s and T_{CMB} are the spin temperatures of the HI and the temperature of the background CMB radiation. The spin temperature T_s of HI quantifies the ratio of neutral HI atoms in each of the two hyperfine levels of the ground state.

The balance between the process driving reionisation is non-trivial, but can be delineated into important phases where different processes dominate. Figure 1.4 shows the sky-averaged brightness temperature ΔT, from Pritchard & Loeb (2012).

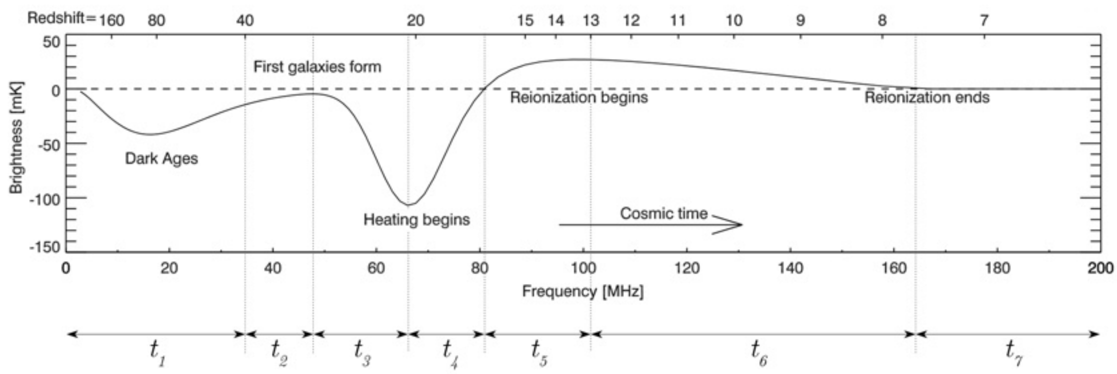

Figure 1.4: The expected evolution of sky-averaged 21-cm brightness temperature (taken from Pritchard & Loeb 2012, with modifications inspired by J. L. B. Line 2017) between the dark ages ($z \simeq 200$) to the end of reionisation ($z \simeq 6$). The solid curve indicates the signal, dashed line indicates $\Delta T = 0$, and the dotted lines demarcate important periods of the evolution of the 21-cm signal, labeled t:

- t_1 Gas continues cooling adiabatically, resulting in collisional coupling $T_s < T_{CMB}$, leading to an absorption signal during the Dark Ages

- t_2 Reduced efficiency of collisional coupling due to cosmological expansion, and radiative cooling sets $T_s = T_{CMB}$ with no detectable signal

- t_3 Birth of first stars and galaxies leading to emission of both Lyman-α photons and X-rays. X-rays heat the IGM, increasing gas temperature (T_k), while Lyman-α

couple to the gas. Spin temperature is coupled to cold gas such that $T_s \sim T_k < T_{CMB}$, resulting in an absorption signal

t_4 Lyman-α coupling saturates, and heating becomes significant. As T_k increases slowly so does T_s raising the 21-cm signal amplitude, till it eventually crosses over from absorption to emission

t_5 T_k continues increasing due to Lyman-α coupling, until 21-cm signal saturation occurs when $T_s \sim T_k >> T_{CMB}$

t_6 T_{CMB} no longer contributes to Equation 1.1. As reionisation progresses the signal is dominated by ionisation fraction, and reduces in amplitude

t_7 Reionisation is complete, most 21-cm signal comes from HI in galaxies

1.4. Foregrounds

The cosmological 21-cm signal the Epoch of Reionisation between $z \simeq 6-15$ can be observed between $\sim 200-90$ MHz. The primary obstacle hindering a statistical detection of the 21-cm signal are a range of astrophysical and terrestrial foregrounds which can up to ~ 5 orders of magnitude brighter than the cosmological signal (e.g. Oh & Mack, 2003; Santos et al., 2005; Jelić et al., 2008; Bowman et al., 2009; Pindor et al., 2011; Pober et al., 2013; Yatawatta et al., 2013). These foregrounds are dominated by Galactic diffuse synchrotron radiation, supernovae remnants, extragalactic radio-loud galaxies and Active Galactic Nuclei (AGNs). Time variable distortions induced by the ionosphere warp all celestial radiation. Terrestrial transmissions from radio, television, and satellite communication all fall within or adjacent to this observing band. Galactic synchrotron radiation occupies $\sim 70\%$ of the foreground flux budget at 150 MHz, while extragalactic sources contribute $\sim 27\%$ (Shaver et al., 1999). Figure 1.5 depicts the various components of foregrounds ordered by proximity — from astrophysical to terrestrial and instrumental.

1.5. Thesis Outline

The obstacles hindering the first EoR detection cannot be understated and require unprecedented precision at all levels —- from the understanding of our instruments and foregrounds to the astrophysical inferences drawn from observations. This thesis presents advances in measuring and understanding the impact of interferometric instrumental systematics on an Epoch of Reionisation detection.

In Chapter 2, we provide a foundational introduction to low-frequency radio interferometry, with a focus on the Murchison Widefield Array (MWA) telescope. In Chapter 3, we develop and implement an experiment to use communication satellites to perform in-situ all-sky dual-polarised measurements of MWA beampatterns, revealing significant sidelobe distortions at the $\sim 10\%$ level. In Chapter 4, we develop a framework to emulate measured beam deformations with cutting-edge beam models. This chapter also tests the impact of an imperfect instrumental representation, during calibration of astronomical data, can have on a future EoR detection. In Chapter 5, we explore how

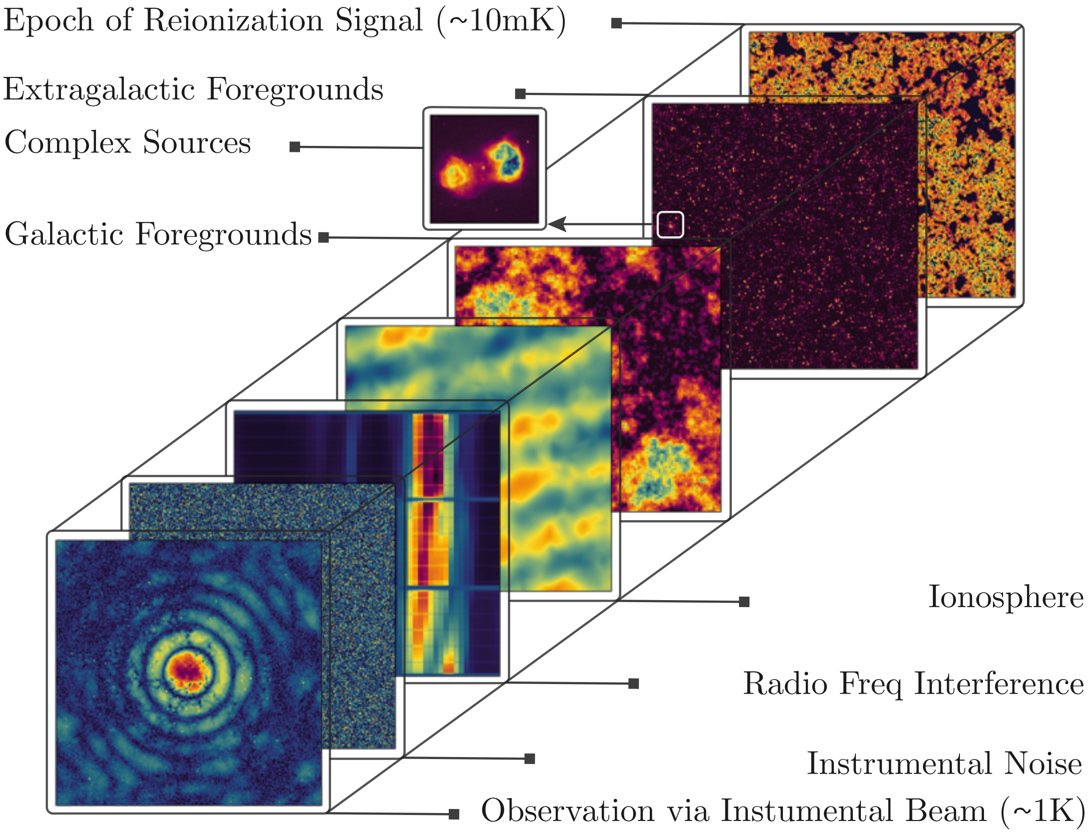

Figure 1.5: A breakdown of astrophysical and terrestrial foregrounds, ordered by proximity, which must be precisely peeled away or avoided to measure the EoR signal. An illustration inspired by Jelić et al. (2008), extended to include terrestrial and instrumental effects to depict the entire dynamic range that an EoR measurement must span.

deformed beams interact with the polarised radio sky, and the impact on studies of cosmic magnetism. We finally conclude and discuss this thesis in Chapter 6, with a focus of future directions of investigations towards a first detection of the cosmological signal from the Epoch of Reionisation.

Beneath desert skies,
Murchison listens for light,
Echoes from the dawn.

Aman, 2024, *Haiku*

CHAPTER 2

Measurement Theory & the Murchison Widefield Array

Traditional telescopes achieve angular resolutions of $\sim \lambda/D$, where λ is the observing wavelength, and D is the aperture diameter. Exploring the Universe at longer radio wavelengths necessitated the development of larger and larger single-dish telescopes. Despite the mechanical marvel of the world's largest physically steerable telescope[*] achieving an aperture of $D = 100\,\mathrm{m}$, pushing much beyond this is infeasible. The desire for higher resolutions at these longer wavelengths led to the development of radio interferometry, where observations from multiple smaller telescopes are coherently synthesised to achieve angular resolutions determined by the separation between the telescopes rather that the diameter of each telescope. This concept revolutionised the field of radio astronomy.

This chapter discusses the fundamentals of radio interferometry, establishes a mathematical framework in which Epoch of Reionisation measurements can be understood, and explores the elegance of the Murchison Widefield Array telescope.

2.1. Introduction to Interferometry

The fundamental measurement made by a radio interferometer is called a visibility, is the time-averaged cross-correlation between pairs of voltage signals observed by a pair of receiving elements. An interferometer composed of N receiving elements can be considered an ensemble of $N(N-1)/2$ two-element interferometers, each making a unique measurement. For a source in direction $\hat{\mathbf{s}}$, and a baseline vector $\mathbf{b}$ separating a pair of antennas $1, 2$, the plane wavefront arrives at one antenna before the other, with a geometric delay given by:

$$\tau_g = \vec{\mathbf{b}} \cdot \hat{\mathbf{s}}/c, \tag{2.1}$$

were c is the speed of light. Quasi-monochromatic signals measured by antennas $1, 2$, centred at frequency ν are $V_1(t)$ and $V_2(t)$ respectively. These voltages are multiplied and time-averaged by the correlator resulting in a visibility:

[*] A title currently held by the Green Bank Telescope

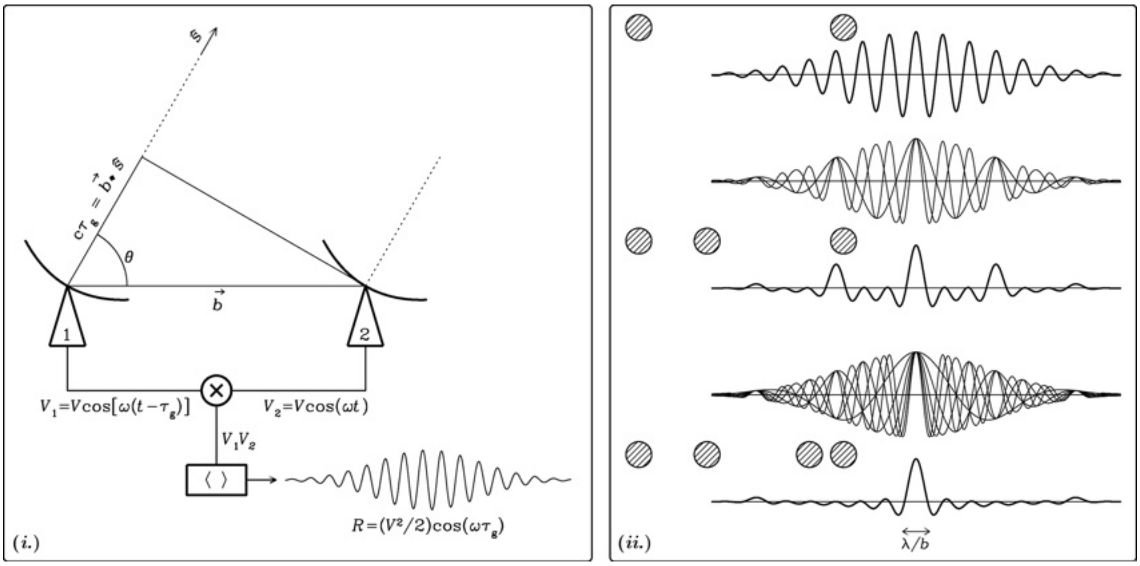

Figure 2.1: Illustrations of interferometry from Condon & Ransom (2016). The left panel (*i.*) represents a simple two-element interferometer. Plane waves incident on the pair, experience a geometric phase delay from an off-zenith source in direction $\hat{\mathbf{s}}$. The time-averaged cross correlation of voltages measured by each pair of antennas represent a visibility, and exhibit a fringe pattern as the source transits the sky. The right panel illustrates how the combination of multiple pairs of two-element interferometers rapidly approaches a Gaussian response to the sky, known as the synthesised beam whose angular resolution approaches $\theta \approx \lambda/\mathrm{b}$, the ratio of wavelength and maximum seperation between receiving elements.

$$R = \langle V_1(t) V_2(t) \rangle = \left(\frac{V^2}{2}\right) \cos\left(\omega \tau_g\right), \tag{2.2}$$

whose amplitude is proportional to the flux density of the source at $\hat{s}$, and phase $(\omega\tau_g)$ depends on geometric delay τ_g and frequency $\nu = \omega/2\pi$. As the source transits the sky the geometric delay changes, resulting in an alternation between constructive and destructive combinations of signals from the two antennas. This is observed as a sinusoidal fluctuation in the measured visibility R known as a fringe, enveloped in a broad Gaussian envelope resulting from the primary beam response of the receiving elements (see panel (*i.*) of Figure 2.1). For interferometers constructed of identical receiving elements, the primary beam is the product of the power pattern of individual antennas (see Appendix B for a review of primary beam models). In the absence of antenna beams, the point source response of the interferometer would be a sinusoidal fringe spanning the sky — sampling a single Fourier mode of the sky brightness distribution with angular period $\lambda/\mathrm{b}\sin\theta$.

Graduating from the pedagogic two element interferometer, we can gradually begin including more antennas. Every unique pair of antennas samples a different Fourier mode of the sky brightness distribution. The $N(N-1)/2$ visibilites measured by a N element interferometer can be coherently synthesised to rapidly approach a Gaussian response on the sky (see panel (*ii.*) of Figure 2.1). This is known as the instantaneous synthesised beam, and has an angular resolution approaching $\theta \approx \lambda/b$, the ratio of wavelength λ and maximum baseline b.

This framework can be further generalised by considering an extended sky brightness distribution $I(\hat{\mathbf{s}})$ instead of a single point source. Additionally a fully complex correlator must be utilised to describe an arbitrary source brightness distribution, using a sine and cosine basis. The response of a two element interferometer to an extended source can be formulated using Euler's formula to perform the complex correlation. We can generalise Equation 2.2 to complex visibilities as:

$$\mathcal{V}_\nu = \int \mathcal{A}_\nu(\hat{\mathbf{s}}) I_\nu(\hat{\mathbf{s}}, \nu) \exp(-2\pi i \vec{\mathrm{b}} \cdot \hat{\mathbf{s}}/\lambda)\, d\Omega, \tag{2.3}$$

were $\mathcal{A}_\nu(\hat{\mathbf{s}})$ is the normalised beam response of the two antennas, $I_\nu(\hat{\mathbf{s}})$ is the intensity of the source across the sky, $\vec{\mathrm{b}}$ is the baseline vector between antennas, ν is frequency, and $d\Omega$ represents an integration across the sky.

In practice, the application of Equation 2.3 requires the introduction of a coordinate system. A common notation is to use the Fourier dual of the spatial vector $\hat{\mathbf{s}}$ to describe wavelength dependent baseline vectors $\mathbf{u} = \mathbf{b}/\lambda = (u, v, w)$. Note that, (u, v, w) are measured in terms of wavelengths, pointing East, North and towards the phase centre (a direction of interest), respectively. Positions on the sky are conveniently described by the directional cosines (l, m, n), measured with respect to the (u, v, w) axes which obey $l^2 + m^2 + n^2 = 1$. In this coordinate system, Equation 2.3 become:

$$\mathcal{V}_\nu(u, v, w) = \int\int \frac{\mathcal{A}_\nu(l, m) I_\nu(l, m)}{(1 - l^2 - m^2)^{1/2}} \exp\left[-2\pi i(ul + vm + wn)\right] dl\, dm, \tag{2.4}$$

with the integrand evaluated where $l^2 + m^2 < 1$. This relation is reminiscent of a two-dimensional Fourier transform, and can reduce to it under two sets of special conditions. The first is by building East-West interferometers which have baselines confined to a plane, under Earth Rotation. The baseline coordinates can then be defined with w pointing to a celestial pole. Setting $w = 0$ in Equation 2.4 results in a Fourier relation which can be readily inverted to form synthesised images. The second case occurs when $|l|$ and $|m|$ are small enough that:

$$\left(\sqrt{1 - l^2 - m^2} - 1\right) w \approx -\frac{1}{2}(l^2 + m^2) w = 0. \tag{2.5}$$

Equation 2.4 becomes:

$$\mathcal{V}_\nu(u, v) = \int\int \mathcal{A}_\nu(l, m) I_\nu(l, m) \exp\left[-2\pi i(ul + vm)\right] dl\, dm. \tag{2.6}$$

inverting this Fourier relation:

$$\mathcal{A}_\nu(l, m) I_\nu(l, m) = \int\int \mathcal{V}_\nu(u, v) \exp\left[2\pi i(ul + vm)\right] du\, dv, \tag{2.7}$$

in this narrow-field imaging regime, the dependence of visibilities on w is negligible. We now posses the mathematical framework required to describe an arbitrary interferometer, and have explored how measured visibilities can be converted to a synthesised image. In the following section we explore how the unique measurement spaces of interferometers both facilitate and hinder the search for the EoR signal.

2.2. Interferometric Measurement Spaces

Measurements by interferometers are in a intermediate $\{u, v, f\}$-space comprised of sets of Fourier modes at the set of frequencies in the telescope's band. This space is neither convenient for imaging $\{x, y, f\}$, nor for power spectrum estimations $\{u, v, \eta\}$; where I x, y are spatial directions, u, v are Fourier modes defined by baseline vectors, f is frequency, and η is the Fourier dual of frequency (Morales & Hewitt, 2004). Transformations between various spaces are depicted in Figure 2.2, and described below.

(i.) We observe galaxies scattered across a cosmological volumes, with the x, y Cartesian axes aligned with the plane of the sky for an observer on Earth. The line-of-sight into the sky is aligned with the z axis, along which cosmological evolution can be observed (Figures 1.1, 1.4).

(ii.) As discussed in Section 1.3, the evolution of the Universe can be observed by measuring the intensity of the redshifted 21-cm line from neutral Hydrogen across cosmic time. In practice, this is achieved by observing the sky as a function of frequency f. Synchrotron emission follows a power law spectra, varying slowly with frequency. Thus in this intermediate spatial-frequency $\{x, y, f\}$ space, extragalactic sources span the frequency axis.

(iii.) Interferometers do not natively measure sky brightness intensity, rather each constituent baseline samples a Fourier mode on the sky for every frequency (see Section 2.1 and Equation 2.6). Thus the native measurement space of an interferometer is $\{u, v, f\}$, depicted in panel (iii.) of Figure 2.2.

(iv.) Interpreting native measurements in the $\{u, v, f\}$ space is challenging. Performing a spatial Fourier transform results in dirty images* as a function of frequency $\{x^*, y^*, f\}$, where x^*, y^* are indicative of dirty imaging.

(v.) An alternate method of understanding interferometric measurements is to embrace their Fourier nature, and perform a one-dimensional Fourier transform along the frequency axis resulting in $\{u, v, \eta\}$-space. An additional coordinate transform results in a three-dimensional Fourier representation of the measurements in a $\{k_x, k_y, k_z\}$ space. Here the wavenumbers k_x, k_y lie along the plane of the sky, with modes along the line-of-sight being aligned with k_z. Interestingly, the majority of foreground flux described in Section 1.4 is slowly varying with frequency, resulting in this power being contained within the first few k_z Fourier modes (see white dotted lines perpendicular to k_z in Figure 2.2). The utility of the Fourier space is already apparent!

*Dirty images arise for the inherent incomplete sampling of the Fourier plane by interferometers. The inverse Fourier transform of visibilities results in an image containing *only* spatial scales sampled by the interferometer, thus missing some information and imperfectly recovering the true sky brightness distribution.

(*vi.*) Since there is nothing particularly unique about the rotation of the axes in the plane of the sky, performing a cylindrical average on the $\{k_x, k_y, k_z\}$ space, along k_z can separate modes of contamination and signal in deterministic ways. We define two new wavenumber axes; $k_{||} = k_z$ (Fourier modes along the line-of-sight), and $k_{\perp} = \sqrt{k_x^2 + k_y^2}$ in the plane of the sky. Slowly frequency varying foreground power is then contained within the lower $k_{||}$ modes (below horizontal white line in Figure 2.2). This two-dimensional power spectrum space is an elegant diagnostic tool in which foreground, cosmological, and instrumental systematics become apparent. Of particular import is the wedge-like structure above the low-$k_{||}$ foreground modes. This arises from the chromatic nature of interferometers, which inherently sample different u, v modes as a function of frequency, leading to mode-mixing of foreground power into higher $k_{||}$ modes. This characteristic of interferometric measurements has long been studied (see Datta et al., 2010; Morales et al., 2012; Vedantham et al., 2012; Parsons et al., 2012; Trott et al., 2012; Hazelton et al., 2013; Thyagarajan et al., 2013; Pober et al., 2013; Liu et al., 2014a,b; Thyagarajan et al., 2015).

(*vii.*) Finally, spherically averaging Fourier $\{k_x, k_y, k_z\}$ modes gives us the highest signal-to-noise. This one-dimensional representation of the power spectrum provides the optimal space in which to attempt making a statistical detection of the cosmological signal from redshifted Hydrogen.

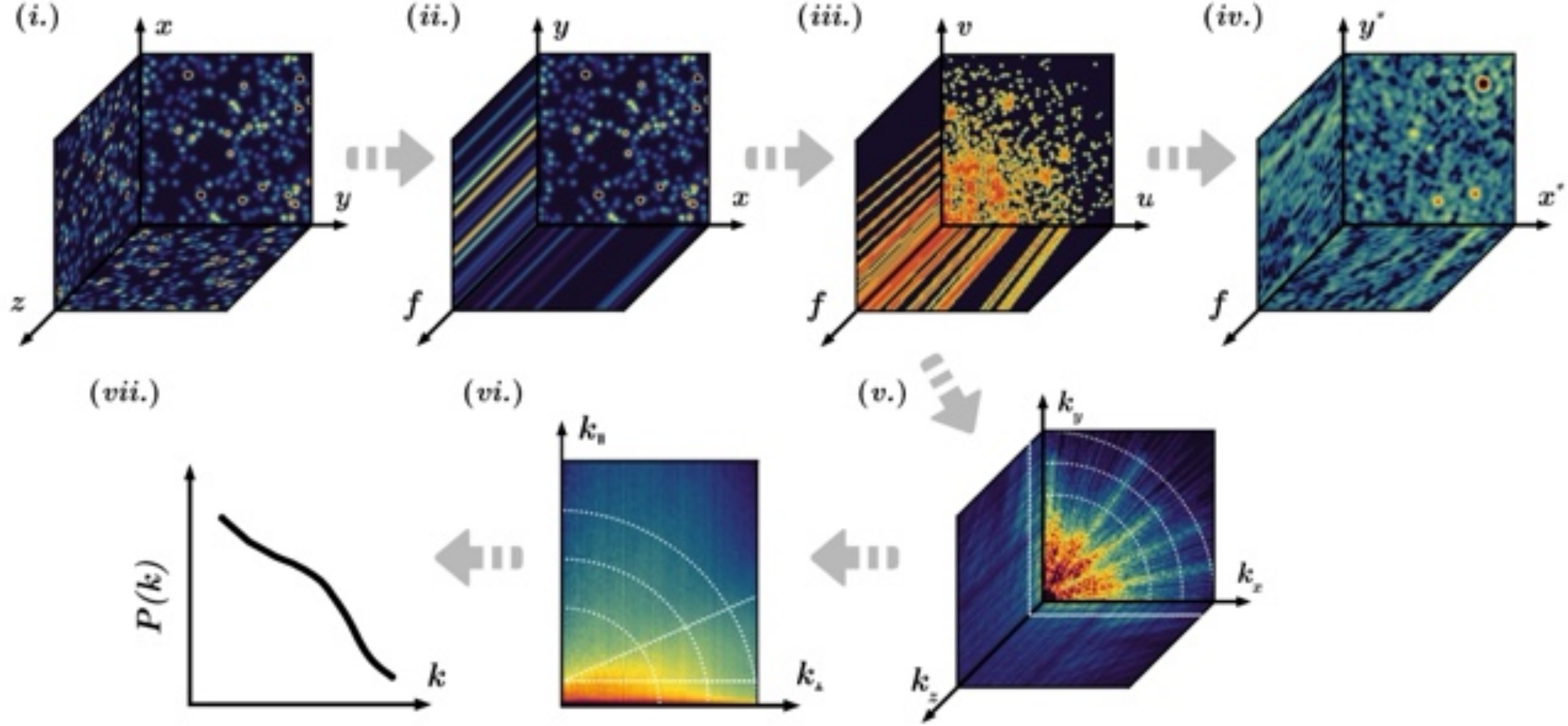

Figure 2.2: An illustration of the various mathematical spaces involved in interferometric measurements, from representations of Cartesian space in panel $(i.)$, intermediate spatial-frequency space in $(ii.)$, interferometric measurements in $(iii.)$, interferometric imaging in $iv.$, and power spectrum estimation panels $(v.), (vi.), (vii.)$. Here (x, y, z) represent Cartesian coordinates with the first two aligned in the plane of the sky, with the third along the line of sight. Frequency is f, its Fourier dual is η, (u, v) are Fourier spatial coordinates and (k_x, k_y, k_z) are wavenumber. The relation between various spaces are discussed in Section 2.2.

2.3. The Murchison Widefield Array

The Murchison Widefield Array* (MWA) is the low-frequency radio interferometer located at *Inyarrimanha Ilgari Bundara*†, the CSIRO Murchison Radio-astronomy Observatory (MRO), in the remote Western Australian outback. Designed with a primary goal of detecting the 21-cm EoR power spectrum, its science capabilities extend far beyond; including Galactic and extragalactic surveys, time variable astrophysics, solar and ionospheric science and searches for exoplanets and fast radio bursts (see Bowman et al., 2013; Beardsley et al., 2019a, for a description of key science goals).

Each antenna of the array is composed of a regular grid of 4×4 dual-polarised bow-tie dipoles, on a 5×5 m reflective metal mesh which acts as a groundscreen (see Figure 2.3). The orthogonal dipoles of each "tile" are aligned with the East-West and North-South cardinal directions, and are labeled X and Y respectively. The dipoles are sensitive to the entire visible sky in the $80 - 300$ MHz band. The signals from each dipole are initially amplified by a low noise amplifier (LNA) in the central column of the dipole before being combined by an analogue beamformer (white box to the right of the tile in Figure 2.3). The analogue beamformer synthesises the signals from the 16 dipoles to construct a primary beam response on the sky with a full-width-half-max (FWHM) of roughly 25°, and integrated collecting area of about 15m^2 at 150 MHz. By inserting analogue delays between the dipoles, the beamformer is capable of digitally pointing the primary beam response away from its neutral zenith sensitivity.

The initial construction of the Phase I stage of the MWA was composed of 128 tiles arranged in a pseudo-random configuration across ~ 3 km of the desert (Beardsley et al., 2012; Tingay et al., 2013). In 2017, the telescope was upgraded with a Phase II expansion (Wayth et al., 2018) which increased the total number of tiles to 256, 128 of which could be correlated at any one time. The Phase II extension consisted of two possible configurations; an addition of two redundant hexagonal arrays to increase short baselines for EoR sensitivity, or a set of long baselines up to 5 km to improve angular resolution. The MWA is currently undergoing its Phase III upgrade (powered by the new MWAX correlator, see Morrison et al., 2023) which will enable it to correlate all 256 tiles at once, massively increasing sensitivity. The left panel of Figure 2.4 depicts the layout of Phase I tiles in green and Phase II tiles in orange. The right panel shows the density of baselines of the 128 Phase I tiles between $167 - 200$ MHz.

Radio frequency signals from sets of 8 tiles are transmitted to digital receivers, which can process 30.72 MHz of bandwidth in real time. A polyphase filterbank first splits this bandwidth into 24×1.28 MHz coarse bands, and then into 768 40 kHz fine channels. The correlator (Ord et al., 2015; Morrison et al., 2023) cross-multiplies data from every unique set of tiles, at a 0.5 s or 2 s resolution, to create visibilities (see Section 2.1, and Equation 2.4) - the fundamental measurements of interferometers.

Finally, the Murchison Widefield Array boasts a truly *wide* field-of-view. It is tough to understate how significant an impact this makes to the quality and scope of science it enables. The FWHM of the primary beam spans a staggering $25° \times 25°$ field of view, enabling rapid sky surveys along with efficient measurements of large cosmo-

*https://www.mwatelescope.org

†The Wajarri Yamaji people, the traditional owners of the land, have named the site *Inyarrimanha Ilgari Bundara*, meaning *sharing sky and stars.*

Figure 2.3: Photos from the MWA site. In the top panel is one of 128 MWA tiles in the Western Australian desert, comprised of sixteen dual-polarisation bow-tie dipoles, signals from which are combined by an analogue beamformer to the right of the tile, before being passed to a digital reciever for processing. A goanna (not to scale), passes though the site during my visit in 2019. This beautiful specimen was roughly 1.5m in length. Goannas are notoriously stupid, and when startled are know to climb up humans with their sharp claws, mistaking them for trees. In the bottom left image, I am installing equipment into an MWA receiver for the satellite beam experiment described in Chapter 3 (Photo Credit: Jack Line). The final image is a reference antenna Nichole Barry, Jack Line and I built at the MRO, with me on top for scale (Credit: Nichole Barry).

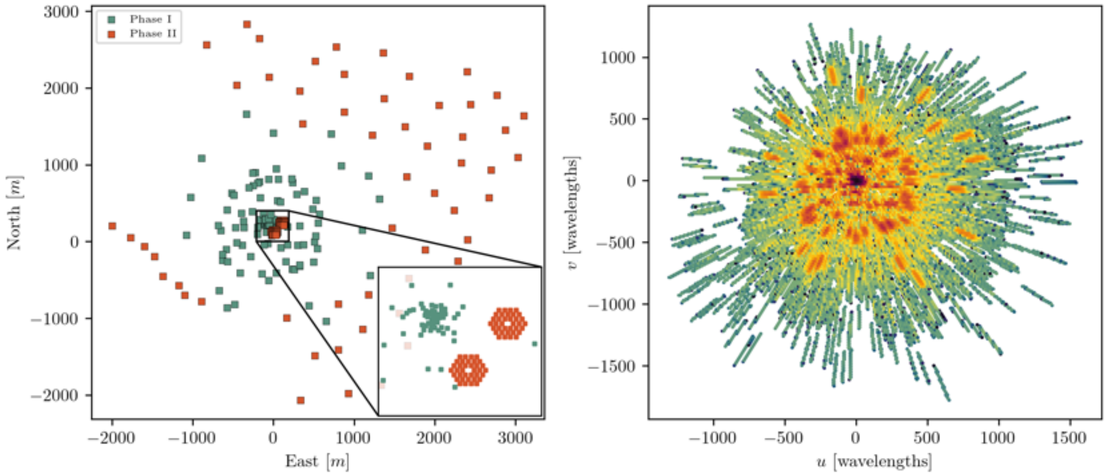

Figure 2.4: The left panel shows the location of the 256 MWA at the MRO, with the original Phase I tiles in green and the newer Phase II tiles in orange. The two Phase II redundant hexagonal arrays are showed in the inset. The right panel display the density of (u, v) baseline coverage of the 128 Phase I tiles, between $167 - 200$ MHz.

logical volumes. What is less obvious is that the primary beam of each tile is actually sensitive to the *entire* sky - horizon to horizon. Figure 2.5 illustrates the extent of the primary beam pattern of the MWA at 182 MHz, with beam sensitivity contours at $90, 50, 30, 10, 1, 0.1\%$ plotted over the Haslam map of the galaxy at 408 MHz (Haslam et al., 1981; Remazeilles et al., 2015). The figure is centred around the EoR 0 observing field ($\alpha = 0, \delta = -27°$), chosen to be one of the quietest parts of the sky, yet the beam sidelobes intersect with the rising Galactic plane. Even attenuated by a factor of a 1000, the apparent magnitude of the Galactic plane on the horizon can rival emission from the zenith of this quiet field.

Any uncertainties in the primary beam model can lead to the mis-estimation and mis-calibration of far-field sources. Much of this thesis focuses of developing and implementing experiments to measure the all-sky beam patterns of the MWA, and understand their non-trivial coupling to foreground power, with an emphasis of the implications of such effects on a future EoR detection.

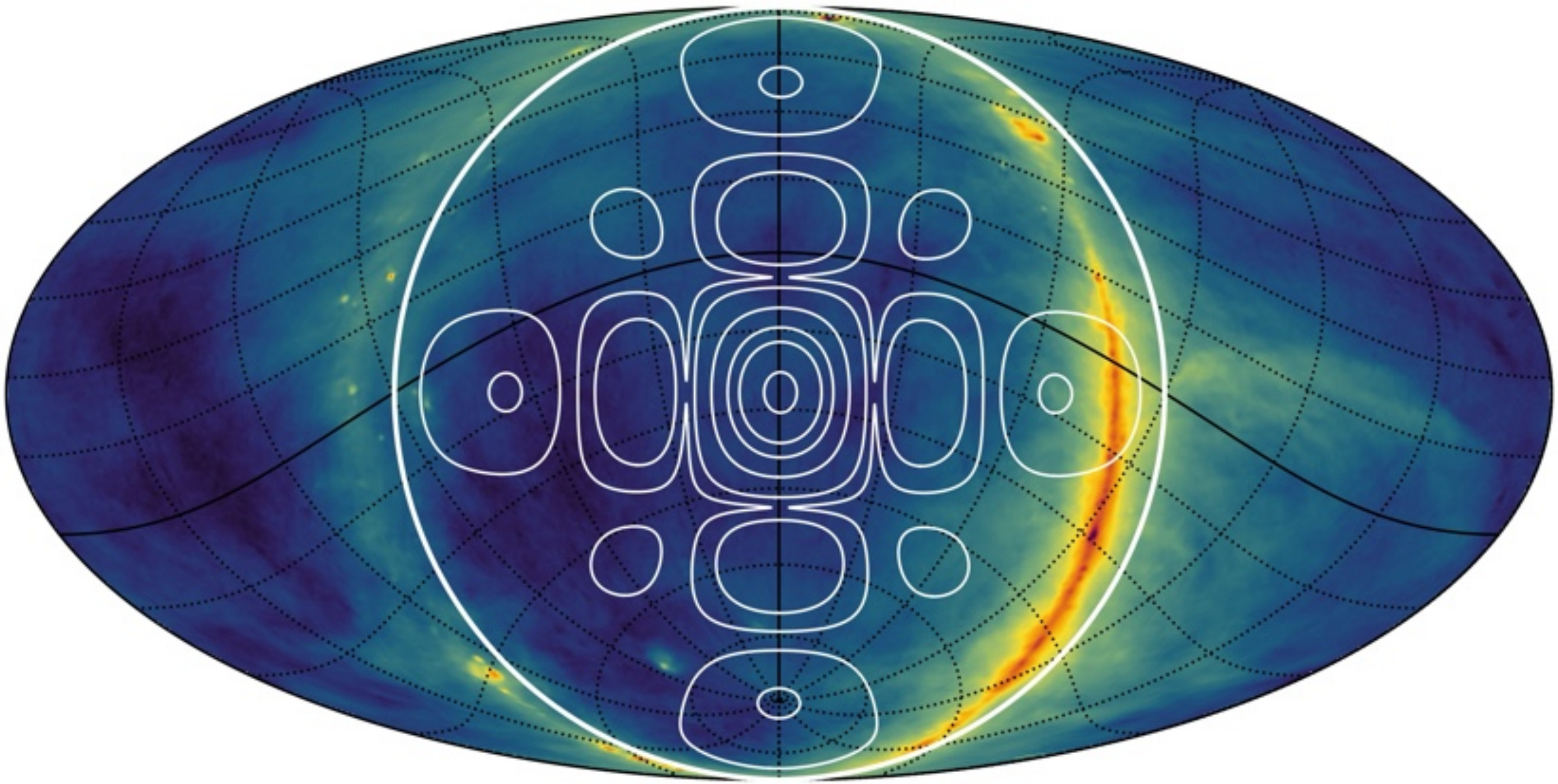

Figure 2.5: An illustration of the truly *wide* field-of-view of the Murchison Widefield Array. Plotted on top of the galactic Haslam map are all-sky sensitivity contours of the MWA primary beam at 182 MHz, with 90, 50, 30, 10, 1, 0.1% levels. This figure is centred around one of the quietest parts of the sky - the EoR 0 observing field ($\alpha = 0, \delta = -27°$), yet the beam is sensitive to the rising Galactic plane on the horizon.

CHAPTER 3

Dual Polarization Measurements of MWA Beampatterns at 137 MHz

This chapter is based on

A. Chokshi, J. L. B. Line, N. Barry, D. Ung, D. Kenney, A. McPhail, A. Williams, R. L. Webster
Monthly Notices of the Royal Astronomical Society, 502, 2, 2021, 1990

reformatted with the following changes only:

- **The text is styled and restructured to match the rest of this thesis.**
- **Where necessary, bibliographic records are updated.**

3.1. Abstract

The wide adoption of low-frequency radio interferometers as a tool for deeper and higher resolution astronomical observations has revolutionized radio astronomy. Despite their construction from static, relatively simple dipoles, the sheer number of distinct elements introduces new, complicated instrumental effects. Their necessary remote locations exacerbate failure rates, while electronic interactions between the many adjacent receiving elements can lead to non-trivial instrumental effects. The Murchison Widefield Array (MWA) employs phased array antenna elements (tiles), which improve collecting area at the expense of complex beam shapes. Advanced electromagnetic simulations have produced the Fully Embedded Element (FEE) simulated beam model which has been highly successful in describing the ideal beam response of MWA antennas. This work focuses on the relatively unexplored aspect of various in-situ, environmental perturbations to beam models and represents the first large-scale, in-situ, all-sky measurement of MWA beam shapes at multiple polarizations and pointings. Our satellite-based beam measurement approach enables all-sky beam response measurements with a dynamic range of ~ 50 dB, at 137 MHz.

3.2. Introduction

The pursuit for deeper, higher resolution astronomical observations for new scientific programs has led to the adoption of low-frequency radio interferometer arrays. Large numbers of relatively simple dipoles, coherently synthesized together, have angular resolutions capable of exceeding the largest traditional dish telescopes. Notably, some of the largest interferometers are now the size of the Earth and beyond. These instruments are ideal for investigations from the local to the early universe. Unfortunately, the spectral windows relevant to such observations are often contaminated by radio frequency interference (RFI) from FM radio, television, and other man-made sources, necessitating that these sensitive instruments be located at some of the most remote and least populous regions of the world.

Electronic interactions between the large number of identical and adjacent elements in an interferometer can lead to complex instrumental responses, exacerbated by disproportionate dipole failure rates due to harsh environmental conditions. This underpins the importance of accurate instrumental beam models which will enable precise calibration of data and increase the sensitivity of various science investigations.

The Murchison Widefield Array (MWA*; Tingay et al., 2013; Wayth et al., 2018) is a precursor to the Square Kilometer Array (SKA†), located at the Murchison Radio-astronomy Observatory, in the remote western Australian outback. Designed to observe the low-frequency radio sky between 80 and 300 MHz, one of the MWA's key science goals is detection of redshifted 21 cm emission from the Epoch of Reionization (EoR) (Bowman et al., 2013; Beardsley et al., 2019b). In this work we will explore the in-situ measurement of MWA beam shapes, broadly in the context of EoR science.

The high dynamic range of EoR experiments, coupled with the intrinsic chromatic nature of radio interferometers can introduce spectral structure variations, leading to calibration errors which must be constrained to high levels of precision (e.g. Barry et al., 2016; Trott & Wayth, 2016; Patil et al., 2017). The Fully Embedded Element (FEE) beam model (Sutinjo et al., 2015; Sokolowski et al., 2017) is a cutting-edge electromagnetic simulation of the tile response using the FEKO‡ simulation package which can be used in EoR pipelines such as the RTS and FHD (Mitchell et al., 2008; Sullivan et al., 2012; Barry et al., 2019a). While accurate simulations of the instrumental beam has been crucial in improving calibration, simulations reflect ideal conditions, which often do not perfectly represent the in-situ reality. This is especially true for the MWA, located in a remote harsh desert, where multiple environmental factors may perturb instrumental beams from their ideal behaviour.

A relatively unexplored aspect of the calibration of radio interferometric data is the instrumental beam. Errors in beam models can introduce flux calibration and polarization errors which may significantly impede the detection of the EoR signal. Simulations by Joseph et al. (2019) show that beam deformations due to broken dipoles can introduce biases in the 2D power spectrum (PS) up to two orders of magnitude above the expected EoR signal. Laboratory measurements and simulations by Neben et al. (2016a) reveal that inter-tile beam variation due to beamformer errors make foreground subtraction

---

*http://www.mwatelescope.org

†https://www.skatelescope.org

‡http://www.feko.info

infeasible. This is not an insurmountable issue for scientific studies which plan on utilizing a foreground avoidance approach, as it is shown that beamformer errors do not contribute significant spectral structure into the theoretically foreground-free regions of the power spectrum.

Spectral features of $\sim 10^{-5}$ in the antenna or receiver system can hinder the detection of the EoR signal (Barry et al., 2016). It is possible that spectral structure of this scale could be introduced via errors in beam calibrations. Local environmental effects can be large contributors to beam distortions and it is unclear in precisely what ways these distortions contribute spectral structure to the PS, emphasising the requirement for exceptionally well characterised individual beam models for more sophisticated analysis of EoR data.

This paper is presented in the context of EoR science, but has broad implications and the scope to significantly inform a wide variety of science cases which utilise data from wide-field radio interferometers. For example, radio polarimetry studies using the MWA have found significant flux leakage from Stokes I into other Stokes parameters (Bernardi et al., 2013; Lenc et al., 2017, 2018). For a Zenith pointings (-27° declination) leakage was $\sim$ 1% and $\sim$ 4% at the edge of the primary beam, increasing to a range of 12-40% at off zenith pointings. The GaLactic and Extragalaxtic All-sky MWA (GLEAM) survey (Wayth et al., 2015; Hurley-Walker et al., 2014, 2017) found beam errors cause frequency and declination dependant errors in Stokes I. Surveys such as GLEAM form the basis for calibration of EoR observations, making a correct flux scale essential. The increasing unreliability of the beam model, away from zenith, causes surveys such as GLEAM to only use the central half-power portion of the primary beam. Accurate beam models would enable the use of a larger portion of the beam with confidence, presenting the opportunity for a significant increase in sensitivity and thus faster experiments and better utilisation of precious telescope time.

A traditional method of beam measurement, known as radio holography, utilises drift scans of celestial sources of known flux densities to probe cross-sectional slices of the primary beam (e.g. Nunhokee et al., 2020; Berger et al., 2016; Pober et al., 2012; Thyagarajan et al., 2011; Bowman et al., 2007). Pulsar holography has been proposed to improve polarised beam measurements (Newburgh et al., 2014). A significant impediment to such methods is the faint nature of celestial sources which often have insufficient flux to probe the depths of the beam sidelobes and nulls, especially since wide-field instruments such as the MWA are sensitive to the whole sky.

An alternate method being explored is the use of radio transmitters mounted on commercially available drones (e.g. Jacobs et al., 2017; Chang et al., 2015). This technique has been used as an in-situ validation of two SKA-Low prototype arrays (Paonessa et al., 2020) and LOFAR* antennas (e.g. Ninni et al., 2020; Bolli et al., 2018; Virone et al., 2014). A distinct advantage of this approach is the control and repeatability of drone flight paths, at multiple frequencies, enabling broadband characterization of beam shapes. While promising, this method comes with a set of drawbacks. Drones have limited altitude ranges and thus operate in the near-field of the instrument as opposed to astronomical observations which occur in the far-field. This is particularly relevant to wide-field instruments, where the projection of the drone mounted transmitter beam couples to the Antenna Under Test (AUT) beam, and is exacerbated as the drone moves further from

*http://www.lofar.org

zenith. Finally, the use of bright radio receivers at radio-quiet zones make such methods challenging for large interferometric arrays such as the MWA, LOFAR, HERA* and the upcoming SKA-Low.

The final method used to measure beam shapes and the focus of this paper, utilises satellites as bright radio sources with known trajectories, to probe cross-sectional slices of the AUT. Advantages of this method include: bright satellites enabling high dynamic range observations of the beam and sidelobes; sources emitting in the far field; the precision of orbital tracks creating new slices of the AUT beam with each orbit. This method was neatly demonstrated by Neben et al. (2015) using a test MWA tile and by Neben et al. (2016b) using a prototype HERA dish at the NRAO Green Bank Observatory†. The work of Line et al. (2018) represents the first in-situ demonstration of this method at the MWA site.

This paper represents the first large-scale, in-situ, all-sky measurement of MWA beam shapes at multiple polarizations and pointings, with the aim to quantify inter-tile variations and measure environmental beam distortions at 137 MHz using communication satellites. Our methodology demonstrates a passive parallel monitoring system, which measures the beam shapes of MWA tiles in parallel to regular observations with no disruption to the operation of the telescope. As this setup was built using cheap off-the-shelf components, and the analysis is carried out using our open-source `python`‡ package called `EMBERS`§ (Experimental Measurement of BEam Responses with Satellites) (Chokshi et al., 2020), we present it as a prime candidate for a passive beam monitoring system for large interferometric arrays such as the MWA, HERA, LOFAR and SKA-Low. As Radio Frequency Interference (RFI) encroaches on the last remaining radio-quiet observatories, archival data becomes ever more valuable. The addition of measured beam shapes could be critical to the analysis of this data in the future, when more sophisticated analysis techniques are developed.

A description of the MWA Telescope, experimental setup and data acquisition system are explained in Section 3.3, following which Section 3.4 outlines our data analysis method. In Section 3.5 we present challenges encountered in our analysis, experimental biases and the results. Finally, in Section 3.6, we discuss implications of this work and possible future directions.

3.3. Experimental Method

The approach taken in this experiment is an extension of investigations presented in Line et al. (2018) and Neben et al. (2015). The premise of this work is based around using radio satellites, with well known orbital trajectories, to probe the beam response of MWA tiles. The power received by the Antenna Under Test (AUT) is the product of the beam response B_{AUT} and the flux transmitted by the satellite F. A reference antenna with a simple, well known beam response B_{ref} is used to record the modulation of the transmitted flux, and can subsequently be used to compute the beam shape of the AUT. The power received by the AUT and reference antenna are $P_{\mathrm{AUT}} = B_{\mathrm{AUT}}F$ and

*https://reionization.org
†https://greenbankobservatory.org
‡https://www.python.org
§https://embers.readthedocs.io

Table 3.1: Reference and MWA tiles used in the Experiment. Each tile is dual-polarised with both XX and YY dipoles. For example, the rf0 tile has rf0XX and rf0YY arrays.

rf0	rf1	S06	S07	S08	S09	S10	S12
S29	S30	S31	S32	S33	S34	S35	S36

$P_{\mathrm{ref}} = B_{\mathrm{ref}}F$ respectively. These expression can be reduced to give us the response of the AUT, described by:

$$B_{\mathrm{AUT}} = \frac{P_{\mathrm{AUT}}}{P_{\mathrm{ref}}} B_{\mathrm{ref}}. \tag{3.1}$$

With each satellite pass, we measure a cross sectional slice of the AUT beam response. With sufficient observation time, an all-sky beam response is built up.

3.3.1. The Murchison Widefield Array

The MWA is an aperture array telescope, with 128 receiving elements or tiles, each constructed from a grid of 4×4 dual polarization bow-tie dipoles, mounted on a 5×5 m reflective metal mesh (Tingay et al., 2013). The two orthogonal linear polarizations of the MWA tiles are labled XX and YY, with dipoles aligned along the East-West and North-South directions respectively. MWA tiles have a wide field of view, with a full-width half-maximum $\sim 25°$ at 150 MHz, which can be steered using an analogue delay-line beamformer. The beamformers have a set of quantised delays available, which results in a set of 197 discrete pointings to which the beamformer can point the phase-center of the MWA beam. The phased array design of MWA tiles improves the collecting area of tiles, at the expense of additional complexity introduced to the beam shapes.

3.3.2. Data acquisition

The experimental setup used in this work is based on Line et al. (2018) and expanded to accommodate our new science goals which differ from previous methods in a few key ways.

We measure the all-sky beam response of 14 MWA tiles, over a 6 month period, at both instrumental polarizations (XX, YY) and at multiple pointings using ORBCOMM[*] communication, METEOR[†] and NOAA[‡] weather satellites. This work is the first demonstration of parallel, in-situ beam measurements without disruption to the telescope's observational schedule. The 14 MWA tiles are a part of the inner core of the compact configuration of the MWA array, located within the "Southern Hex" as shown in Figure 3.1. The names of the tiles can be found in Table 3.1. In addition to the Zenith pointing of the telescope, measurements of the beam response are carried out at two off-zenith pointings (see Table 3.2).

Radio frequency (RF) signals are simultaneously recorded from 14 MWA tiles and two reference antennas, in both XX and YY polarizations. The reference antennas are con-

[*] https://www.orbcomm.com/en/networks/satellite
[†] http://www.russianspaceweb.com/meteor-m.html
[‡] https://www.noaa.gov/satellites

Table 3.2: MWA beamformer pointings used in this work

MWA Pointing	Altitude	Azimuth	Integration [h]
0	90°	0°	~ 900
2	$83^\circ 11' 28.32''$	90°	~ 350
4	$83^\circ 11' 28.32''$	270°	~ 350

structed using a single dual polarization MWA dipole, centered on a $5 \times 5\,\mathrm{m}$ conductive ground mesh. Custom-built RFI shielded circuits are used to power the Low Noise Amplifiers (LNAs) within the dipole, and retrieve data via coaxial cables. These field boxes contain secondary LNAs, to further amplify RF signals, and Bias-Ts which facilitate data and power transfer through coaxial cables. These field boxes are placed near the reference antennas and are connected with long coaxial cables, to RF Explorers[*] located within a RFI shielded hut approximately 50 m away. RF signals from the tiles are acquired inside the MWA receivers (see Tingay et al.,, 2013), using beam splitters, after amplification and filtering by the Analogue Signal Conditioning unit. These are passed to RF Explorers installed within the receivers.

The RF Explorers are set to have a spectral resolution of 12.5 kHz, sampling 112 frequency channels between 137.150 MHz and 138.550 MHz. This frequency window was chosen to observe Meteor and NOAA weather satellites and the ORBCOMM constellation of communication satellites, which provide excellent sky coverage. The signal is acquired at a rate between 6 - 9 samples per second, limited by the hardware in the RF Explorers. A set of five Raspberry Pi[†] single-board computers are used to control and retrieve data from the 32 RF explorers connected to 14 MWA tiles and 2 reference antennas. The positions of the antennas can be seen in Figure 3.1. USB hubs are used to power and facilitate the control of multiple RF Explorers by a single Raspberri Pi. An outline of our experimental setup can be found in Figure 3.2.

The Raspberri Pi's are connected to the MWA network via ethernet cables, enabling remote control over the experiment. Network access allows the synchronisation of the Raspberri Pi's by syncing them to the same NTP server. The Raspberri Pi's control the RF Explorers using a custom `python` script and the `pySerial`[‡] module. Every 24 hours, a scheduled `cron job`[§] transfers the recorded RF data to an external server and, using the `at`[¶] command, schedules a day of 30 minute observations across all the RF Explorers.

The beam splitters allowed the experiment to run concurrently with normal MWA operations, meaning the pointing of the telescope was dictated by the regular observational schedule. A large amount of data was recorded using this setup, invariably including a significant portion irrelevant to this project. Though the experiment was plagued by technical failures of the RF Explorers, USB hubs and a rare lightning strike, between 12$^{\text{th}}$ September 2019 and 16$^{\text{th}}$ March 2020, over 4000 hours of raw data were collected.

[*] http://rfexplorer.com
[†] https://www.raspberrypi.org
[‡] https://pythonhosted.org/pyserial
[§] http://man7.org/linux/man-pages/man8/cron.8.html
[¶] http://man7.org/linux/man-pages/man1/at.1p.html

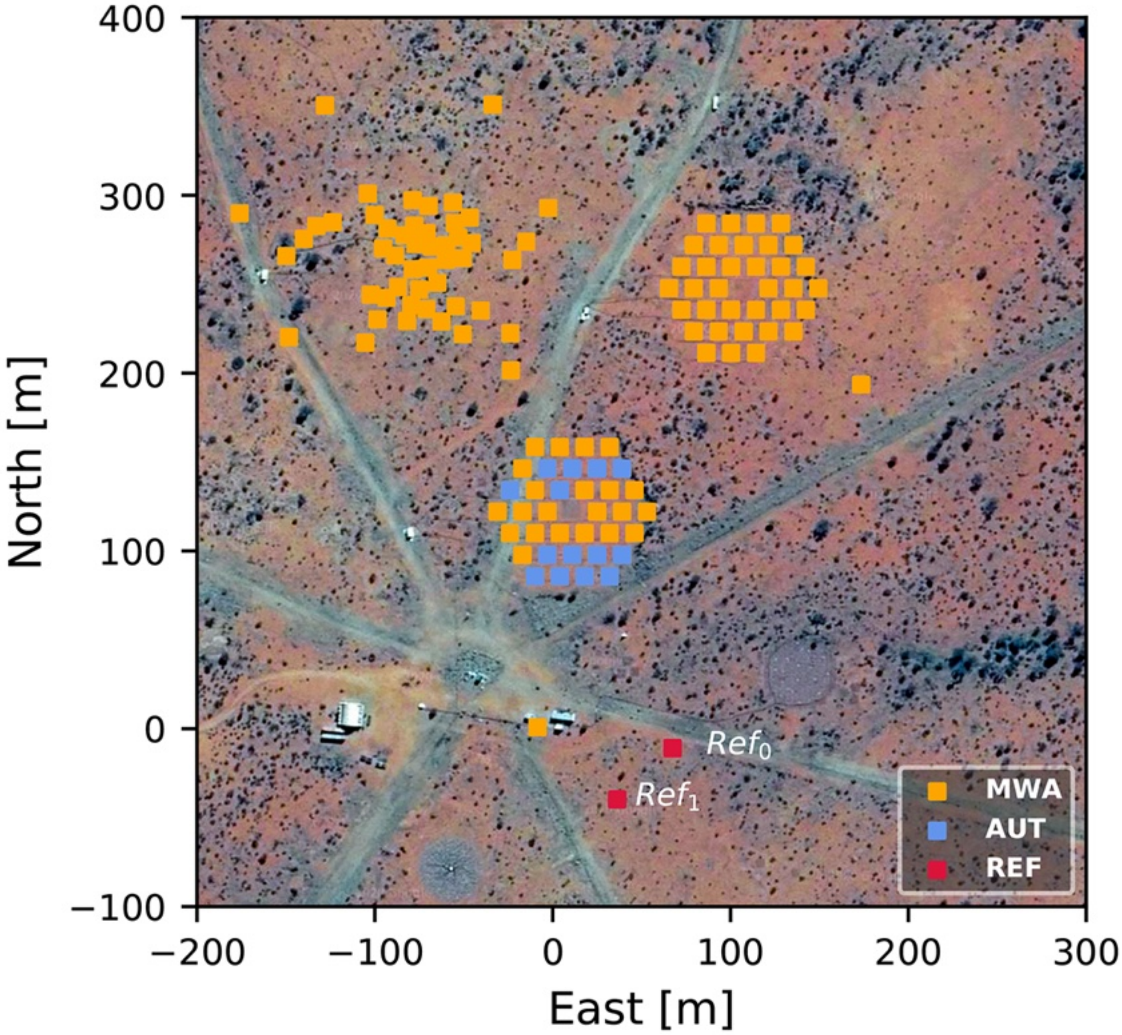

Figure 3.1: The positions of the AUTs (blue) and the Reference antennas (red). The ochre points represent the rest of the compact core of the MWA.

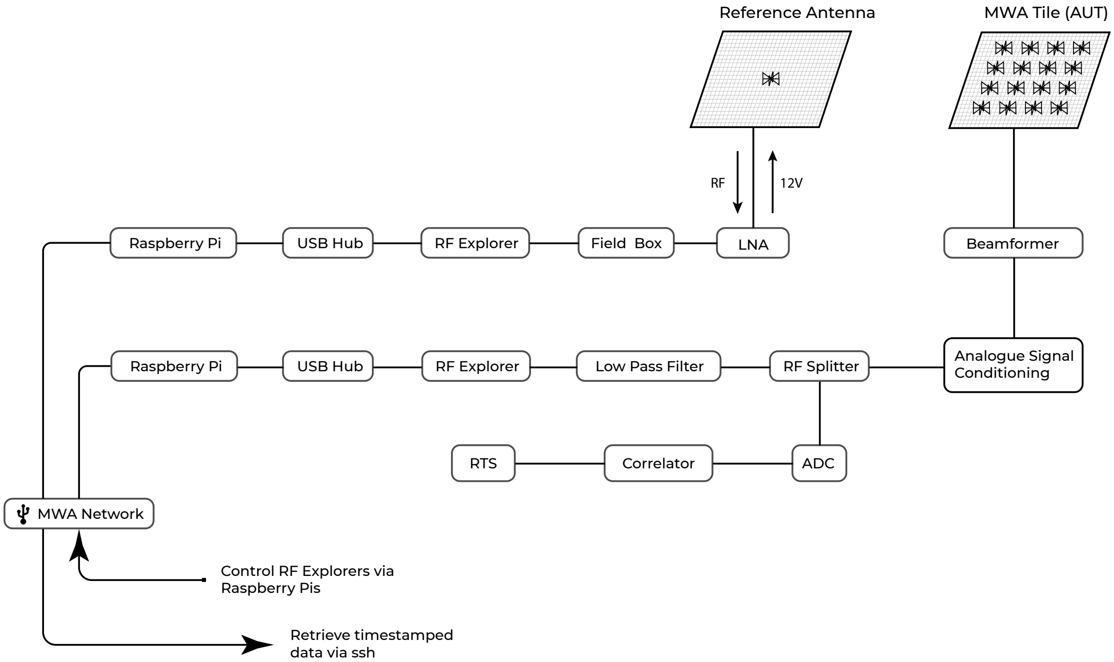

Figure 3.2: Flow chart of our experimental setup to measure MWA beam shapes. **Top:** The reference dipole receives satellite signals which is amplified by a Low Noise Amplifier (LNA). A Bias-T in the field box supplies the LNA with a 12V power supply and transmits the satellite signal from the dipole to the field box. Long coaxial cables carry the amplified signal to a RFI-shielded hut for analysis by a RF Explorer, the results of which are saved by a Raspberry Pi computer. **Bottom:** RF signals received by the Antenna Under Test (MWA Tile) are fed to an analogue beamformer, which introduces time delays to the signals from the 16 dipoles corresponding to the pointing of the telescope. The signals are combined and transmitted via long coaxial cables to an MWA receiver. Within the receiver, the Analogue Signal Conditioning unit performs amplification and filtering before passing it to a signal splitter. The splitter sends half the signal on its usual path to the correlator, while the other half passes through a low-pass filter before being analysed by a RF Explorer and saved by a Raspberry Pi. The USB hubs supply power to the RF Explorers and facilitates the transfer of data from multiple RF Explorers to the Raspberry Pi. The Raspberry Pis are connected to the MWA network, from which they can be remotely controlled and transfer data.

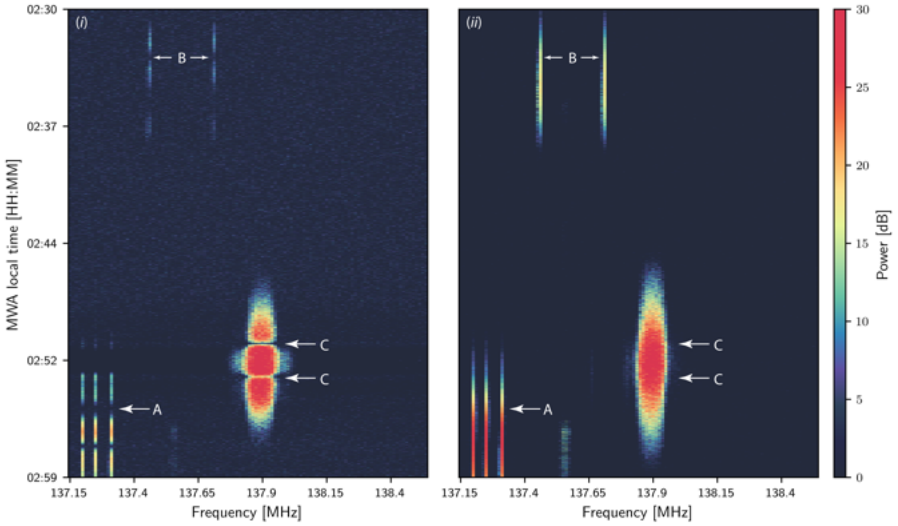

Figure 3.3: A sample set of raw data observed between 2:30AM and 3:00AM on 10/10/2019. The image on the left (i) is tile S10XX while the image on the right is data from reference ref0XX. Both sets of data have been scaled to have a median power of 0 with a dynamic range of 30dB. Interesting features have been annotated at the same positions in each plot with arrows indicating points of stark differences between the plots. The flux received by the MWA tile (i) drops to zero at the positions of the nulls at the edge of the MWA primary beam, which are absent in the reference antenna (ii). We find that ORBCOMM satellites generally have narrow band transmissions, occupying no more than 2 channels, as seen in A and B. Meteor weather satellites have significantly broader spectral footprints, occupying up to 10 channels, as seen in C.

3.4. Data Analysis

A sample of the raw data can be seen in Figure 3.3, in the form of a waterfall[*] plot. ORBCOMM satellites were found to transmit in narrow frequency bands, occupying up to two 12.5 kHz channels. In contrast, weather satellites exhibit a broader spectral signature, occupying up to 10 consecutive channels. In Neben et al. (2015), an ‘ORBCOMM user interface box’ was used to match satellite ephemerides to transmission frequencies of satellites above the horizon. As this technology is not commercially available, Line et al. (2018) used satellite ephemerides, published by Space-Track.org[†], to match satellites above the horizon to observed RF signals seen in waterfall plots similar to Figure 3.3 and manually create a map of ORBCOMM transmission frequencies.

Multiple ORBCOMM satellites are often above the horizon simultaneously, and are observed to periodically shift transmission frequencies to avoid inter-satellite interference. With observations spanning more than 6 months, and the resulting large volume of data it became infeasible to manually determine the transmission frequencies of every satellite pass. This necessitated the development of an automated system of matching satellite ephemerides and RF data, described in detail in Section 3.4.2.

[*] time vs. frequency

[†] https://www.space-track.org

3.4.1. *Data conditioning*

Before the analysis of our data can proceed, it must be pre-processed to ensure that sensible comparisons can be drawn between the tiles and references. A complication we encountered was that different RF Explorers recorded the data at different temporal rates, ranging between 6 and 9 Hz. We attribute this issue to two distinct batches of RF Explorers used. The first batch of 8 were purchased in 2017, and recorded data at a rate between 6-7 samples per second, while the remaining 24 RF Explorers were purchased in 2019 and recorded data at a rate between 8-9 samples per second. Though the model numbers of the RF Explorers and their configuration settings were identical, we infer that there must have been hardware improvements in the more recently manufactured modules.

An optimal balance between the RF Explorers sampling rate, Signal-to-Noise and the sky coverage of our selected satellites, determines the N-side of our HEALPix (Gorski et al., 2005) maps. We use a N-side of 32, corresponding to an angular resolution of 110 arcmins. An important consideration at this stage was that Satellites in Low Earth Orbit typically transit the visible sky in 5-15 minutes, depending on their orbital altitudes (Cakaj et al., 2009). Typical transit periods of satellites used in this experiment were observed to be in the 15 minute range, at which satellites took ~9 seconds to transit across one 110 arcmin HEALPix pixel.

The calculation above indicates that the raw data is highly oversampled, providing a certain leeway to get around the issue of varied temporal sampling. An iterative Savitzky–Golay (SavGol) filter is selected to smooth the raw noisy data, while preserving it's high dynamic range. Initially, a SavGol filter with a small window is used to preserve the depth of the null in the beam response, followed by a second SavGol filter with a larger window to smooth short time-scale noise present in the data. We then interpolate our data down to a 1 Hz frequency, while retaining multiple data points per HEALPix pixel. This enables us to compare our tile and reference data accurately. Figure 3.4 shows the concurrence between the raw data and the SavGol smoothed, interpolated data.

A noise threshold is defined at this stage, allowing further analysis to be limited to RF satellite signals above the noise floor. In a 30 minute observation, typically 3-7 of the 112 frequency channels contain satellite signals. These channels are identified to first order by having peak signals above a single standard deviation (σ_{raw}) of the data. Excluding these occupied channels, the Median Absolute Deviation (MAD*) σ_{noise} and the median μ_{noise} of the remaining noisy channels are used to define a noise threshold shown in Equation 3.2. The noise threshold for both P_{AUT} and P_{ref} is computed for every time-step with

$$P_{\mathrm{noise}} = \mu_{\mathrm{noise}} + \sigma_{\mathrm{noise}}. \tag{3.2}$$

If $P < P_{\mathrm{noise}}$ for either the AUT or reference data, the time-step data is flagged as "noisy".

As observations were carried out in parallel to the regular observational schedule of the MWA, satellite RF data is recorded at all pointings the telescope visited over the course of the experiment, accumulating over 4000 hours of raw data. The total integrated data at most pointings fell far short of the ~ 400 hours required to make maps with a N-side of 32. The Zenith and two EoR 2, 4 pointings met this criteria, resulting in ~ 1600

*MAD - robust statistic more resilient to outliers than standard deviation

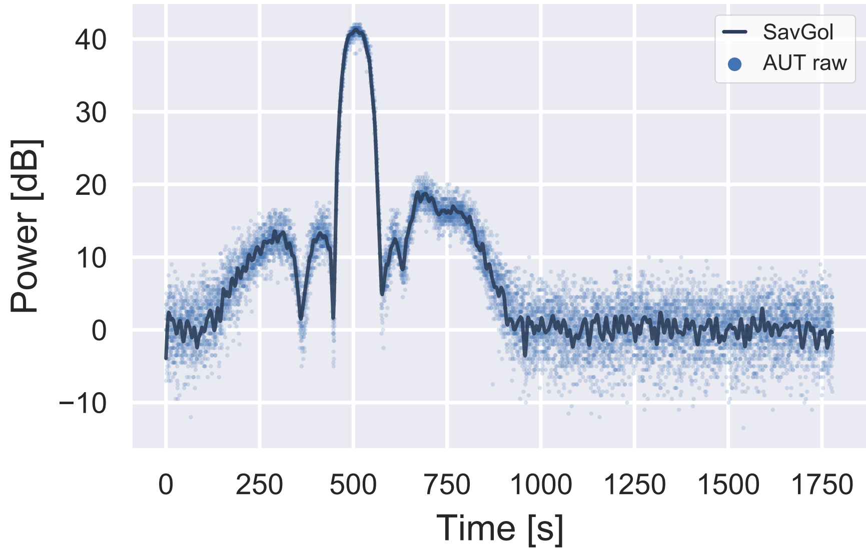

Figure 3.4: A single channel of raw data with a bright satellite pass. The solid curve is the SavGol smoothed data, interpolated down to 1 Hz.

hours of usable data. The data is sorted based on pointing, and separate maps are created for each. See Table 3.2 for details about the pointings and the amount of usable data collected at each.

3.4.2. Satellite ephemerides

Satellites transmit data to Earth on their allocated "downlink" frequency, the exact location of which are often proprietary. Reliable sources of data regarding spectrum allocations in the 137-138 MHz band are scarce and often outdated. Our initial estimate of ~ 70 active satellites within our window was optimistic, with a total of 18 satellites being regularly observed in our data. Some of our initial satellite candidates were no longer actively transmitting, while others presumably transmitting marginally outside our frequency window. Table 3.3 contains information on the satellites we used. The orbital parameters (ephemeris) of most satellites are recorded multiple times a day by USSPACECOM and are published by Space-Track.org. The ephemerides of our satellites are downloaded in the form of Two Line Elements* (TLEs). A custom `python` script reads these TLEs and accurately (within ~10 arcsec at epoch) computes when the satellites are above the horizon and their trajectories in the sky, at the MWA telescope . The `Skyfield`†(Rhodes, 2019) software package was instrumental to these calculations.

3.4.3. Frequency mapping

The sheer quantity of data made it infeasible to manually determine transmission frequencies of our satellites. Instead, we developed a method to automatically cross match satellite ephemerides and raw RF data, identifying the transmission frequency of every

*http://www.satobs.org/element.html
†https://rhodesmill.org/skyfield

Table 3.3: Satellite constellations and frequency bands.

Constellation	Spectral band [MHz]	Satellites observed
ORBCOMM	137.2 -137.800	15
NOAA	137.1 -137.975	2
METEOR	137.1 -137.975	1

satellite in each 30 minute observation. Using the ephemerides of each satellite, a temporal window within the RF data is identified, within which transmissions are expected to be found. We define a set of criteria to identify the correct frequency channel.

Window Occupancy: W_{RF} is the percentage of RF signal above the noise threshold P_{noise} (Eq. 3.2), within the temporal window. Identified satellites were required to have an occupancy in the range $80\% \leqslant W_{\mathrm{RF}} < 100\%$. The lower limit accounts for satellite passes close to the horizon, where long noise-like tails are observed on either end of the satellite data.

Power Threshold: P_{peak} is introduced to set a minimum peak satellite power. It was observed that channels adjacent to a bright satellite pass were often observed to be contaminated with lower power, noise-like, RF signals. This probably occurs due to transmission bandwidth marginally exceeding the 12.5 kHz channel width of the RF Explorers, leading to spectral leakage. Such channels typically have peak power in the range of 10-15 dB, compared to the 20-40 dB peak powers. To eliminate these contaminated channels, we require identified channels to have $P_{\mathrm{peak}} \geqslant 15\mathrm{dB}$.

Triplets: It is common to observe pairs or triplets of almost identical signal, as seen in labels A, B of Figure 3.3, which often pass both filters described above. In such cases, the channel with the higher window occupancy is selected, indicative of a superior match between RF data and satellite ephemerides.

While this method has been highly effective, it is not foolproof. At later stages in the analysis, described in Section 3.5.3, obvious errors in this method are eliminated by implementing a goodness of fit test between measured beam profile and the FEE simulated model.

3.4.4. *Map making*

FEKO simulations were run to create simulated beam models of the reference antennas B_{ref}, using on-site measurements of the ground screen and dipole positions, identical to those used to generate the FEE models of the MWA beam. These models are used to make maps of the tile responses by computing $P_{\mathrm{AUT}}/P_{\mathrm{ref}} \times B_{\mathrm{ref}}$ (Eq. 3.1) for each satellite pass, for every pair of AUT and Reference. The different amplifications that the RF signals undergo along the two distinct signal paths – through the field box for the reference data, and via the beamformer and the Analogue Signal Conditioning unit for the AUTs – have not been considered (see Figure 3.2). Since we are interested in the profile of the signal, rather than the absolute power, a least-squares method is used to assign each satellite pass, a single multiplicative gain factor G_{FEE}, effectively fitting it to power level of a corresponding slice of the FEE model.

This slice of the beam response is now projected onto a HEALPix map with a N-side of 32, using the satellite ephemerides, resulting in a map with an angular resolution of 110 arcmins, a good balance between integration per pixel and resolution. Each pixel of the map now contains a distribution of values from multiple satellite passes, the median of which gives us a good estimate of the beam response, without being influenced by outliers.

3.5. Results

3.5.1. *Null tests*

Two reference antennas ref_0 and ref_1, seen in Figure 3.5, were used in this experiment. This provides the ability to perform a null test to characterize the differences between the beam patterns of the references, and their FEKO simulated models. The ratio of the beam powers, for a set of perfect reference antennas, should ideally be unity and $P_{\text{ref}0}/P_{\text{ref}1} = 1$ should hold true for all satellite passes. Deviations from this expression are indicative of systematics such as alignment errors and imperfections in the ground screen, soil, dipole or the surrounding environment.

The results of the null test are shown in Figure 3.6. The first row (subplots (i)-(iv)) shows slices of the ref_0 HEALPix map along both East-West (EW) and North-South (NS) directions for XX and YY polarizations, respectively. The median of the distribution of values in each pixel is power $\text{P}_{\text{ref}0}$, while an estimate of the errors is determined from the Median Absolute Deviation σ_{MAD} of the distribution. These are compared to corresponding slices of the reference FEKO model B_{ref}, and the residuals $\Delta\text{ref}_0 = \text{P}_{\text{ref}_0} - \text{B}_{\text{ref}}$ are fit with a third order polynomial. The second row (subplots (v)-(viii)) is an identical analysis carried out for the ref_1 HEALPix map. The null test is performed in the third row (subplots (ix)-(xii)), where corresponding slices of ref_0 and ref_1 HEALPix maps are compared. The green data represents a pixel to pixel comparison between ref_0 and ref_1, with error bars propagated in quadrature from the σ_{MAD} of each references. We also compare the fits to the residual power Δref (orange curve), seen in the lower panels of the first two rows of Figure. 3.6.

An interesting pattern emerges in the residuals between the map slices and FEKO model Δref (Figure 3.6 (i)-(viii) lower panels). For zenith angles between $30° - 60°$, a systematic deficit of power is observed with residual power structure observed with deviations up to ± 2 dB from the FEKO reference models. This feature is investigated by summing the residuals of all four reference HEALPix maps and averaging the results in $2°$ radial bins. By classifying the data according to the progenitor satellite type, an illuminating pattern emerges, shown in Figure 3.7. We achieve a good fit of the radial residuals using a 8^{th} order polynomial. Each satellite has a distinct and well defined residual structure. These residuals represent a profile measurement of the beam shapes of satellite transmitting antennas. This can be understood by considering that satellites primarily focus on transmitting data downwards, normal to the surface of Earth. As satellites rise above the horizon, the reference antennas observe RF transmitted power convolved with the sidelobes of the satellite beam shapes, which is attenuated away from its primary beam (pointed to the surface).

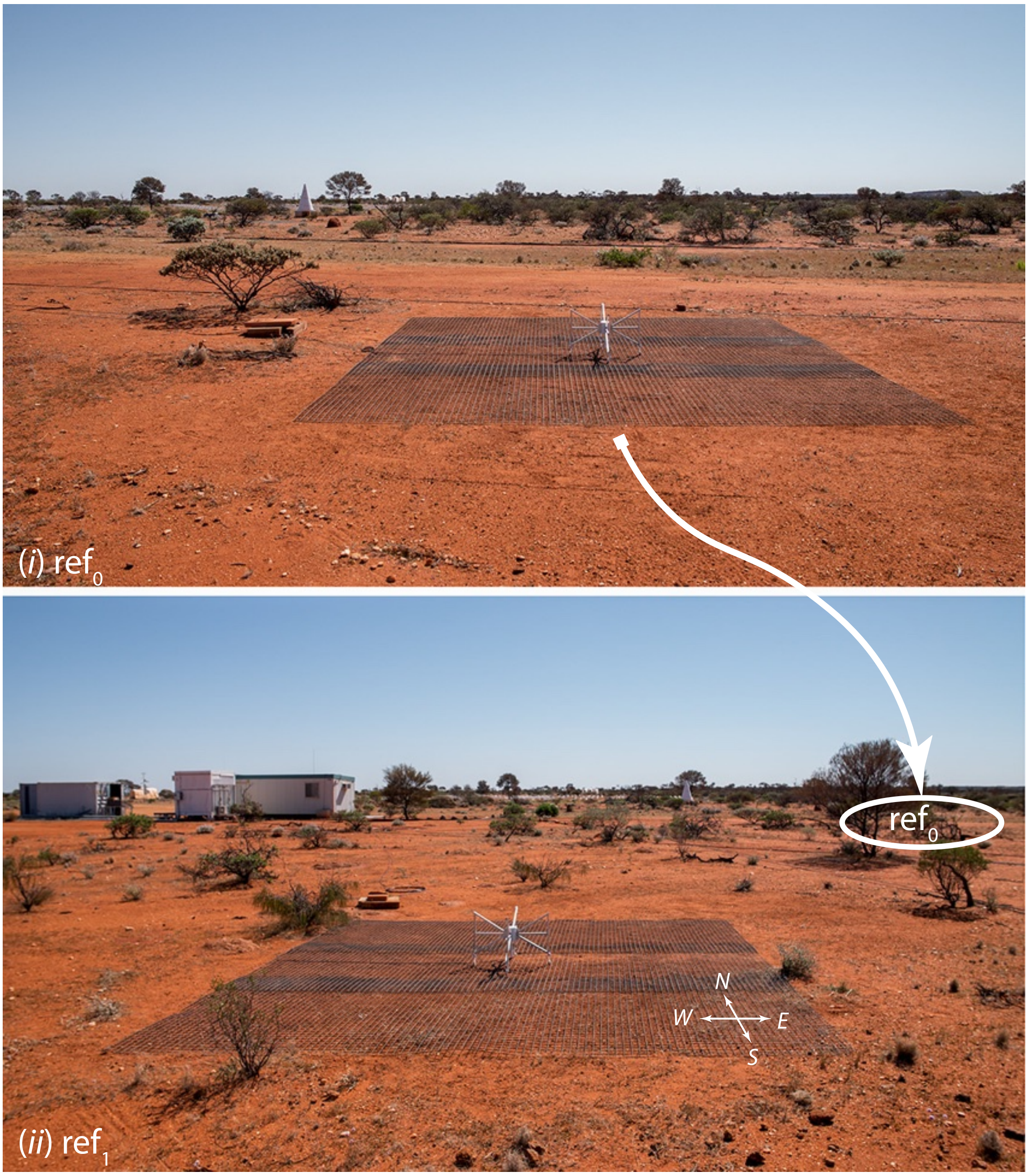

Figure 3.5: The reference antennas (i): ref_0 and (ii): ref_1 on site. In the bottom panel, the RFI shielded huts can be seen, as well as the position of ref_1 in the distance behind a bush.

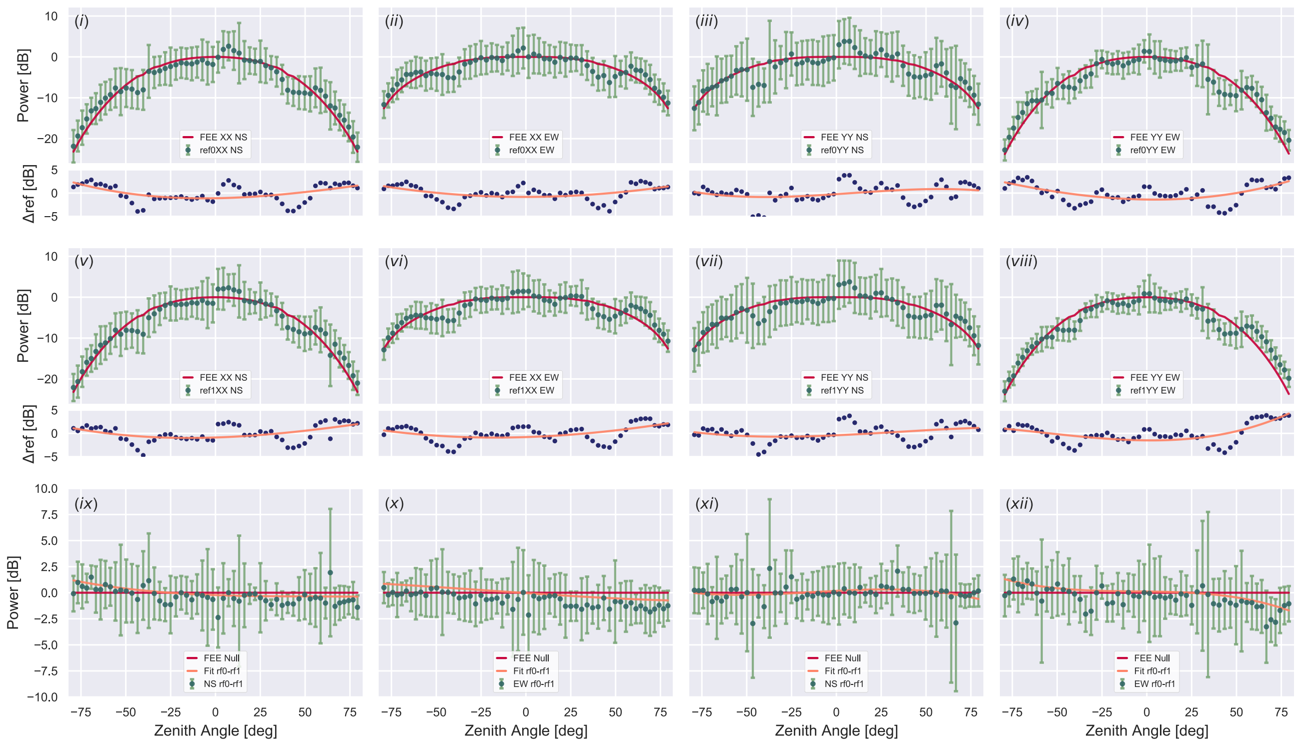

Figure 3.6: **Null Test Results:** The first row (i)-(iv) represent slices of HEALPix maps generated from RF data of ref_0. (i) and (ii) are North-South (NS) and East-West (EW) slices of the XX polarization of ref_0 while (iii) and (iv) are matching NS, EW slices of the YY polarization of ref_0. The green data-points indicate the median value of each HEALPix pixel, with the median absolute deviation as the error bars. The crimson curves represent corresponding slices of the FEKO reference model (Section 3.4.4). The difference between the data and model $\Delta\mathrm{ref}$ are plotted in the lower panel as blue points. The orange curve is a third order polynomial fit to the residuals. The second row (v)-(viii) show an identical analysis performed on ref_1. The bottom row (ix)-(xii) are the null tests, each computed from the two preceding plots. In (ix), the crimson line represent the the ideal null test while the green data represents the difference between ref_0 from (i) and ref_1 from (v). The error bars are computed by propagating errors from (i) and (v) while the orange curve shows a third order fit to the null test. (x)-(xii) are similar to (ix), each being calculated from the two plots above it.

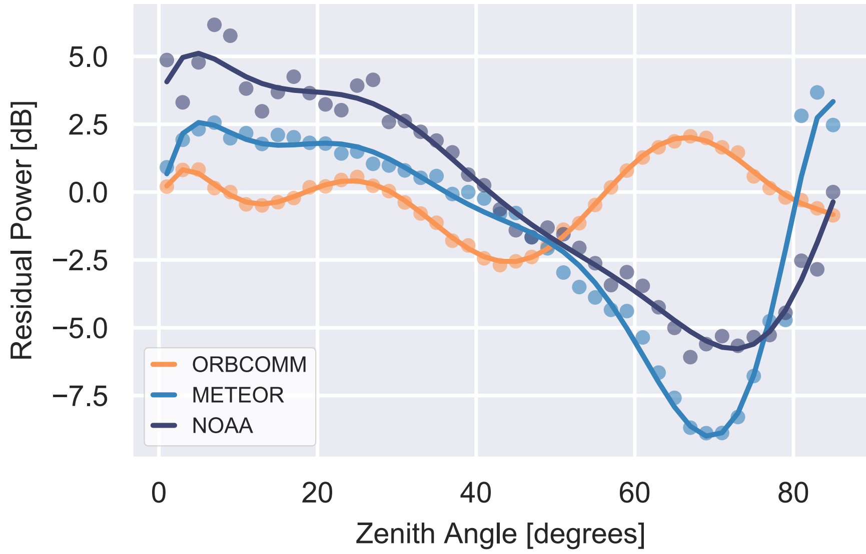

Figure 3.7: Radially averaged reference residual power, displaying unique beam profiles for each of the three types of satellites used in the analysis, validating our methodology and null tests.

The amplitude and structure of these residuals may appear significant to our analysis, but are in-fact accounted for by our primary Equation 3.1. This can be illustrated by considering the concurrent measurement of satellite data by both MWA and reference tiles. Any modulation encoded in the data transmitted by the satellites will be identically recorded by all antennas, convolved with individual tile beam shapes. The ratio of observed powers in Eq. 3.1 ($P_{\mathrm{AUT}}/P_{\mathrm{ref}}$) will neatly divide out any satellite beam structure or modulation encoded within the incoming RF data.

We note the slightly exaggerated slope in the null test of the EW slice of the YY reference maps, as seen in the last column of Figure. 3.6 (subplots (iv), (viii), (xii)). On further inspection of subplot (viii), we note that the East edge of the ref$_1$ receives ~ 2 dB less, and the West edge receives ~ 2 dB more power that the corresponding slice of ref$_0$. We suggest that this discrepancy probably results from a slight EW gradient in ground screen or the dipoles of the tile, which points the bore-sight of the dipole marginally off-zenith.

The agreement between the fits to the residuals (orange curve in subplots (ix)-(xii) of Figure. 3.6) and the expected null (red lines) represent a good validation of our experimental procedure described in section 3.3. We observe less than a ∼0.5 dB error in the central 25° of the reference model, corresponding to the primary lobe of the MWA beam at 137 MHz. These errors do increase as we move towards the horizon, reaching a maximum of ∼2 dB, in our most inaccurate reference. This validates the efficacy of our null test, in characterising systematic effects from the references, which propagate into the beam maps created in the following sections (see grey errorbars in Figure 3.12).

The null tests display a marginally better performance of reference tile 0 (ref$_0$). Despite this, we have chosen to use reference tile 1 (ref$_1$) in proceeding sections as hardware failures on ref$_0$ resulted in more data and better sky coverage for ref$_1$.

3.5.2. *RF explorer gain calibration*

During the last stages of the experiment, we noticed that the very brightest satellite signals exceeded the maximum recommended power of the RF explorers, resulting in the internal amplifiers entering a non-linear regime. Unfortunately, the limited dynamic range of the RF Explorers coupled with the high dynamic range of satellite observations resulted in almost no leeway for errors in this regard. This effect was only present in RF Explorers recording data from MWA tiles, via the MWA receivers and is apparent in Figure 3.8, where the light blue raw tile data is ~ 6 dB lower than a corresponding slice of the FEE model (yellow curve). This deficit of measured power in the primary lobe was unexpected as the primary lobe has been well characterized (Line et al., 2018) and validated by scientific studies which primarily use the primary lobe (e.g. Hurley-Walker et al., 2017) . The effort to recover the "missing" power led to the creation of a global gain calibration scheme.

It was observed that RF Explorers begin to leave their linear amplification zone at around -45 dBm* and were definitely non-linear by -35dBm, where slices of the FEE model had visibly diverged from raw tile data (see Fig. 3.8). We begin by considering deformed AUT power P_{def}, non deformed reference power P_{ref} and slices of the FEKO reference B_{ref} and FEE MWA beam B_{FEE} models for a satellite pass. Once Equation 3.1 is computed, information regarding absolute power recorded by the RF explorers is lost in favour of a normalized beam profile (see Section 3.4.4). Thus, gain calibration of the RF explorers must take place at the tile power level, before scaling or normalization processes distort the original power levels. A mask M_{def} is created using the region where the deformed tile power P_{def} exceeds -35dBm. This mask prevents the distorted sections of the measured primary beam from biasing the results of the multiple least-squares gain fits described below.

Equation 3.1 is used to compute the deformed beam slice B_{def} using P_{def}, P_{ref} and B_{ref}. To maintain the initial power level, we mask the deformed section of B_{def} using the mask M_{def} and use a least-squared method to determine a single multiplicative gain factor which will scale B_{def} down to the initial power level of P_{def}. A similar method is used to scale the slice of the FEE beam B_{FEE} down to the initial power level of P_{def}. The result of the scaling can be seen in Figure 3.8 where B_{FEE} (yellow) and B_{def} (light blue) have been successfully scaled to match at low powers while clearly displaying a deficit of power at the peak of the primary beam.

We can now empirically determine a gain calibration solution by looking at the residual power (B_{FEE} - B_{def}) of all satellite passes. The 2D histogram of all residual power is shown in Figure 3.9, with the horizontal axis representing power observed by the AUT RF explorers, and the vertical axis representing residual power. The figure displays a bridged bimodal distribution, which can be explained by considering the profile shape of cross sectional slices of the MWA beam models. The nodes at the edges of the primary beam are sharply peaked and extremely narrow, leading to a dearth of observational data points in such regions as satellites pass over them relatively quickly. The cluster of points at lower observed power is the result of satellites passing over the relatively broad secondary lobes of the MWA beam while the cluster at higher observed power comes from satellite passes transiting through the primary beam. For linear gain

*dBm - physical units of power, measured with respect to 1 milliwatt

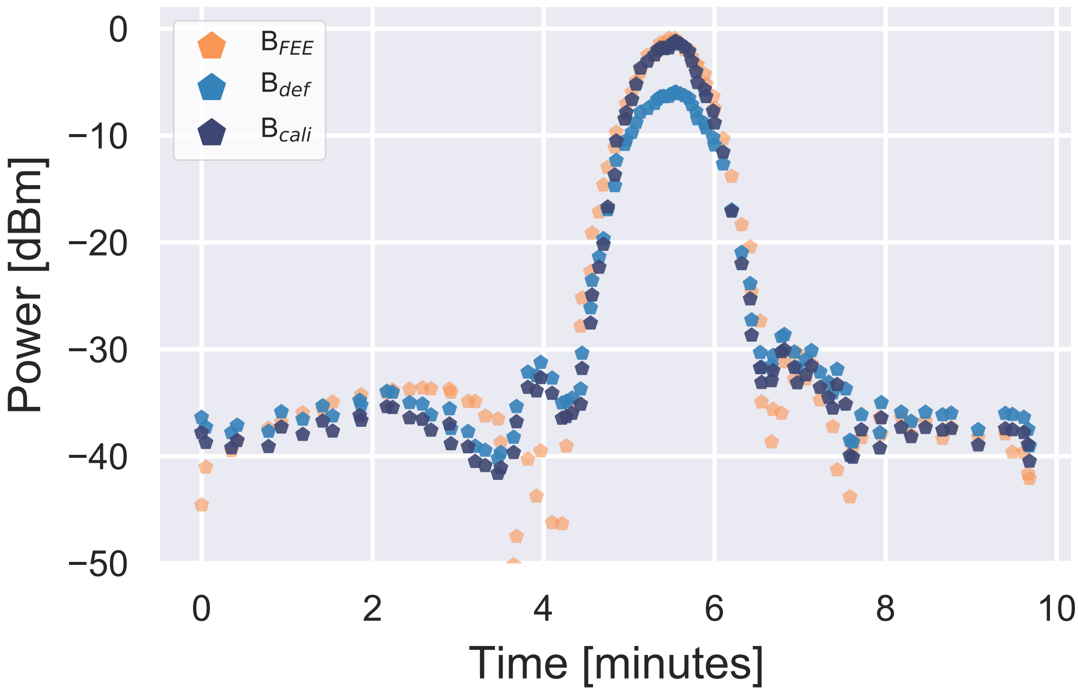

Figure 3.8: A bright satellite pass recorded by the non-linear gain of the AUT RF explorer, which results in a deformed beam model B_{def} compared to a corresponding slice of the FEE model B_{FEE}. The power of B_{def} is significantly lower than B_{FEE}, in the primary beam. The efficacy of the RF explorer gain calibration method is demonstrated by the dark blue data points B_{cali} which result from applying the gain calibration solution to the distorted beam model (light blue). The nulls of the FEE model extend beyond the depth of the recorded data due to the -50dB sensitivity of the experiment. A significant mismatch between B_{FEE} and B_{cali} is observed around the 4 minute timestamp. This error can probably be attributed to a combination of a gradient in the ground screen and a slight rotation of the tile, which lead to significant deviations around the edges of the steep nulls as explored in Section 3.6.

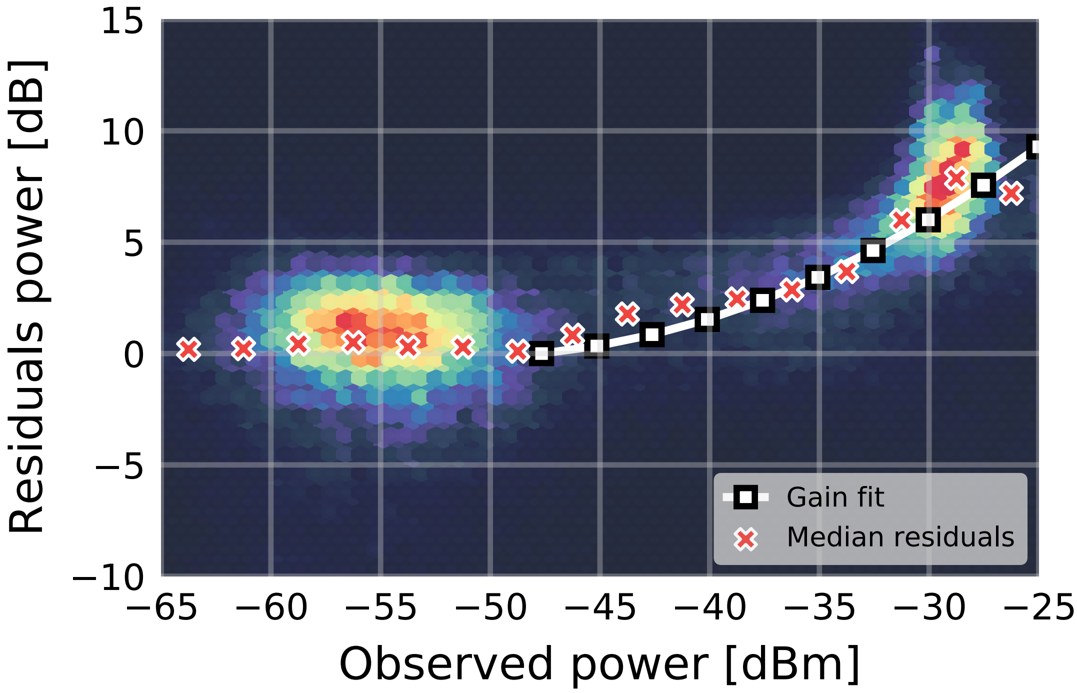

Figure 3.9: The 2D histogram distribution of high power distortions to RF signals. Ideally the residuals should have a value of 0 at all observed powers, indicating that the RF explorers reproduce input signals faithfully. The white curve is a 3^{rd} order polynomial fit to the median values (black squares) of the data binned in ∼ 4dBm intervals.

internal to the RF Explorer, one would expect the residuals to be ∼ zero, while positive residuals result from non-linear gains. The white curve and associated black squares are a 3^{rd} order polynomial fit to the median values (red crosses) of the data binned in ∼ 4dBm intervals. This clearly demonstrates that the RF explorers gradually enter the non-linear regime at ∼ −40dBm and exhibit residuals of ∼ 6dB at observed powers of −30 dBm.

The result of applying the calibration solution developed above to a single satellite pass are seen in Figure 3.8 where B_{def} (light blue) is scaled up to B_{cali} (navy blue) and represents a much better fit to a slice of the fee model B_{FEE} (yellow).

The RF Explorer gain calibration technique presented in this section has been shown to be necessary but comes with a minor drawbacks. Primarily, the global nature of our method could result in the loss of potentially interesting structure present at the center of the primary lobe. The accuracy of the primary lobe has been validated by multiple studies (e.g. Line et al., 2018; Hurley-Walker et al., 2017) and deviations are not expected. The gain correction was essential as the absolute scale of fluctuations in the more uncertain side-lobes, were determined by fitting satellite signals to the well characterized primary lobe. These corrections also enable us to regenerate all-sky beam maps which may be utilized in further studies. Future iterations of this experiment, which could be scaled to passively monitor the full MWA array or SKA-Low, will have to extensively characterize off-the-shelf components such as RF Explorers. Our characterization of the gain profile revealed that the accuracy of factory specification may not be sufficient for experiments of such sensitivity and scale.

3.5.3. *Tile maps*

We now create MWA beam maps using the method described in Section 3.4 with the caveat that the RF explorers gain calibration solution described in Section 3.5.2 are applied to all data from the AUT RF explorers. A single multiplicative gain factor, determined by least-squares minimization, is used to scale measurements to the level of the zenith-normalized FEE beam model. Before B_{AUT} can be projected onto a HEALPix map, it must pass a final goodness-of-fit test. The frequency mapping method described in Section 3.4.3 has been highly successful at dealing with the massive volume of data produced over the course of this experiment, but does exhibit an $\sim 2\%$ failure rate, where the transmission frequency of satellites is misidentified. To catch these final outliers, a chi-squared p-value goodness-of-fit test between the scaled measured beam B_{AUT} and the FEE model B_{FEE} is implemented, with a threshold tuned to ensure that only the beam profiles with obviously wrong null positions are rejected. Successful satellite passes are projected onto a HEALPix map representative of an accurate all-sky MWA beam response.

A set of tile maps at multiple pointings and polarisations are shown in Figure 3.10, created with data from tile S08 and Ref_1. The residual maps shown in the second and fourth row of Figure 3.10 display large gradients in power at the Southern and Eastern edges of their primary lobes. This effect is attributed to gradients in the ground screen of the MWA tiles. Such gradient can lead to systematic angular offsets from the intended pointing of the MWA tiles specified by the beamformers. This effect is most pronounced at the steep nulls surrounding the primary lobe where systematic displacements in null positions occur. The mismatch in the measured position of the nulls as compared to the FEE model manifest as the gradients observed in the residual maps of Figure 3.10.

We further investigate this effect to determine the gradient of the ground screens of our MWA tiles. This is achieved by displacing our measured beam maps and minimizing the residual power at the edge of the primary lobe. The gradient in the ground screens were determined to ~ 15 arcmin resolution by interpolating our HEALPix maps to a higher resolution with NSIDE=256. Figure 3.11 shows the measured angular offset of our 14 tiles from the zenith pointing. Local surveys of the tiles in the Southern Hex have identified a gradual half degree gradient in the soil, from the North-West to the South-East which would result in all beams being offset by $\sim 0.5^\circ$ towards the South-East, displayed as the black cross in Figure 3.11. This analysis shows a significant scatter in angular beam offsets, indicative of tile gradients ranging up to 1.4°, and vertical displacements exceeding 10 cm over a 5 m ground screen.

In Figure 3.12, NS and EW slices of the tile maps are compared to the corresponding FEE models. The first row (subplots (i)-(iii)) represent NS slices of the XX beam map of tile S08. The lower panels of these subplots explore residual power between measurements and the FEE model. The orange curve represents a 3^{rd} order polynomial fit to the residual power, while the cyan shaded regions account for errors which can be attributed to the reference tiles, as seen from the null tests (See Section 3.5.1 and Fig. 3.6). The second row (subplots (iv)-(vi)) represents an identical analysis for the EW slice of the beam maps. The last two rows (subplots (vii)-(xii)) complete the analysis described

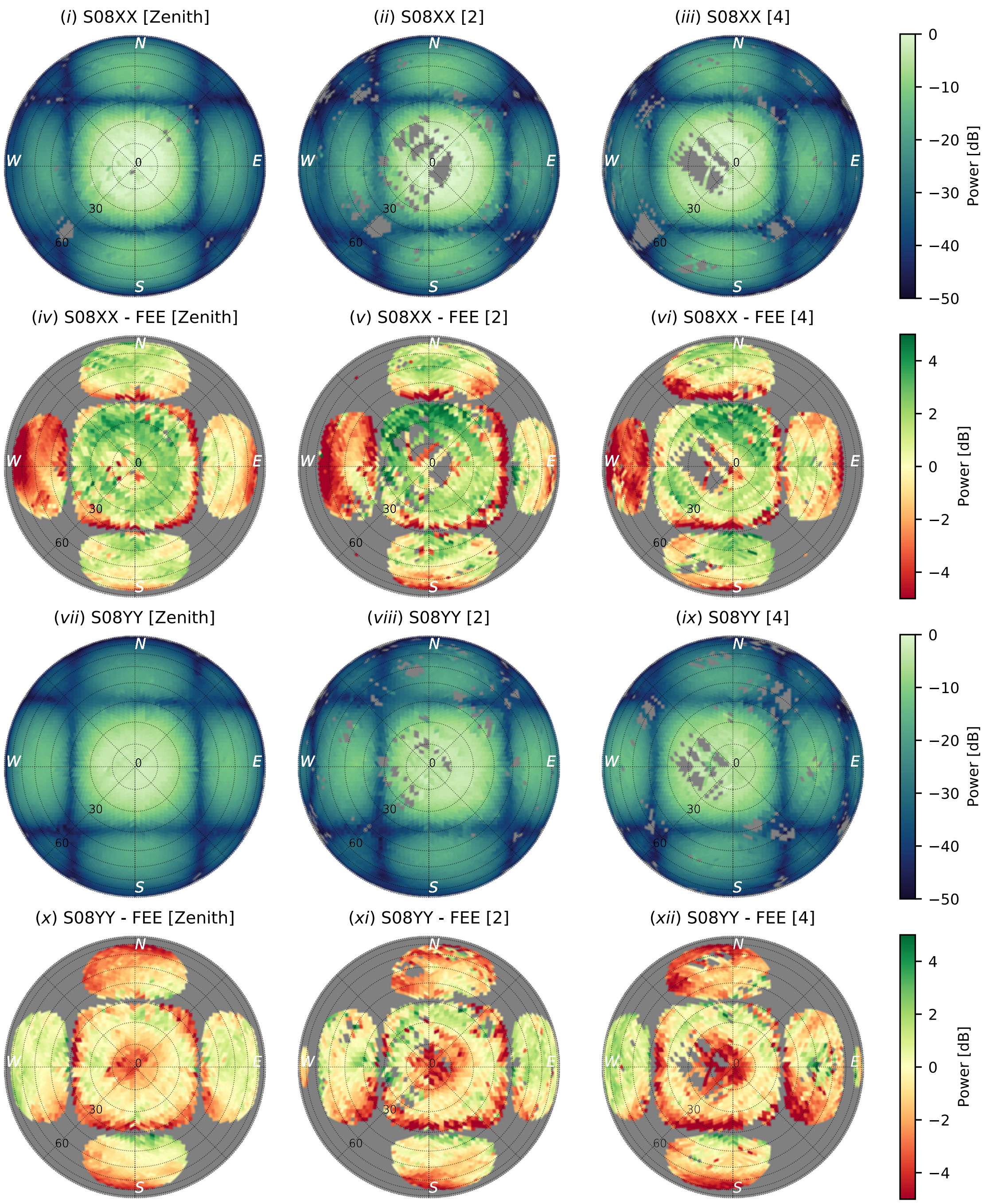

Figure 3.10: A set of beam maps measured for tile S08. The first row (i)-(iii) are maps of the XX polarization of tile S08, while the second row (iv)-(vi) represent the ratios between the beam maps and the corresponding FEE models. The three columns represent maps at the zenith, 2 and 4 pointing of the MWA. The last two rows (vii)-(xii) are an identical analysis for the YY polarization of tile S08.

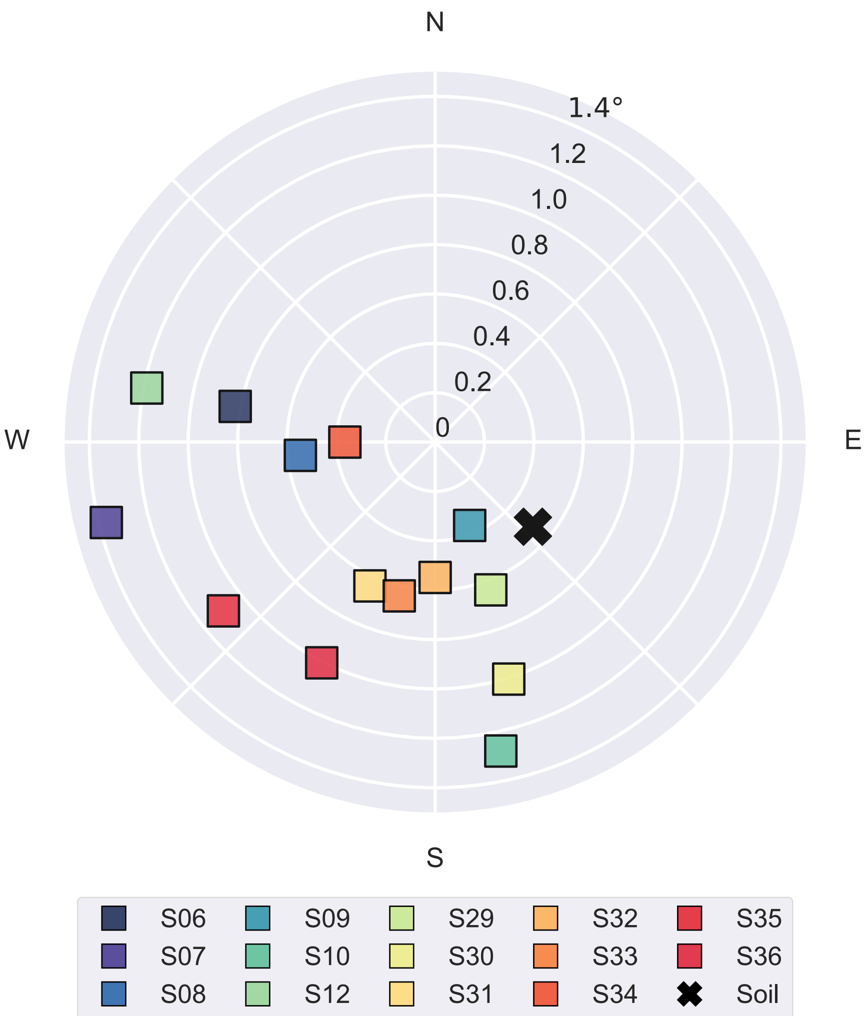

Figure 3.11: Measured angular offsets of zenith beam maps. The black cross represents a pervasive $\sim 0.5°$ gradient of the soil in the Southern Hex towards the South-East.

above, for the YY beam maps. The three columns represent the zenith and the 2 and 4 off-zenith pointings.

The distribution of beam shapes of our 14 tiles can been seen in Figure 3.13, displayed as cross-sections of the beam maps along the cardinal axes. The marginally larger scatter observed of data points around the primary lobes can be attributed the global RF Explorer gain calibration described in 3.5.2.

A subtle but interesting pattern emerges from Figures 3.12 and 3.13. Consider the first row of subplots, representing NS slices of XX beams. There is a slight excess of measured power (∼2dB) at the outer edge of the secondary lobes. XX dipoles are EW oriented and are most sensitive perpendicular to their physical orientation. Thus our measurements indicate a greater than expected sensitivity along the most sensitive axis of the XX dipole. Similarly, the YY beam oriented along the NS, measures an excess of power along its most sensitive axis (EW) as seen in the fourth rows of Figures 3.12 and 3.13. Conversely, the power measured by the dipoles along their least sensitive axis, parallel to their physical orientation, is less than expected. This is seen in the second and third rows of Figures 3.12 and 3.13.

This effect was investigated by computing median residual power for all 14 tiles along EW and NS slices. The results shown in Figure 3.14 (*i*) have been fit with a 2^{nd} order polynomial which shows systematic, radially dependent offsets. This residual structure could potentially be attributed to a rotation of the reference antenna. This scenario was explored using the simulated FEKO models of the reference, as shown in Figure 3.14 (*ii*). The solid lines represent the residual power which would be measured along a NS slice of the XX MWA beam if the reference tile was rotated by a range of angles, while the dashed lines represent the EW slices. As observed in Figures 3.12 and 3.13, the excess measured power along the most sensitive axis of the dipole and the deficit of power along the least sensitive axis of the dipoles seem to have similar shapes to the simulated residuals of reference antenna rotations. Unfortunately, the degeneracy inherent to the symmetric reference FEKO models prevents the identification of the direction of this rotation.

The measurements of the western sidelobe of tile S08 show a significant deficit in power of order ∼4 dB, seen in the second row of Figure 3.10. Pictures of the in-situ condition of the tile reveal potential environmental factors which could potentially be responsible. In Figure 3.15, we observe a number of large rocks on the ground screen of the tile. Additionally, the harsh weather conditions on site seem to have swept some loose soil onto the ground screen, partially obscuring the metal mesh. Both these effects are most prominent along the western edge of the tile and could plausibly explain the measured deficit of power.

3.6. Conclusions

We have measured the all-sky beam response of 14 onsite MWA tiles, at both instrumental polarizations and at three pointings. As the first dual polarization MWA beam measurement experiment, both our XX and YY beam maps display good agreement with the cutting-edge FEE beam models (Sokolowski et al., 2017) to first order. Further investigations reveal a range of environmental perturbations from the FEE models, which may present the scope for improved calibration for EoR and other science cases.

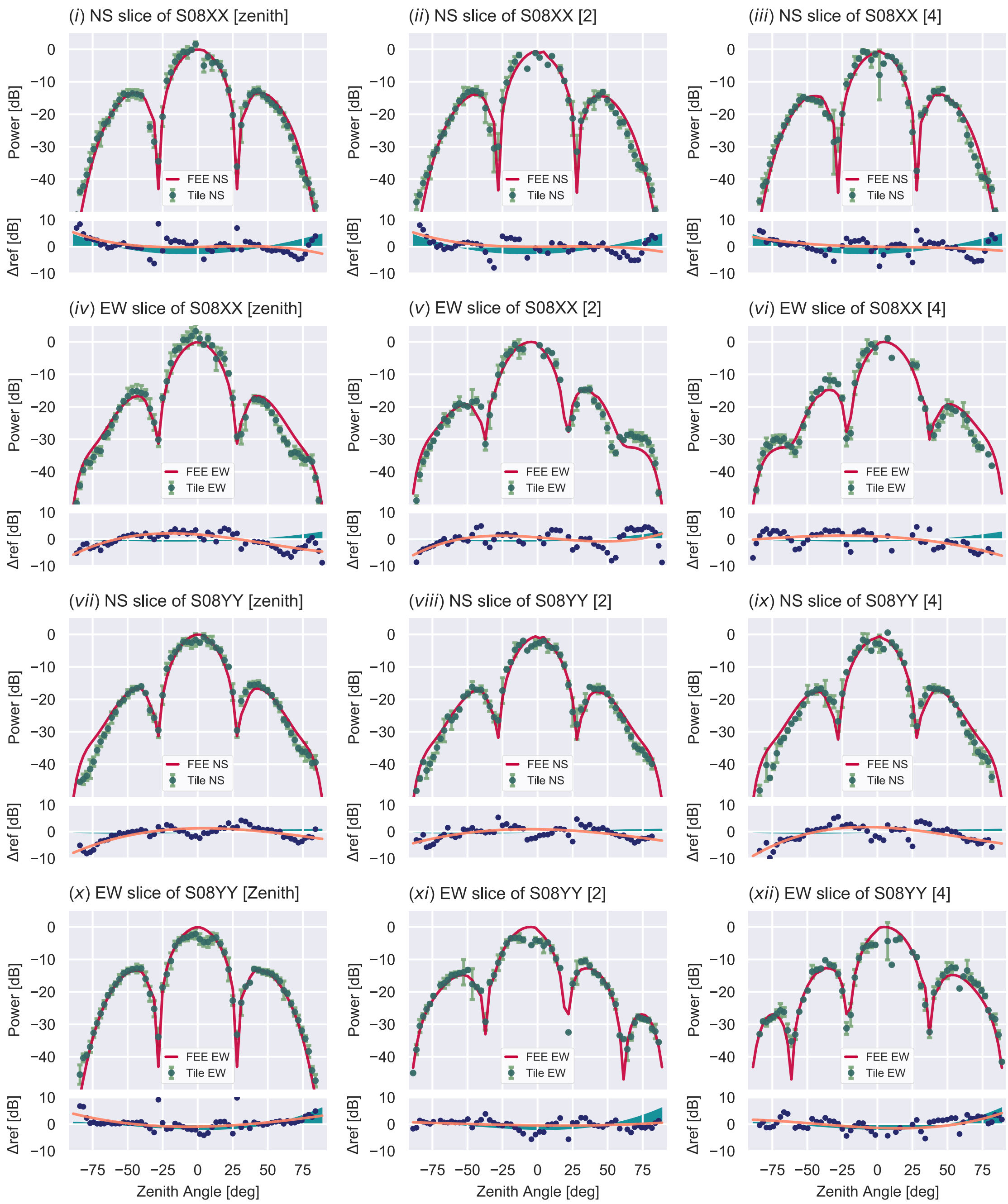

Figure 3.12: North-South(NS) and East-West(EW) slices of beam maps (S08) presented in Figure. 3.10. The first row (i)-(iii) displays NS slices of tile S08 compared to corresponding slices of the FEE model, in the XX polarization and at three pointings. The lower panels show the residuals between the measured tile maps and the FEE models, with the cyan shaded regions representing errors which can be attributed to the reference antennas. The second row (iv)-(vi) display EW slices of S08XX. The bottom two rows (vii)-(xii) represent an identical analysis for the YY polarization of tile S08.

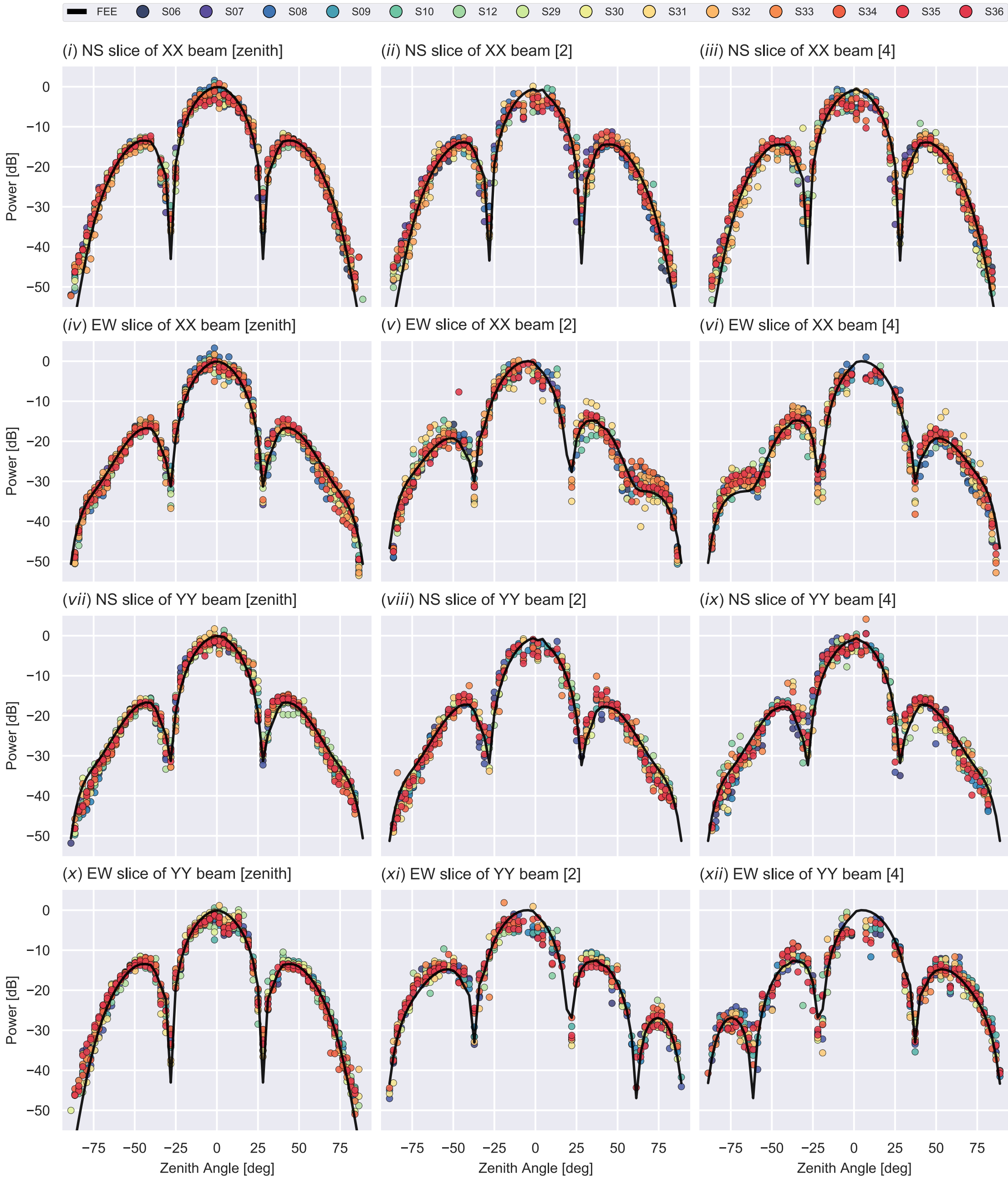

Figure 3.13: Distribution of all beam maps compared to corresponding slices of the FEE beam. The three vertical columns represent the Zenith, 2, 4 MWA pointings, while the horizontal rows represent cardinal (NS, EW) slices of beam maps at both polarizations (XX, YY).

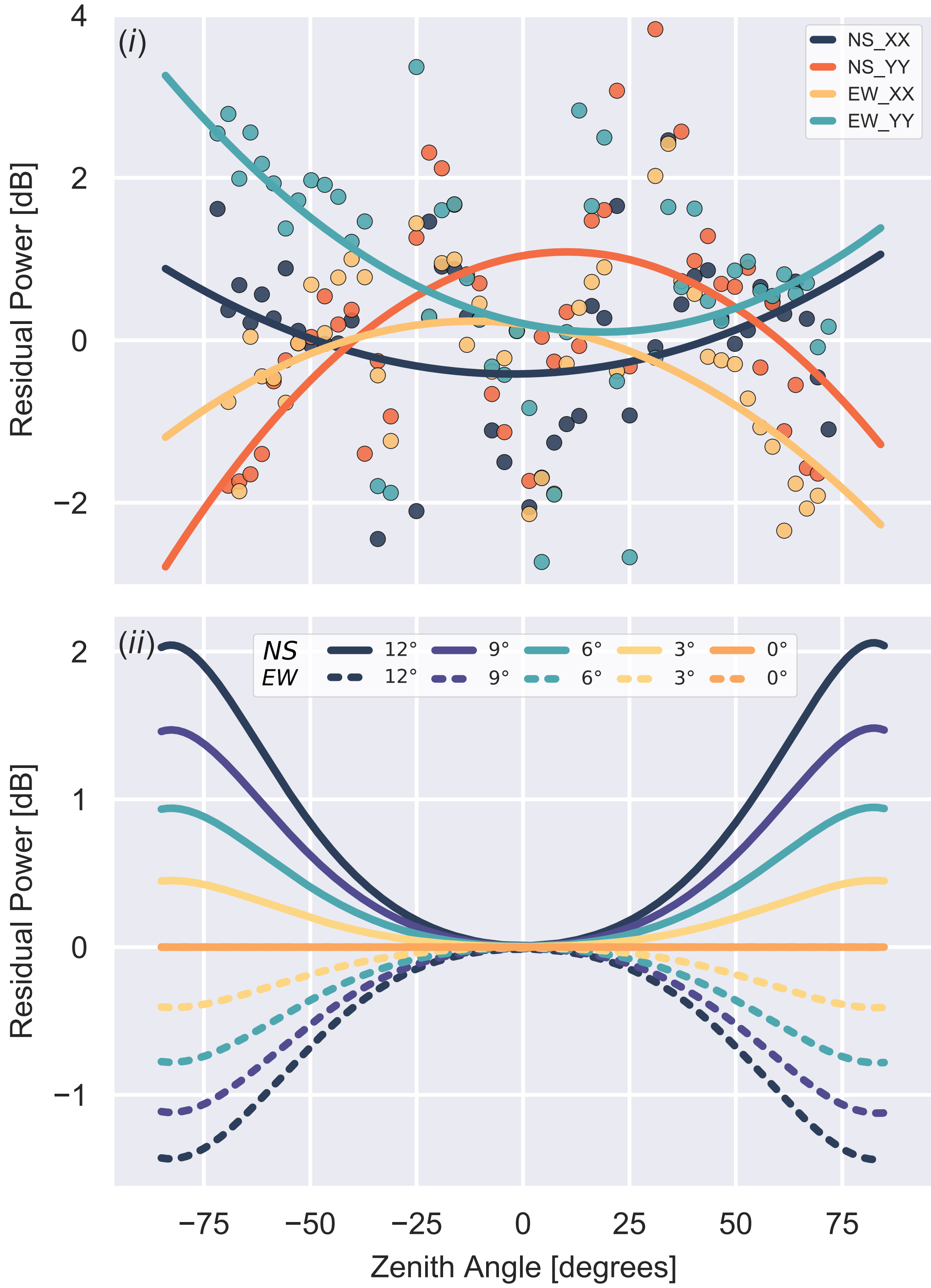

Figure 3.14: (*i*) Global residual power averaged over all 14 tiles. Each point represents the median power at various zenith angles, along cross-sectional slices of residual power between measured MWA tile maps and the FEE model. Second order polynomials fit to this data reveal systematic offsets attributed to rotations in the reference tiles. (*ii*) Simulated effect of anticlockwise rotation in the XX reference tile on measurements of MWA tile power. The solid and dashed lines represent North-South and East-West cross-sectional slices of the beam model.

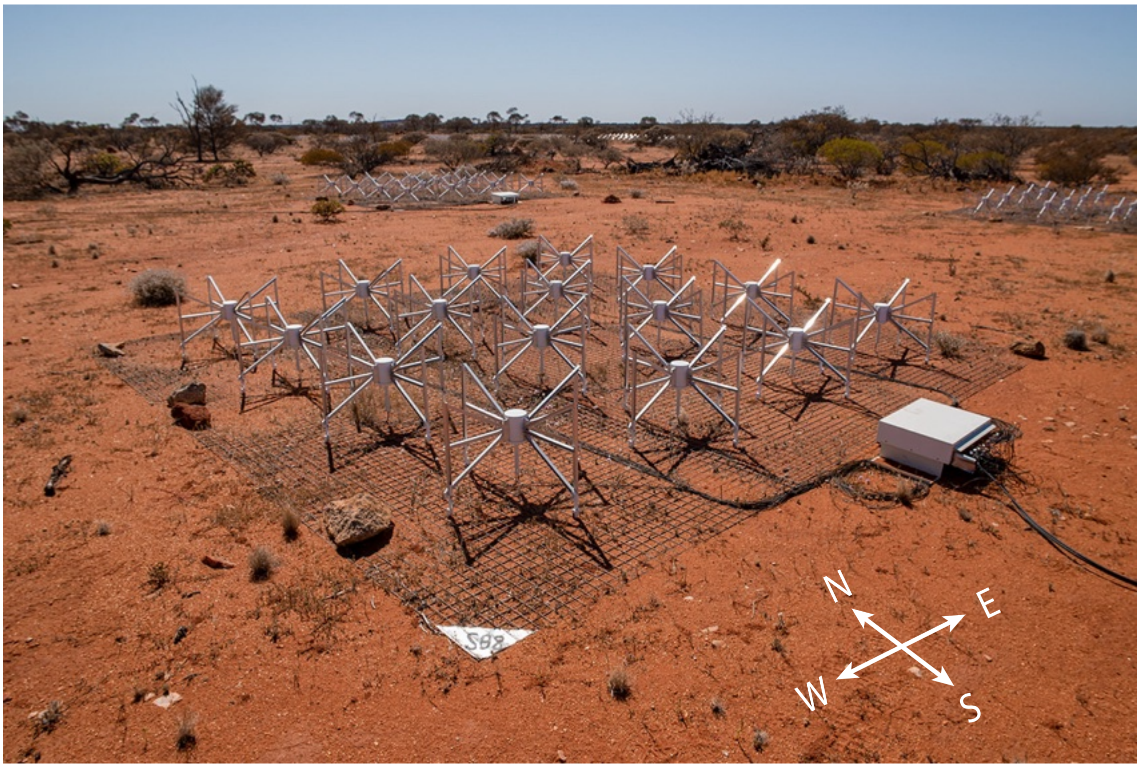

Figure 3.15: A current image of the condition of tile S08 reveals several large rocks on the western edge of the ground screen as well as a significant amount of loose soil which has covered portions of the metal mesh of the ground screen.

The most significant distortions to the MWA beams are found to be asymmetric and in one or more of the sidelobes. These distortions have been observed to occur due to environmental effects such as the obscuration of the metal mesh of the ground screen by loose soil, and other large objects such rocks (see Figure 3.15). Further, local foliage surrounding the tile may also contribute to beam deformations in an unpredictable, non-static manner as they grow and wither over the course of a year. These effects have been seen to deform the sidelobes with up to a $\sim$ 5dB deficit in measured power. Such effects are at the level of $\sim 10\%$ zenith power and could have a serious effect on multiple science cases.

Further, investigations into the mismatch of positions of the primary nulls have revealed the effects of gradients in soil and ground screens. The Southern Hex is known to have a 0.5° gradient in the soil from the NW to the SE. Our investigation revealed the existence of local soil gradients, beyond the gradual background gradient, up to $\sim 1.5°$, scattered around the local gradient (see Figure 3.11). This effect results in the bore-sight of the MWA beam pointing slightly away from its expected position, and is analogous to pointing errors in traditional telescopes. While these effects do not significantly effect the central portion of the primary lobe, the steep edges of the beam surrounding the nulls are susceptible to large power offsets, approaching $\sim$ 8dB, with pointing offsets as low as $\sim 1.5°$. This may be of particular import to observations conducted during the day, where clever observation techniques are used to place the sun in one of the primary beam nulls and achieve maximum attenuation (Morgan et al., 2019). Positional offsets of the nulls could potentially introduce significant erroneous solar flux to such observations.

Finally, unexpected deviations from measured power, along and perpendicular to dipole axis have revealed rotations in our reference tiles. Degeneracies resulting from symmetries in the reference antenna beam models have prevented the exact identification of the direction of this rotation. While the rotation of the reference tile does not affect MWA science cases, it does present an interesting proxy to study effects rotations in MWA tiles may have. MWA tiles are aligned to within 0.5-1.0° of the NS meridian. We estimate that such uncertainties in rotation may introduce error less than $\sim$ 1dB close to the horizon. Such effects do not significantly effect the primary lobe but increase radially outwards. Interferometric arrays such as the MWA are prone to flux leakage, which may be exacerbated by rotational errors which will increase the coupling between the orthogonal, independent dipoles. With better calibration of reference antennas, future versions of this satellite experiments will be able to measure rotations of MWA beams, enabling studies of the effects of tile rotations and place upper limits on the acceptable leeway in beam rotations. More comprehensive simulations of such effects have been reserved for future work.

These measurements provide useful insight to various beam deformations, but are limited to an extremely narrow frequency band. This is an apparent shortcoming of satellite based beam measurement techniques and presents a significant impediment to the adoption of satellite based beam maps by the radio astronomy community. So far, the utility of such methods has been limited to the validation of advanced electromagnetic simulations. Future work based on our measured beam maps will investigate the fitting of 32 complex-valued gain parameters of the FEE model (Sokolowski et al., 2017) to create perturbed FEE models representative of measurements at 137 MHz. Future investigations will explore the efficacy of extrapolating these gain values to cover the MWA's frequency band, potentially opening an avenue for broadband, pseudo-realistic beam models. Finally, a study combining our measured beam maps and data from the regular short dipole tests, used to find dead dipoles, may enable the creation of more realistic beam models for use with archival MWA data.

The implications of more accurate beam models are far-reaching. The detection of the EoR and studies of the cosmic dawn are key science cases of the MWA and upcoming telescopes such as the SKA-Low. The extreme dynamic range of such experiments necessitate uncompromising precision, which may be impeded by imperfect beam models. Particularly, imperfect beam models with radially increasing uncertainty can result in flux calibration errors of bright sources such as Fornax A, and the diffuse galactic plane, close to the horizon. The intrinsic chromatic nature of radio interferometers can be exacerbated by in-situ beam distortions. Such effects could lead to the introduction of bright, unphysical spectral structure, impeding the detection of the EoR signal (e.g. Byrne et al., 2019; Orosz et al., 2019).

Large precise surveys such as GLEAM (Hurley-Walker et al., 2017), along with planned surveys such as GLEAM-X and LoBES, use the half-power portion of the central lobe. This has primarily been necessary due to beam modelling errors, and results in a loss of sensitivity and survey efficiency. Instruments such as the MWA are sensitive to large portions of the sky, and approach all-sky sensitivity at low frequencies. Increased confidence in beam models would enable larger swatches of the sky to be observed at a time. Additionally, unresolved sources in the sidelobes contribute to confusion-noise, place lower limits on sensitivity to faint sources.

This experiment has demonstrated the feasibility of a passive parallel monitoring system, built from off-the-shelf and relatively inexpensive components, which could easily be scaled up to monitor the beam shapes of the entire MWA array, providing invaluable information to many science cases and improving calibration across the board. Using individual tile models for calibration of MWA data is possible using pipelines such as the RTS and FHD, but presents a significant increase in computational effort. The level of measured beam distortions and their complex nature reinforces our conjecture that more realistic beam shapes could significantly improve the accuracy and sensitivity of science possible using the MWA. Further investigation and detailed simulations will be necessary to understand how realistic beam models will effect calibration and improve results. If successful in improving calibration, a similar passive parallel monitoring system may be an essential tool for upcoming telescopes. This is particularly applicable to SKA-Low stations constructed of 512 dipoles, with multiple degrees of freedom available for complex beam perturbations.

This experiment has led to the development of an open-source `python` package called EMBERS[*] – Experimental Measurement of BEam Responses with Satellites. EMBERS is almost completely parallelized and is capable of being scaled to much larger arrays, enabling an end-to-end analysis of satellite beam measurement data. EMBERS can be used and modified by anyone, with the aim of enabling the measurement of beam shapes of radio telescopes all over the world with ease.

[*] https://embers.readthedocs.io

CHAPTER 4

The Necessity of Individually Validated Beam Models for an Interferometric Epoch of Reionization Detection

This chapter is based on

A. Chokshi, N. Barry, J. L. B. Line, C. H. Jordan, B. Pindor, R. L. Webster
Monthly Notices of the Royal Astronomical Society, 534, 3, 2024, 2475

reformatted with the following changes only:

- **The text is styled and restructured to match the rest of this thesis.**
- **Where necessary, bibliographic records are updated.**

4.1. Abstract

A first statistical detection of the 21-cm Epoch of Reionization (EoR) is on the horizon, as cosmological volumes of the Universe become accessible via the adoption of low-frequency interferometers. We explore the impact which non-identical instrumental beam responses can have on the calibrated power spectrum and a future EoR detection. All-sky satellite measurements of Murchison Widefield Array (MWA) beams have revealed significant sidelobe deviations from cutting-edge electromagnetic simulations at the $\sim$10% zenith power level. By generating physically motivated deformed beam models, we emulate real measurements of the MWA which inherently encode the imprints of varied beams. We explore two calibration strategies: using a single beam model across the array, or using a full set of deformed beams. Our simulations demonstrate beam-induced leakage of foreground power into theoretically uncontaminated modes, at levels which exceed the expected cosmological signal by factors of over $\sim$1000 between the modes k=0.1-1 $h\mathrm{Mpc}^{-1}$. We also show that this foreground leakage can be mitigated by including measured models of varied beams into calibration frameworks, reducing the foreground leakage to a sub-dominant effect and potentially unveiling the

EoR. Finally, we outline the future steps necessary to make this approach applicable to real measurements by radio interferometers.

4.2. Introduction

The past decade has seen the adoption of relatively simple, large interferometric arrays as powerful tools for the investigation of the low-frequency radio sky. These aperture arrays are generally constructed from sets of simple metal dipoles, coherently synthesised to achieve high angular resolution imaging over unprecedented wide fields-of-view. Such telescopes are often designed to have a large number of receiving elements (tiles or stations), each constructed from a number of identical dipoles, with theoretically identical sensitivities across the sky.

Low-frequency radio interferometers with large collecting areas can sample many modes on the sky, allowing them to search for faint, cosmic signals. The Murchison Widefield Array (MWA, Tingay et al. 2013; Wayth et al. 2018), the Hydrogen Epoch of Reionization Array (HERA, DeBoer et al. 2017), the New Extension in Nançay Upgrading LOFAR (Nenufar, Zarka et al. 2020; Munshi et al. 2024), the Low Frequency Array (LOFAR, van Haarlem et al. 2013), and the Long Wavelength Array (LWA, Eastwood et al. 2019) are all searching for cosmic signals below 200 MHz.

Understanding the telescope's varied sensitivity across the sky, or primary beam response, is a crucial part of the inherent calibration process. Beam sensitivity measurements show that this often differs from the instrumental simulations, especially in attenuated parts of the beam. Sensitivity measurements have been made with the MWA (Bowman et al., 2007; Neben et al., 2015; Line et al., 2018; Chokshi et al., 2021), with LOFAR (Ninni et al., 2020), and with HERA (Neben et al., 2016b; Nunhokee et al., 2020).

Ideally, the beam shape of each interferometric station or tile is identical, enabling massive computational simplifications during beam calibration. However, the realities of dipole failure and other environmental perturbations breaks this assumption (e.g. as measured by Line et al. 2018; Chokshi et al. 2021) and requires more complicated calibration schemes to be considered in the pursuit of high fidelity science. This may prove costly for extremely large arrays, especially future telescopes like the Square Kilometre Array (SKA-Low, Mellema et al. 2013; Koopmans et al. 2015).

The precision of calibration is particularly crucial for power spectrum measurements of the 21-cm Epoch of Reionisation (EoR) signal. This cosmological, redshifted signal is expected to be up to five orders of magnitude fainter than the various foregrounds (see Figure 4.1) (e.g. Oh & Mack, 2003; Santos et al., 2005; Pober et al., 2013; Yatawatta et al., 2013), but will naturally separate in Fourier space due to its varying spectral structure. However, calibration can impart varying structure on otherwise spectrally smooth foregrounds, clouding the EoR measurement (e.g. Barry et al. 2016; Patil et al. 2016; Byrne et al. 2019).

Calibration errors in the context of beam variations have been explored within simulation. Redundant calibration, where tile parameters are reduced from multiple measurements of the same mode, is particularly susceptible to variations in antennas and their placement (Joseph et al., 2018; Orosz et al., 2019; Choudhuri et al., 2021; Kim et al., 2022). Sky calibration, where tile parameters are reduced from comparisons between measurements and full-sky models, is also affected by unaccounted broken dipoles within tiles

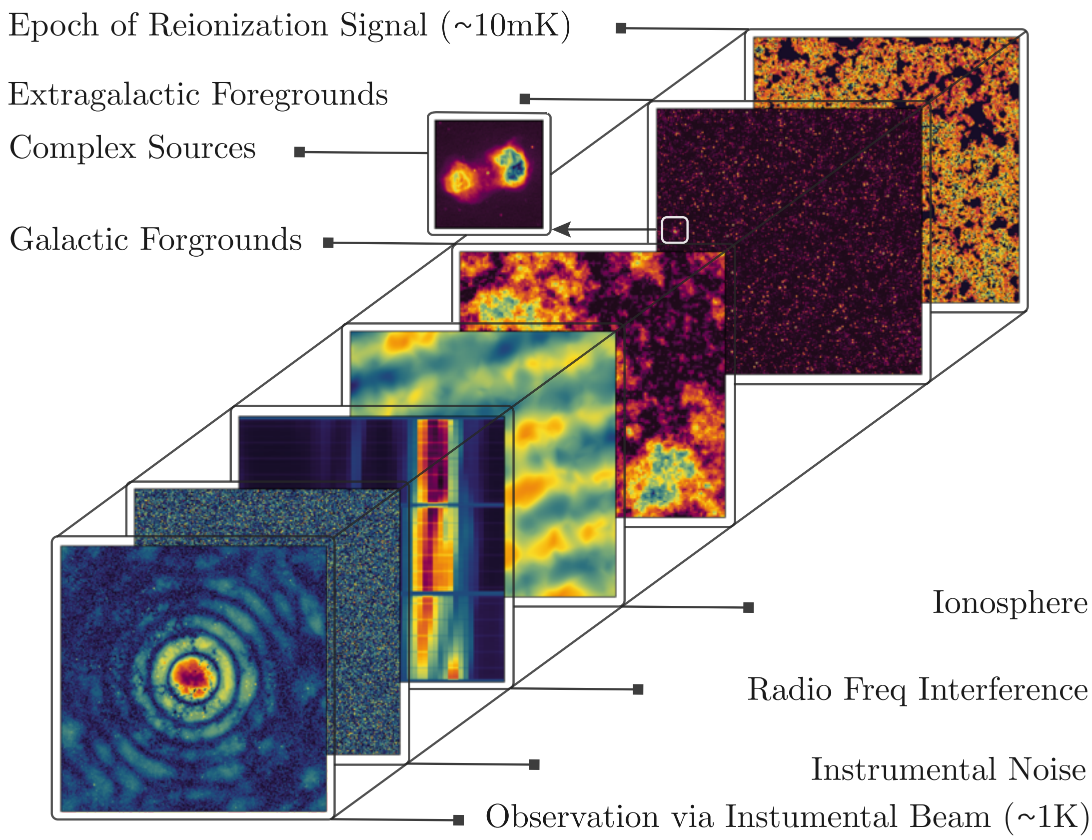

Figure 4.1: A schematic representation of the primary contributing components captured in an standard EoR observation (inspired by figures in Jelić et al. 2008), spanning five orders of magnitudes from the faint cosmological signal, to foreground, terrestrial and instrumental effects.

or stations (Joseph et al., 2019). Given the computational complexity of unique beams in analyses, these studies explore discrete variations.

We show a more complete picture of the effects of beam variation within sky calibration of MWA Phase II, using actual beam measurements to inform our simulations. We have 14 dual polarisation measurements of true beam variation from Chokshi et al. (2021), and we produce simulations which use these measurements to modify the dipole gains within a tile on a floating-point level to match. While our simulations are still encoding discrete variation representative of 14 measurements, it adds to work that was previously binary in nature (Joseph et al., 2019). This gives a more realistic portrayal of expected errors from an instrument that has been in the field for over a decade. Given our evidence-based beam variations and our analysis framework, deformed beams may be the cause of current limiting systematics in recent MWA limits (Trott et al., 2020; Rahimi et al., 2021).

In Section 4.3, we describe how we build optimal beam maps via satellite measurements from Chokshi et al. (2021) for 14 tiles. In Section 4.4, we take these optimal maps and forward model them through a simulation and calibration framework which is representative of real data analysis. We summarise our power spectrum metric in Section 4.5 and investigate the effects of performing calibration with and without knowledge of the deformed beams in Section 4.6 and compare the results in power spectrum space. We summarise our conclusions in Section 4.7.

4.3. Optimal Satellite Beam Maps

The Fully Embedded Element (FEE) beam model (Sutinjo et al., 2015; Sokolowski et al., 2017) is a cutting-edge numerical electro-magentic simulation of the MWA tile response using FEKO[*]. The FEE beam model incorporates a number of significant improvements over the previous analytic representations of the beam, including mutual coupling between the multiple dipoles in the tile and a model of the electromagnetic effects of the soil below the tile.

The FEE simulations represent a tile under ideal conditions. Unfortunately, the arid conditions at the MWA site, and its remote location lead to a range of environmental factors which perturb beam models away from the FEE standard. In-situ, all-sky measurements of MWA beam shapes using communication and weather satellites have shown that the measured beam shapes differ from the FEE model, particularly away from zenith and within the sidelobes of the beams, at a ∼10% level (see, Line et al., 2018; Chokshi et al., 2021). The dual polarised beam shapes of 14 MWA tiles were measured by Chokshi et al. (2021), creating all-sky HEALPix (Gorski et al., 2005) maps with a angular resolution of 110 arcminutes at 137 MHz. These maps were created by an open-source `Python` package called `EMBERS` (Chokshi et al., 2020), and are available online. The direct incorporation of these measured beam maps into standard calibration software is hindered by their low resolution and narrow frequency bandwidth.

The FEE beam model has 16 variable dipole amplitude parameters per polarisation, which can each be tuned to weight the contribution of dipoles to the MWA tile. Typically, all dipole amplitudes are set to one, representing a perfect tile, with the occasional tile having a single dipole set to zero indicating the presence of a malfunctioning or flagged dipole (occurring in ∼20−40% of all tiles at any given time, see Joseph et al. 2019). This predominantly occurs due to the failure of the primary low noise amplifier (LNA) within the central column of the MWA dipoles as they gradually degrade upon contact with the slightly acidic local soil.

Our proposed method of incorporating more complex and perturbed beam models is to use the measured satellite beam maps to determine the optimal set of 16 dipole amplitudes, which best reproduce the measurements. This does not address the issue of extrapolating the narrow bandwidth satellite measurements at 137 MHz, as most Epoch of Reionization searches are conducted across the 167-198 MHz band where Galactic & extragalactic foregrounds and ionospheric effects are least dominant. Given the response of the MWA FEE beam, to first order, the scaling of these dipole amplitudes across frequency is considered to be linear. A study of the frequency scaling of these dipole parameters is beyond the scope of this work as it would likely involve drone measurements of the MWA beam patterns across the entire frequency band. In this work, we assume that it is valid to linearly extrapolate the dipole parameters recovered from 137 MHz satellite beam maps across the 167-198 MHz band where EoR observations are conducted.

[*] http://www.feko.info

The beam maps from Chokshi et al. (2021) are available* in the form of HEALPix maps of two types. The first represents a median satellite map, with pixel values averaged over all satellite passes, while the second are error maps with pixel values representing the median absolute deviation (MAD) of all satellite passes.

We define a likelihood function $\mathscr{L}$ which quantifies how similar the FEE model with 16 dipole amplitudes ($d_0 : d_{15}$) is to the measured beam maps. The set of dipole parameters which correspond to the maximum likelihood estimator $\mathscr{L}_{\max}$ leads an optimised FEE model.

$$\mathscr{L} = -1 \cdot \ln \left\{ \sum_{i=1}^{N} \frac{\left| \mathbb{S}_i - \mathbb{F}_i|_{d_0:d_{15}} \right|^2}{\mu_{\mathbb{S}\,i}} \right\}, \tag{4.1}$$

where $\mathbb{F}$ is the FEE beam model evaluated on a HEALPix grid, with a set of 16 dipole amplitudes, using the GPU accelerated `hyperbeam`† package. $\mathbb{S}$ is the satellite beam map with $\mu_{\mathbb{S}\,i}$ being the MAD error map and i the pixel indices. Pixels with FEE power lower than -30dB from zenith are masked out due to low signal to noise, along with the central 20° where bright satellites saturated the amplifiers used in Chokshi et al. (2021), leading to a low confidence central region.

We use the Bayesian Information Criteria (BIC) as the metric for our optimal model selection, as it accounts for the number of free parameters and amount of data used in the model evaluation, where BIC is defined as:

$$\mathrm{BIC} = k \cdot \ln(n) - 2 \cdot \mathscr{L}_{\max}, \tag{4.2}$$

where k is the number of free parameters in the model (16 in the case of the FEE beam model), n is the number of data points used (number of unmasked HEALPix pixels in satellite beam maps) and $\mathscr{L}_{\max}$ being the maximum likelihood estimator. The model with the lowest BIC value corresponds to a set of 16 dipole amplitude parameters which best optimise the FEE model to the given satellite beam map.

Figure 4.2 shows the best BIC values obtained via the maximum likelihood estimator of Eqn. 4.2 of an optimised FEE model (FEE Min - purple line), compared to the BIC value corresponding to a perfect FEE model (blue line), with all 16 dipole amplitudes set to 1. Figure 4.2 shows that the optimised FEE model is consistently preferred over the nominal FEE model, with improvements in BIC values of ~ 2 across the board. In Figure 4.3, the 16 optimal dipole amplitudes for MWA tile "S06" in the North-South polarisation (henceforth "S06YY"), recovered via the beam minimisation described above, are applied to the FEE model to quantify how well this process can reproduce measured MWA beam shapes. The top row (i, ii, iii) shows the perfect FEE beam model, the measured satellite beam model for tile "S06YY" and an optimised FEE model perturbed to best match the satellite map. Notice how the optimised FEE model (iii) has primary beam nulls which are less deep and distinct than the corresponding perfect FEE model, closely matching the satellite map (ii). The bottom row (iv, v) depicts residuals between the FEE or optimised FEE model and the satellite beam map respectively, with regions of the FEE model lower than 30dB below zenith power being masked out due to low signal to noise. The

*https://github.com/amanchokshi/MWA-Satellite-Beam-Maps

†https://github.com/MWATelescope/mwa_hyperbeam

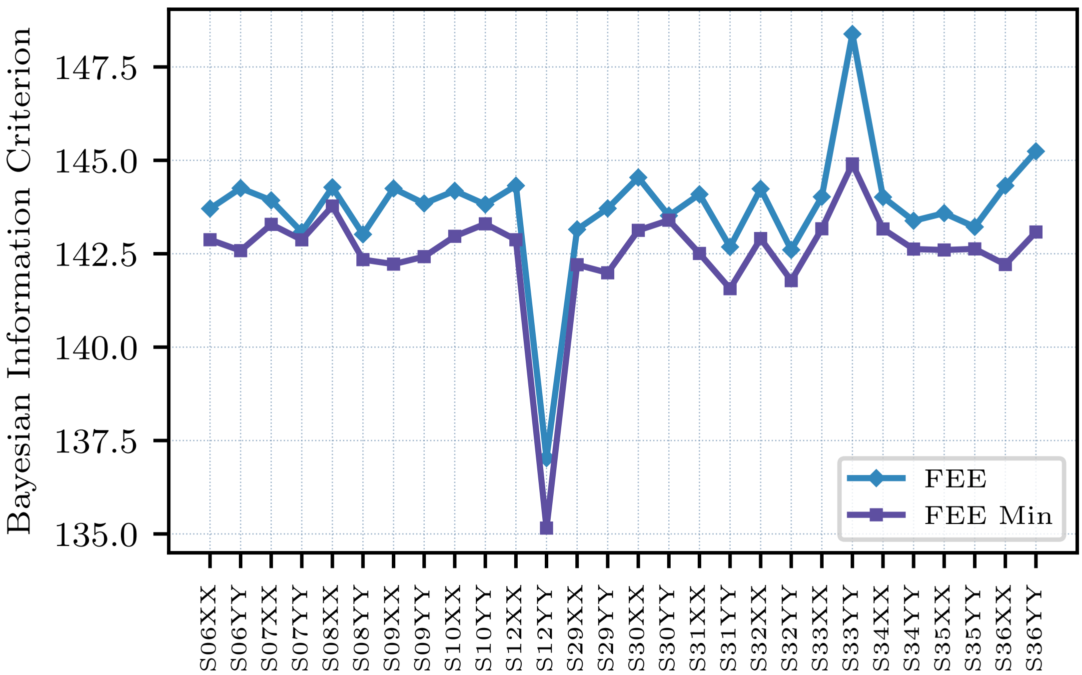

Figure 4.2: The best (lowest) BIC values obtained by the optimisation of the 16 dipole amplitude parameters in Eqn. 4.2, for the 14 dual polarised (XX, YY) MWA satellite beam maps available. The blue line (FEE), show the BIC value of the satellite map compared to the full FEE model, while the purple line (FEE Min) shows the BIC values for the optimised set of dipole amplitudes. Tile "S12YY" has lower BIC values due to sparse satellite coverage which led to a lower n in Eqn. 4.2.

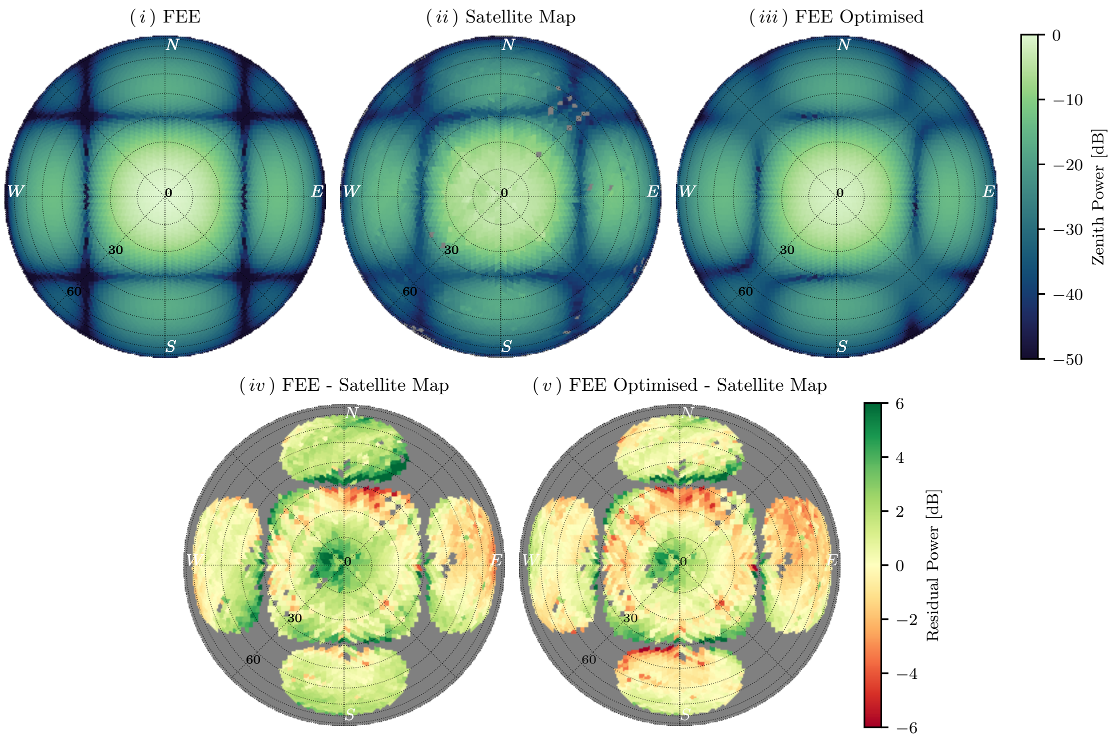

Figure 4.3: A study of the efficacy of the beam minimization procedure described in Section 4.3, tested on MWA tile "S06YY". The top row (*i, ii, iii*) represent the perfect FEE model, the measured satellite model, and the optimised FEE model using dipole amplitude parameters recovered by minimisation. The second row (*iv, v*) depicts the residual power between the FEE, optimised FEE models and the satellite beam map. Panels (*iii, v*) show that the optimised FEE model better matches the satellite beam maps (*ii*), accurately capturing first-order beam deformations present in the satellite data.

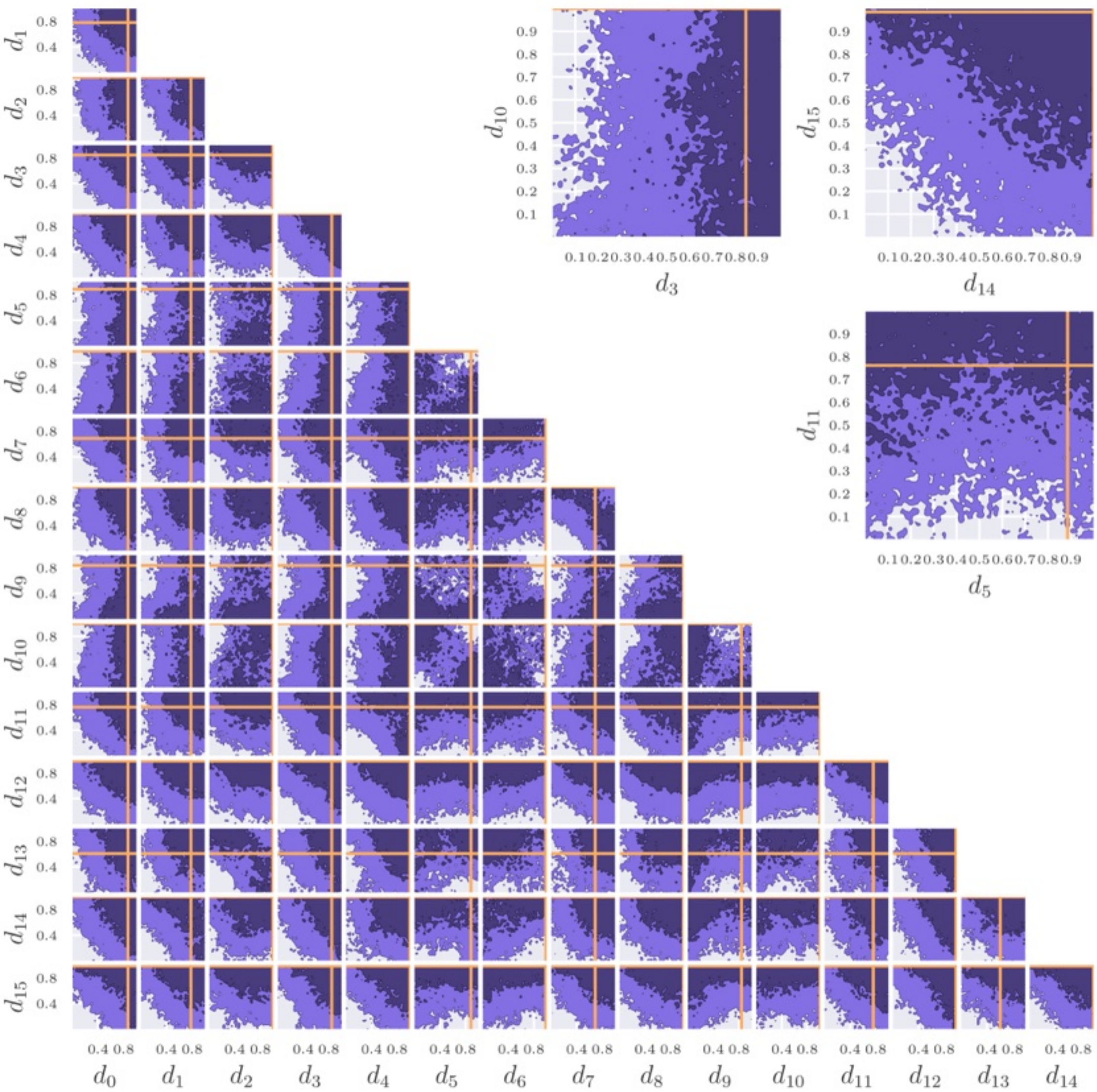

Figure 4.4: A MCMC analysis of MWA tile "S06YY" where purple contours represent 86% and 39% confidence levels respectively. The orange lines depict the results of beam minimisation from Section 4.3. The insets on the top right focus on three sets of dipole pairs which display varying levels of degeneracy between parameter constraints.

residuals with the optimised FEE model (v) have visibly reduced gradients across the beam sidelobes, and better match the satellite map at the zenith.

An in-depth investigation into the distribution of optimal parameters in the 16-dimensional dipole amplitude space was performed for MWA tile "S06YY", using a Markov chain Monte Carlo (MCMC) method, with the likelihood defined in Eqn. 4.1 and uniform, uninformative priors. The MCMC analysis was performed using a `Python` package called `EMCEE` (Foreman-Mackey et al., 2013), with corner plots made using `ChainConsumer` (Hinton, 2016). Figure 4.4 shows the result of the MCMC analysis, marginalised over pairs of parameters, with the purple contours representing 86% (dark purple) and 39% (light purple) confidence levels respectively. The orange lines represent the results of the beam minimisation described above, and shown in Fig. 4.3. While the results of the beam minimisation do concur with the central confidence contours in Fig. 4.4, large degeneracies are observed in certain pairs of parameters, representing a lack of tight constraints on some dipole amplitudes. The insets in the top right corner of Fig. 4.3 show that for dipoles d_3 & d_{10}, any possible value of d_{10} is as valid. Similarly, for the dipole pair d_5 & d_{11}, any value of d_{11} is equally valid. In essence, this indicates that dipole d_3 & d_5 place almost no constraints on dipoles d_{10} & d_{11}, respectively. In contrast, the dipoles d_{14} & d_{15} constrain each other well, leading to much lower degeneracy between these parameters.

We observe that the pairs of dipole parameters which are often least well constrained include one of the four central dipoles. The FEE beam is used in a "zenith normalised" form, where zenith power is scaled to 1, with everything else being correspondingly scaled. We posit that the observed degeneracy in dipole amplitudes which arises from the central dipoles can be explained by the fact that variation in the central dipole amplitudes tend to scale the overall power without significant deviations in beam shape. The effect is mostly eliminated by the zenith normalization of the beam. In contrast, the 12 dipoles on the edge of a MWA tile have a more significant effect on beam shapes, leading to significant distortions in the beam sidelobes. The χ^2 metric used in the beam minimisation and the MCMC analysis is only sensitive to global changes in the shape of the beam. The above procedure thus preferentially places most constraints on dipoles which affect the beam shape adversely.

4.4. Simulation & Calibration Framework

4.4.1. *Calibration & Beams*

Each unique pair of antennas in an interferometer, separated by baseline $\mathbf{u}$, samples the sky brightness distribution $I(\mathbf{l}, \nu)$ by measuring of the complex visibility

$$V(\mathbf{u}, \nu) = \int g_p g_q^* \, b_p(\mathbf{l}, \nu) b_q^*(\mathbf{l}, \nu) \, I(\mathbf{l}, \nu) \, e^{-2\pi i \mathbf{u}\cdot\mathbf{l}} \, d^2\mathbf{l}, \tag{4.3}$$

where $\mathbf{l}$ is the sky coordinate vector, ν is the observing frequency, g_p and b_p are the complex-valued gain and voltage beam pattern of antenna p, respectively. Calibration of measured visibilities enables the accurate reconstruction of the true sky brightness distribution $I(\mathbf{l}, \nu)$. Equation 4.3 demonstrates how each measured visibility $V(\mathbf{u}, \nu)$ contains the fundamental imprint of the constituent pair of receiving element beams.

Traditional sky-based calibration (e.g., Mitchell et al., 2008; Salvini & Wijnholds, 2014) minimises the squared differences between a measured visibility V_{pq}^{data} and a model visibility V_{pq}^{model} simulated from sky and beam models, to solve for unknown antenna complex-valued gains g_p and g_q

$$\chi^2 = \sum_{pq} |V_{pq}^{\text{data}} - g_p g_q^* V_{pq}^{\text{model}}|^2. \tag{4.4}$$

This work investigates the effects of an imperfect representation of the instrumental beams during this critical calibration stage.

4.4.2. *Fiducial Simulation*

To simulate a MWA array of 128 deformed tiles, 16 gain values are required per tile and polarization. Chokshi et al. (2021) measured all-sky dual-polarised beam maps of 14 fully polarized MWA tiles, and in Section 4.3 we determined the optimal gain parameters for each of their dipoles. For each dipole in a simulated deformed tile we make a random selection from the relevant 14 available gain parameters. This ensures that each of the 128 tiles has a physically motivated distortion model. This simulation framework can be used to emulate measurements made an interferometric array composed of deformed beams.

`hyperdrive`[*] (Jordan et al., in prep) is a cutting-edge sky-based calibration and simulation tool designed for the MWA, developed to be the successor to the Real Time System (RTS; Mitchell et al. 2008). `hyperdrive` is used to create a noiseless simulation of the 30,000 brightest foreground sources (see Figure 4.5) from the LoBES survey (Lynch et al., 2021), centered around the EoR0 field (R.A. 0^h, Dec $-27°$), with the set of 128 deformed MWA beams described above. This simulation is performed at a 80kHz frequency resolution, over the 167-198 MHz band, and represents a fiducial "measurement" made by a realistically deformed and complex array.

4.4.3. *Perfect & Imperfect Calibration*

The fiducial simulation created in Section 4.4.2 can be used to explore the effects of calibration errors introduced by the imperfect knowledge of beam models. We discriminate between two calibration scenarios below:

Perfect Calibration [$\mathbb{C}_P$]: In this case, a perfect understanding of our instrument is assumed, which is perfectly accounted for during calibration, along with a complete sky model. In particular, the set of deformed beam models used to generate the fiducial simulation in Section 4.4.2 are used to generate the model visibilities for calibration (V^{model} from Eqn. 4.4). This results in a perfect match between the fiducial simulation and the model visibilities used for calibration, leading to perfect calibration solutions.

Imperfect Calibration [$\mathbb{C}_I$]: In this case, an incomplete understanding of our instrument is emulated by using a single, perfect (FEE) beam model to generate the the model

[*] `https://github.com/MWATelescope/mwa_hyperdrive`

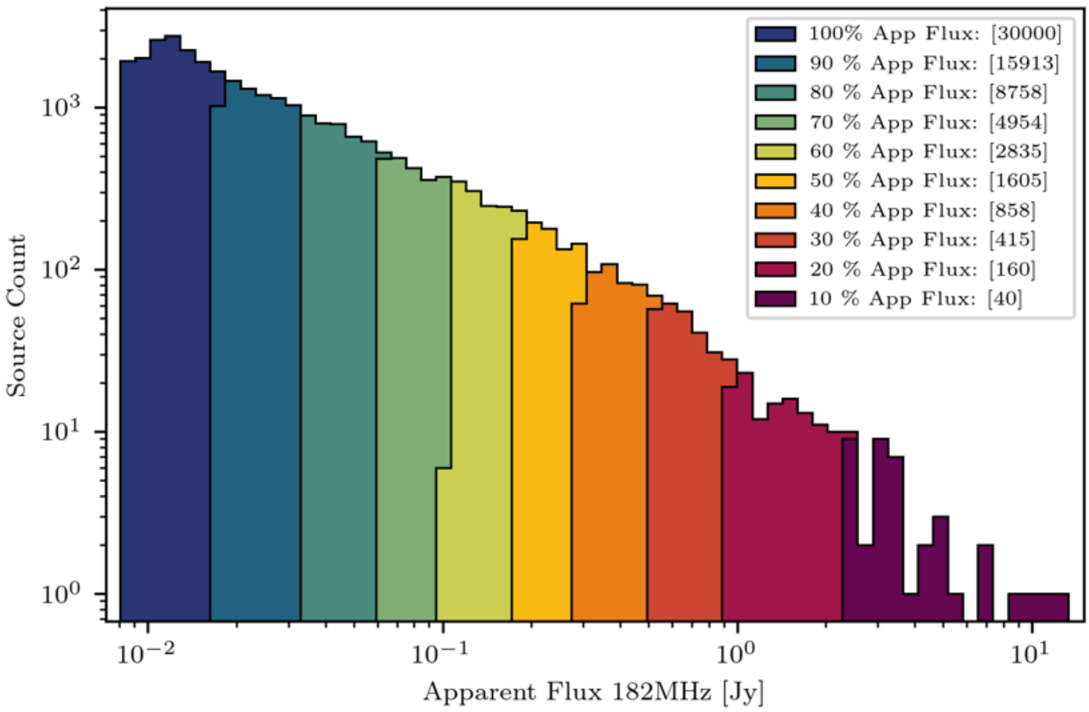

Figure 4.5: A histogram of apparent brightness of all 30,000 sources included in this work, at 182MHz. Each coloured section represent 10% of the integrated flux, from brightest on the right, to faintest on the left.

visibilities for calibration. This scenario was chosen to mimic current interferometric calibration pipelines where varied or deformed beams are not considered. This case also uses a complete sky model, ensuring that any calibration errors arise purely from beam errors.

Following the application of these two calibration scenarios to our fiducial simulated data, a 2D (cylindrical) and 1D (spherical) power spectrum analysis is performed to quantify the effects of mismatches in instrumental and calibration beams on an EoR detection pipeline, described below.

4.5. Power Spectrum

The spatial power spectrum is designed to quantify spatial correlations in a cosmological field, and measures signal power as a function of spatial scale, k ($h\mathrm{Mpc}^{-1}$). It can be defined as the Fourier transform of the two-point spatial correlation function:

$$P(|\vec{k}|) = \int_V \xi(\vec{r}) e^{-2\pi i \vec{k}\cdot\vec{r}} d\vec{r}, \tag{4.5}$$

where $\xi(\vec{r})$ is the two-point spatial correlation function. The power spectrum can be estimated from the volume normalised Fourier transformed brightness temperature field, given an observing volume Ω:

$$P(|\vec{k}|) \equiv \frac{1}{\Omega}\langle \tilde{T}(k)^{\dagger} \tilde{T}(k) \rangle. \tag{4.6}$$

It's relevant to note that in an interferometer, the observing volume Ω is determined by the primary beam of each receiving element or tile. Given the nature of the satellite beam measurements made in Chokshi et al. 2021, we only consider changes to the shape of beam responses across the array in this work, and make no assertions regarding changing observing volumes. This is in contrast to the case of flagged or dead dipoles, which change both the beam shape as well as observed cosmological volumes (see e.g. Joseph et al., 2018).

Radio interferometers fundamentally sample Fourier modes across the spatial (angular) extent of the sky, captured by the measured interferometric visibilities (see Eq. 4.3): $\mathbf{u} \equiv (u, v) \mapsto k_{\perp}$. For a resonant line signal, such as the 21-cm line, line-of-sight Fourier modes can be mapped with the spectral channels: $\mathcal{F}(f) = \eta \mapsto k_{\parallel}$. This mapping from measured interferometric visibility space (u, v, f) to Fourier space (u, v, η) leads to readily applicable expression for the power spectrum:

$$P(|\vec{k}|) \equiv \frac{1}{\Omega}\langle \tilde{V}(k)^{\dagger} \tilde{V}(k) \rangle. \tag{4.7}$$

In practice, multiple sets of measured visibilities are integrated coherently by gridding to a discretised uv-plane, following a Fourier transform along the spectral axis which results in an u, v, η data cube. This can now be squared to arrive at an unnormalised estimate of the cosmological power spectrum. Typically this orthogonal k-space is compressed to a 2D (cylindrically-averaged) and 1D (spherically-averaged) power spectra, where the former is used to isolate and diagnose foreground leakage and instrumental systematics, and the latter for cosmological measurements. The MWA EoR collaboration typically uses CHIPS - the Cosmological HI Power Spectrum estimator (Trott et al., 2016) and ϵppsilon - Error Propagated Power Spectrum with Interleaved Observed Noise (Barry et al., 2019a) for power spectrum estimation. In this work we use CHIPS to perform our power spectrum analysis.

4.5.1. Foreground Contamination and Subtraction

Galactic and extragalactic foregrounds dominate the faint cosmological EoR signal by up to five orders of magnitude (see Figure 4.1). To have any hope of detecting the EoR, extensive and accurate models of these foregrounds are necessary, including extended and bright sources such at Fornax A (Line et al., 2020), diffuse emission (Byrne et al., 2022), the Galactic plane (Barry et al., 2024), and the ubiquitous faint point-like extragalactic sources (Barry et al., 2016). A powerful discriminator between foreground flux and the background cosmological signal are their disparate spectral characteristics. The emission mechanisms of foreground sources are expected to be spectrally smooth (Di Matteo et al., 2002; Oh & Mack, 2003), while the 21-cm signal is anticipated to be uncorrelated on frequency scales larger than a MHz due to the topography of bubble formation and evolution as probed along the line-of-sight.

The cylindrically-averaged 2D power spectrum is formed by collapsing the cartesian 3D k-space along the spatial extent $k_\perp = \sqrt{k_x^2 + k_y^2}$, and the spectral or line-of-sight direction $k_{||}$. In this space, spectrally smooth foregrounds components will dominate the low line-of-sight modes ($k_{||}$) at all spatial modes perpendicular to the line-of-sight ($k_\perp$). We would thus expect a large region of this 2D k-space, above the low $k_{||}$ modes, to be free of power from the intrinsic foreground components. Unfortunately, radio interferometers are chromatic - they exhibit frequency dependant responses in both their primary beams and their synthesized beam or Point Spread Function (PSF). This results in the well-documented "foreground wedge" caused by the mode-mixing of power from low $k_{||}$ into larger $k_{||}$ values (Datta et al., 2010; Morales et al., 2012; Vedantham et al., 2012; Parsons et al., 2012; Trott et al., 2012; Hazelton et al., 2013; Thyagarajan et al., 2013; Pober et al., 2013; Liu et al., 2014a,b; Thyagarajan et al., 2015). This effect can also be considered to be the result of spectral structure being introduced to the otherwise spectrally smooth foregrounds by a chromatic instrumental response. The characteristic "wedge" shape of foreground mode-mixing arises from the fact that longer baselines (higher $k_\perp$) change more rapidly with frequency, resulting in faster spectral fluctuation which manifest as power at higher $k_{||}$ modes.

The area above the wedge is known as the "EoR window" and is expected to be contaminant free. The cosmological signal peaks at large scales, or small $k = \sqrt{k_\perp^2 + k_{||}^2}$, leading to an area of higher sensitivity in the lower left corner of the EoR window. This also means that k-modes within the wedge can have significantly more 21-cm power than those in the EoR window. The accurate subtraction of foreground flux from 21-cm data sets can enable the recovery of highly sensitive k-modes at the wedge-window boundary, boosting the significance of power spectrum measurements (Pober et al., 2014, 2016; Beardsley et al., 2016; Cook et al., 2022; Barry et al., 2024), and can theoretically put a statistical detection of the cosmological signal within reach of current generation experiments.

4.6. Results

Following the two calibration scenarios described in Section 4.4.3, a systematic subtraction of foreground flux is performed to enable the recovery of k-modes around the edge of the EoR window. Of the 30,000 sources included in the fiducial simulation from Section 4.4.2, we generate model visibilities (using the relevant set of calibration beam models) with integrated apparent flux in 10% intervals (see Figure 4.5), between the brightest 10% to brightest 90% to subtract from the two calibrated data sets. CHIPS is then used to calculate the 2D cylindrical-averaged power spectrum, and a 1D spherically-averaged power spectrum within the EoR window.

4.6.1. 2D Power Spectrum

The 2D or cylindrically-averaged power spectrum is the compressed parameter space where line-of-sight modes ($k_{||}$) and those in the orthogonal plane of the sky ($k_{\perp}$) are separated, making it an ideal space to observe and understand the complex effects of foreground-instrumental coupling (Pober et al., 2016). Figure 4.6 displays the 2D power spectra of the two calibration scenarios described in Section 4.4.3 before and after the majority of foreground flux has been subtracted. The dashed lines in Figure 4.6 represent the full-width half-max of the MWA primary beam response, while the black contours in the upper left corner of each panel represent the EoR window above the horizon.

The first two panels (i, ii) of Figure 4.6 contain flux from all 30,000 sources included in the simulation, with key differences occurring in the EoR window in the top left. The EoR window of the perfect calibration case ($\mathbb{C}_P$: panel (i)) has much less foreground power than the imperfect calibration case ($\mathbb{C}_I$: panel (ii)), by a factor of approximately 100. This excess foreground power present in the EoR window can be completely attributed to the mismatch between the set of measurement beam models (used to create the fiducial simulations in Section 4.4.2) and the single perfect beam model used during calibration.

We subsequently subtract a sky-model, generated with the relevant set of beams, containing 90% of the brightest apparent flux (see Figure 4.5) from each calibrated data set results. This results in an anticipated reduction of power within the foreground-wedge (lower sections of panels iii, iv), but unexpected behaviour within the EoR window. In the perfect calibration case ($\mathbb{C}_P - \mathbb{M}_{0.9}$: panel ($iii$)), the EoR window has significantly reduced power, while in the imperfect calibration case ($\mathbb{C}_I - \mathbb{M}_{0.9}$: panel ($iv$)), the EoR window power has remained essentially the same. The difference in EoR window power after foreground subtraction has now widened to be greater than a factor of 10,000, reaching levels significantly below the expected EoR in the perfect calibration case (panel (iv)).

This implies that spectral structure introduced into the calibration solutions by the mismatch between the set of instrumental and single calibration beam leads to mode mixing from low $k_{||}$ modes to high $k_{||}$ well beyond the expected foreground wedge. It also demonstrates that this excess beam-based chromaticity introduces power to the EoR window which cannot be mitigated by simply subtracting partial models of the foregrounds.

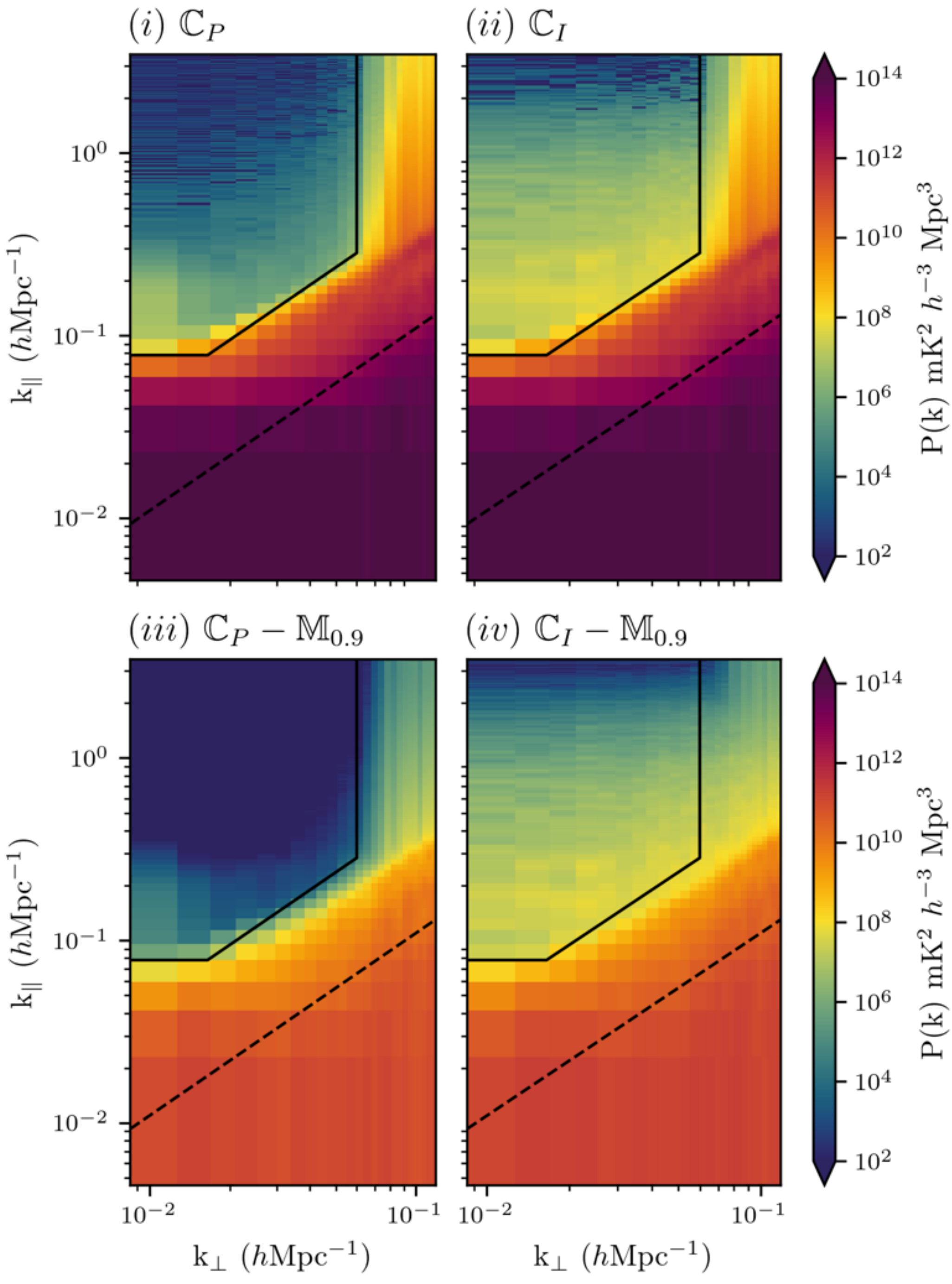

Figure 4.6: Cylindrical-averaged power spectra of the two calibration scenarios described in Section 4.4.3. The left column (panels *i*, *iii*) represents perfect calibration where the varied beam models are accounted for during calibration. The right column (panels *ii*, *iv*) represent imperfect calibration when a simple and incomplete instrumental model is used for calibration. The bottom row (panels *iii*, *iv*) are identical to the top row (panels *i*, *ii*) except that a 90% of the brightest foreground flux have been subtracted. The top left region of each panel is the EoR window where a search for the cosmological signal can be performed.

4.6.2. 1D Power Spectrum

Spherically averaging the k-modes within the EoR window leads to a 1D power spectrum typically assumed to be free of foreground power which can then be used to make cosmological measurements. In this work, we use the 1D power spectrum to quantify the extent of foreground spectral leakage into the EoR window caused by the differing instrumental and calibration beams.

In Figure 4.7 the grey dotted line and shaded regions denote the power level of an EoR model and its 95% confidence limits (Barry et al., 2019b; Greig et al., 2022) - which are used as a reference to compare levels of beam-based spectral leakage. Only when foreground leakage into the EoR window is below the EoR level and thus a sub-dominant systematic, is there any hope of a direct measurement of the cosmological signal. The different colours in Figure 4.7 denote varied levels of foreground subtraction from the brightest 10% in apparent flux to a complete 100% of all sources in 10% integrated flux bins (see Figure 4.5). The solid and dashed lines represent the perfect and imperfect calibration cases respectively.

In the imperfect calibration case (dashed lines in Figure 4.7) when an incomplete model of the telescope (i.e. a single beam model) is assumed during calibration, the resultant spectral structure introduced into the calibration solutions leads to foreground spectral leakage over a 1000 times our fiducial EoR model between k=0.1 and k=1 hMpc^{-1}. This foreground leakage into the EoR window is not appreciably reduced by subtracting models of foreground sources (dashed lines in Figure 4.7 lie practically on top of one another), demonstrating that the excess chromaticity introduced by beam-based calibration errors results in mode mixing beyond the well characterised foreground-wedge effect caused by instrumental chromaticity.

If an accurate instrumental model is used during calibration, as demonstrated by the perfect calibration scenario (solid lines in Figure 4.7), systematically subtracting models of the brightest apparent flux reduces spectral leakage into the EoR window till it is a sub-dominant effect. In fact, the solid navy blue line which represents a complete subtraction of foreground flux ($\mathbb{C}_P - \mathbb{M}_{1.0}$) during perfect calibration lies at the $\sim 10^{-20}$ mK^2 level far below the bottom of the y-axis in Figure. 4.7, and is numerically insignificant. This demonstrates that in the perfect calibration scenario, all foreground flux which is known can be subtracted from the EoR window, in contrast to the imperfect calibration scenario where a fundamental spectral leakage imprint remains in the EoR window despite the subtraction of sky-model flux.

A pertinent question to consider is why there is any power in the perfect calibration case prior to any flux subtraction ($\mathbb{C}_P$: black solid line in Figure 4.7), since all the foreground flux is expected to be contained in the foreground-wedge. We primarily attribute this to excess chromaticity from the implementation of the FEE beam model, but can also arise from the bandpass, decoherence due to frequency smearing, and other unidentified analysis or instrumental systematics. Any excess chromaticity leads to mode mixing of power from the foreground-wedge into the EoR window, which is then measured in the spherically-averaged power spectrum.

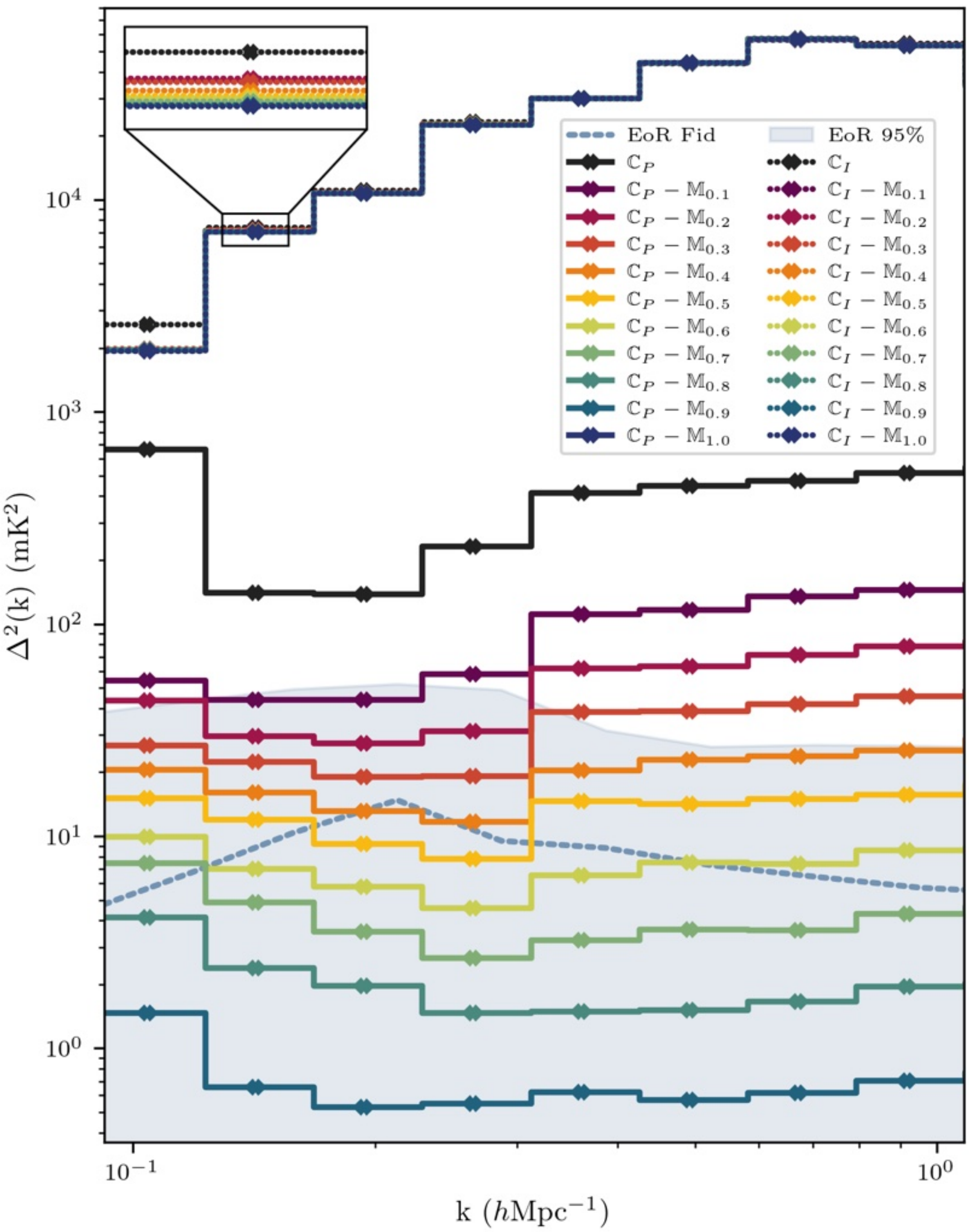

Figure 4.7: Spherically-averaged power spectra within the EoR window. The dashed lines represent the imperfect calibration ($\mathbb{C}_I$) scenario, while the solid lines represent the perfect calibration ($\mathbb{C}_P$) case. The coloured lines represent a systematic subtraction of apparent foreground flux, in intervals between 10% to 100% The grey dotted line is the fiducial EoR level while the shaded region represents the 95% confidence limits. Note that all the dashed lines from the imperfect calibration scenario lie practically on top of one another, and do not change significantly after subtracting foreground flux models.

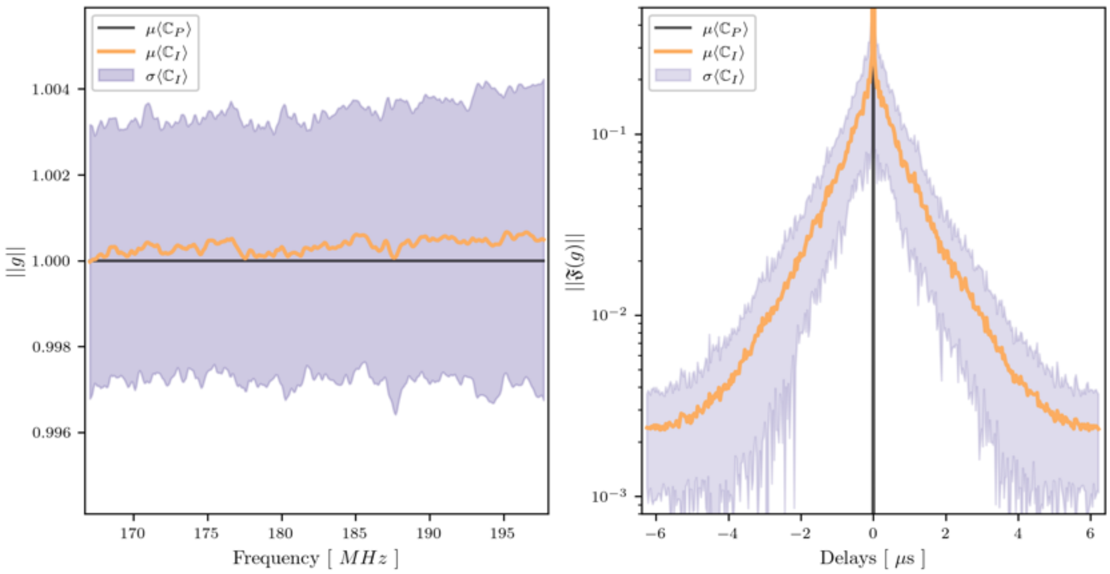

Figure 4.8: Gain amplitudes of calibration solutions are shown in the left panel, with the black line representing perfect calibration averaged over tiles ($\mu\langle\mathbb{C}_P\rangle$), while the yellow line is the antenna averaged gain amplitudes in the imperfect calibration scenario ($\mu\langle\mathbb{C}_I\rangle$) with the purple region enclosing 68% of values ($\sigma\langle\mathbb{C}_I\rangle$). The right panel is the Fourier transform along frequency of gain amplitudes, and plot the results as a function of delay. The black line is perfect calibration, while the yellow line represent the antenna averaged quantity and purple region encloses 68% of values from the imperfect calibration scenario.

4.6.3. *Spectral Structure in Calibration Solutions*

The 2D and 1D power spectra clearly demonstrate the effects of beam-based calibration errors, yet it is instructive to explore the raw calibration solutions obtained in Section 4.4.3, where beam-based spectral leakage initially originates.

The fiducial simulation from Section 4.4.2 was noiseless, and used a sky catalogue of 30,000 sources to generate visibilities which emulated a measurement by the MWA with a set of deformed beam models (V^{data}). While thermal noise can be a significant systematic in single observations, for a temporally stable instrument such as the MWA, noise in calibration solutions has been shown to incoherently average (Barry et al., 2019a). In the perfect calibration scenario, an identical set of deformed beams and sky catalogue are used to generate model visibilities (V^{model}) for the calibration minimisation process (see Equation 4.4). In the absence of noise, the fact that the data and model visibilities are identical leads to gain solutions which are unity within double precision across the frequency band (black line in the left panel of Figure 4.8). Adding thermal noise to the simulations would introduce uncertainty in the calibration solutions leading to a deviation for unity described above. This has the potential to introduce spectral leakage into the EoR window, even in simulations using a single perfect beam model. Further investigations along this line are left for future works.

In the imperfect calibration scenario, a single perfect beam model is used to generate the model visibilities (V^{model}) with the original sky catalogue. During the calibration process, the mismatch between the data and model visibilities lead to non-unity gain solutions as a function of frequency. This frequency structure is the root cause of foreground leakage from the EoR wedge into the EoR window observed in the power spectra, and can be solely attributed to an incomplete representation of the instrument (single beam model instead of set of deformed beam models) during the calibration process. The yellow solid line in the left panel of Figure 4.8 represent the antenna-averaged calibration gain amplitudes to visualise any common spectral structure, while the purple region encloses 68% of values.

To gauge the spectral structure within calibration solutions, we perform a Fourier transform across frequency, which decomposes calibration error amplitudes as a function of delay modes. In the perfect calibration scenario, this results in a delta function at a delay of zero, and any deviation from this would lead to excess calibration chromaticity, resulting in mode mixing from the foreground-wedge into the EoR window. The right panel of the Figure displays the Fourier transform of the calibration gain amplitudes, with the green line being the antenna-averaged quantity, while the blue region again encloses 68% of values.

4.7. Conclusions & Next Steps

This work explores the impact that imperfect and varied beams across a radio interferometer could have on EoR power spectrum measurements. We demonstrate how incomplete representations of varied and complex beams during calibration can lead to the leakage of foreground power into modes sensitive to the cosmological signal. This leads to contamination beyond the well-known foreground wedge into the EoR window, which is typically assumed to be free of foreground contaminants, at levels which exceed the expected EoR level by factors greater than ∼1000 between k=0.1-1 hMpc^{-1}. We also demonstrate how this effect is not improved by subtracting models and foreground sources, and necessitates the inclusion of validated and measured beam models in calibration frameworks.

Appreciable differences have been measured between cutting-edge electromagnetic Fully Embedded Element (FEE) MWA beam model (Sutinjo et al., 2015) and in-situ measurements using satellites (Line et al., 2018; Chokshi et al., 2021). These effects are predominantly measured as deformations in beam sidelobes, and are attributed to a variety of environmental factors. In Section 4.3, we develop a method of leveraging the 16 dipole gain parameters, natively used to weight the contribution of each dipole to the summed MWA tile response, to deform the FEE beam model to best match satellite beam maps from Chokshi et al. (2021).

In Section 4.4, we develop a physically motivated model to simulate a full 128-tile MWA array composed of realistically deformed beams based on the 14 dual polarization maps available from Chokshi et al. (2021). Using 30,000 complex sources from the LoBES catalog (Lynch et al., 2021), we create a noiseless fiducial simulation using the set of deformed beams, which emulates a real measurement with the MWA. We now calibrate our fiducial simulation using two strategies; perfect calibration where a complete understanding of the instrument is assumed by using the set of deformed beams during calibration, or imperfect calibration where a single FEE beam model is used to emulate currently accepted calibration strategies which do not account for beam variations across the radio interferometer. Using the spatial power spectrum described in Section 4.5, we investigate the effects of beam-induced calibration errors on the prospects of recovering an EoR signal in Section 4.6 (see Figures 4.6 & 4.7).

Our work demonstrates that **including physically motivated beam models during calibration has the potential to reduce foreground spectral leakage into the EoR window by factors greater that 1000, which could potentially put a statistical detection of the cosmological signal within grasp**. We outline the necessary step required to make this technique applicable to real data below:

- Satellite beam maps of each station in the radio interferometer will be a crucial first step. The satellite backend developed in Line et al. (2018); Chokshi et al. (2021) and the `EMBERS` analysis pipeline (Chokshi et al., 2020) have provided excellent all-sky maps at 137MHz at a very reasonable expense.

- A key question which has not been addressed by this work is the fact that the satellite maps by Chokshi et al. (2021) span a 1.4 MHz bandwidth, and are relatively narrowband in comparison to the observing bandwidth of ∼ 30 MHz. Thus the beam deformation model described in Section 4.3 is generated from narrowband data and applied across the broader observing band. The validity of this approach must be validated and augmented using a drone-based beam measurement system (Chang et al., 2015; Jacobs et al., 2017; Bolli et al., 2018; Ninni et al., 2020; Paonessa et al., 2020; Herman et al., 2024).

- The 16 parameter beam deformation model developed in this work was physically motivated by the aperture array design of MWA tiles, and could be modified to be applicable to telescopes such as LOFAR, NenuFAR, or the future SKA-Low. Unfortunately, telescopes such as HERA which employ parabolic dishes as their intereferometric elements will require new innovative models such as those developed by Wilensky et al. (2024).

We have demonstrated how a mismatch between the complex set of instrumental beams and the beam assumed during calibration can lead to the introduction of artificial spectral structure into calibration solutions which results in foreground leakages beyond the foreground wedge and into the EoR window. While we have shown that this beam-based calibration leakage can be mitigated by the inclusion of more accurate representations of instrumental beam models into calibration frameworks, it it not necessarily the only solution. While beyond the scope of this work, we leave the investigation of direction-dependant calibration, delay filtering, and regularised calibration solutions for future works.

CHAPTER 5

Effects of Deformed Interferometric Beams: Depolarization & Rotation Measure

This chapter is based on a draft of

A. Chokshi, N. Barry, B. Pindor, J. L. B. Line, C. J. Riseley, X. Zhang, R. L. Webster
to be submitted to the Publications of the Astronomical Society of Australia,

reformatted with the following changes only:

- **The text is styled and restructured to match the rest of this thesis.**
- **Where necessary, bibliographic records are updated.**

5.1. Abstract

The origins of cosmic magnetism can be unveiled by observing grids of polarised sources across large cosmological volumes, recently enabled by the adoption of wide-field interferometers. This work explores the impact which non-identical beam responses can have on instrumental depolarisation, which can result in biased populations within polarised surveys. All-sky satellite measurements of Murchison Widefield Array (MWA) beams have revealed significant sidelobe deviations from cutting-edge electromagnetic simulations at the ~10% zenith power level. This work builds an all-sky simulations framework of the MWA composed of physically motivated deformed beams, as a test-bed to explore the impacts of deformed beams on polarisation science. We observe $\sim 1\%$ fractional leakages at the beam centre rising to $\sim 5\%$ at the full width half maximum ($\sim 22°$ at 180MHz), which is similar to the baseline leakage observed in cutting-edge MWA beam models, but with significantly altered leakage morphology. The depolarisation observed with the set of deformed beams is $\geq 10\%$ worse than that observed with a single beam, and exhibits large gradients and non-uniform patches. We demonstrate how this altered leakage morphology is not improved by traditional direction independent calibration,

and outline avenues of investigations to improve the polarised behaviour of large imperfect interferometric arrays.

5.2. INTRODUCTION

Extended interferometric arrays have been adopted as the tool of choice for the efficient mapping of large cosmological volumes for multiple reasons. Constructed from hosts of identical and cheap dipoles, these aperture arrays can be coherently synthesised to achieve high angular resolutions over unprecedented large field-of-views. The search for distant and faint cosmic signals, coupled with the paradigm of simple software-driven telescopes, necessitates a precise and prior understanding of the instrument when pushing the upper bounds of sensitivity. A crucial part of the calibration process involves an understanding of the telescope's varied sensitivity across the sky, or its primary beam response. The construction of such arrays in remote and harsh radio-quiet sites can have a detrimental impact on the longevity of instruments, leading to an increased rate of dipole failure and other environmental perturbations to the beam models requiring more complicated calibration schemes to be considered in the pursuit of high fidelity science.

The Murchison Widefield Array (MWA[*]; Tingay et al., 2013; Wayth et al., 2018) is a low frequency radio interferometer, located in remote Western Australia at the Inyarrimanha Ilgari Bundara Murchison Radio-astronomy Observatory, and is a precursor to the Square Kilometer Array (SKA[†]). The MWA is an aperture array telescope, with 128 receiving tiles, each constructed from a grid of 4×4 dual polarization bow-tie dipoles. The MWA is a fully polarised instrument capable of imaging the sky in all Stokes parameters using orthogonal linear dipoles in the MWA tiles, aligned along the East-West and North-South directions respectively.

Large surveys of polarised radio sources and the exploration of cosmic magnetism are among the key science goals of low frequency radio telescopes such as the MWA (see, Wayth et al., 2015; Hurley-Walker et al., 2014, 2017; Riseley et al., 2018, 2020). Radio polarimetry at low frequencies is plagued by a host of challenges which include Faraday depolarisation (where polarised sources depolarise with increasing wavelength; Burn 1966), synthesised beam depolarization (here a mix of polarisation angles within the PSF can lead to an apparent reduction in observed polarisation fraction), and primary beam depolarisation (errors in beam models can lead to the loss of polarised signal). Significant flux leakage from Stokes I into other Stokes parameters have been observed in MWA polarimetric observations (see, Bernardi et al., 2013; Lenc et al., 2017, 2018). In zenith observations, leakage of $\sim 1\%$ at the beam centre and $\sim 4\%$ at the edge (full width half max $\sim 25°$ at 150MHz) of the primary beam have been measured, increasing to a range of 12-40% at off-zenith pointings.

The statistical detection of 21-cm Epoch of Reionisation (EoR) signal is another key priority of low-frequency arrays such as the MWA (Bowman et al., 2013; Beardsley et al., 2019b). Obscured by various foregrounds up to five orders of magnitude brighter than the redshifted cosmological signal (Oh & Mack, 2003; Santos et al., 2005; Pober et al.,

[*] http://www.mwatelescope.org
[†] https://www.skatelescope.org

2013; Yatawatta et al., 2013) a detection has yet to be made. Complex gain errors during calibration and primary beam model errors can lead to the leakage of polarised flux into the Stokes I maps hindering an EoR detection (Geil et al., 2011; Asad et al., 2015, 2016, 2018; Kohn et al., 2016, 2019). Faraday rotation measure techniques and direction dependant calibration can be used to decontaminate leakage from various polarised foregrounds (Geil et al., 2011; Asad et al., 2016).

Large computational simplifications in interferometric imaging are achieved by assuming that receiving elements across an array are identical. The reality of environmental interactions across large arrays leads to frequent failure of dipoles and more nuanced deformations in beam models, breaking the assumption of identical receiving elements. This is expected be be exacerbated and costly for extremely large arrays, such as the future SKA-Low telescope (Mellema et al., 2013; Koopmans et al., 2015). In-situ satellite measurements of MWA tiles revealed variations in sidelobe sensitivity at the $\sim 10\%$ level (Line et al., 2018; Chokshi et al., 2021). The impact of assuming a single beam model during calibration of measurements which encode non-identical beams has been investigated by Chokshi et al. 2024. They revealed leakage of non-polarised foregrounds into theoretically uncontaminated modes at levels over 1000 times brighter that the expected EoR, highlighting the importance of a precise understanding of instrumental complexities.

This work explores the importance of individually validated beam models across interferometric arrays for the accurate and unbiased recovery of polarised flux. It validates all-sky primary beam based polarisation leakage for the current cutting-edge MWA beam model, and compares them to the results simulated via an array of realistically deformed beam models. This work also highlights the importance of diverse beam sidelobes to polarisation science as we enter the SKA era.

A summary of the rotation measure synthesis technique is presented in Section 5.3, following which we develop a Jones matrix based framework of beam depolarization in Section 5.4. A simulation pipeline is developed in Section 5.5 to evaluate all-sky beam depolarisation induced by interferometric arrays composed of uniquely deformed beams. Results are presented in Section 5.6 with concluding statements in Section 5.7.

5.3. Rotation Measure Synthesis

Faraday Rotation Measure Synthesis is a novel technique developed and formulated by Burn (1966); Brentjens & de Bruyn (2005); Heald (2009). It leverages the Fourier relationship between observed complex narrowband linear polarisation and the function describing intrinsic polarisation, to disentangle multiple polarisation components along a line-of-sight.

Magnetised plasma in the intergalactic and interstellar medium acts as a birefringent medium, rotating the polarised plane of radiation as a function of frequency. This effect is known as Faraday rotation, and rotates the polarisation angle by:

$$\chi(\lambda) = \chi_0 + \mathrm{RM} \cdot \lambda^2, \tag{5.1}$$

where χ_0 is the intrinsic polarisation angle and $\chi(\lambda)$ is the polarization angle at wavelength λ. RM is the Faraday rotation measure, which characterises the amount of rotation and is given by:

$$\mathrm{RM} = 0.81 \int_{\ell}^{0} n_e \vec{B} \cdot \mathrm{d}\vec{\ell}, \tag{5.2}$$

where ℓ is the distance to the source in parsecs, n_e is the free electron density expressed in units of cm^{-3} and $\vec{B}$ is the magnetic field strength in μG. It is often useful to express these quantities in terms of measured Stokes parameters I, Q, U and V. Polarisation angle χ can be expressed as:

$$\chi = \frac{1}{2}\tan^{-1}\frac{U}{Q}, \tag{5.3}$$

with the complex narrowband linear polarisation P being expressed in terms of Stokes parameters and fractional polarisation (Π), as:

$$P = Q + iU = \Pi I e^{2i\chi}. \tag{5.4}$$

Traditionally, rotation measure was defined as the slope of the polarization angle χ versus λ^2:

$$\mathrm{RM} = \frac{\mathrm{d}\chi(\lambda^2)}{\mathrm{d}\lambda^2}.$$

This approach is good in theory, but is often limited in its application. The linear fit described above breaks down when there are multiple sources of polarised emission along the line of sight. Faint sources with high RM often have low signal to noise in individual channels. Integrating channels can lead to the decoherence of rapidly oscillating stokes Q and U fluxes resulting in a reduced perceived polarisation fraction, an effect dubbed bandwidth depolarisation. Further, there is an $n\pi$ radian ambiguity in the determination of polarisation angle which can lead to multiple degenerate RM fits (see Rand & Lyne, 1994). Rotation measure synthesis can be used to overcome these issues while also being capable of simultaneously disentangling multiple components of magnetic fields along the line of sight.

The elegance of the rotation measure (RM) synthesis technique comes from the ability to invert the complex polarisation vector via a Fourier transform. Equation. 5.4, denotes the observed complex polarisation vector, in which we can substitute χ from Equation. 5.1, replacing RM with a more generalised quantity known as Faraday depth, (ϕ). As all possible values of ϕ can contribute to the observed polarisation vector,

$$P(\lambda^2) = \int_{-\infty}^{+\infty} \Pi I e^{2i[\chi_0 + \phi\lambda^2]} \mathrm{d}\phi.$$

This can be re-written as:

$$P(\lambda^2) = \int_{-\infty}^{+\infty} F(\phi) e^{2i\phi} \mathrm{d}\phi,$$

where $F(\phi)$ is the Faraday dispersion function, describing the polarised flux as a function of Faraday depth. This equation is in the form of a Fourier transform and can be inverted to obtain the Faraday dispersion function $F(\phi)$ in terms of observable quantities:

$$F(\phi) = \int_{-\infty}^{+\infty} P(\lambda^2) e^{-2i\phi\lambda^2} \mathrm{d}\lambda^2. \tag{5.5}$$

While this is an elegant result, a few caveats must be noted. Having a negative value of λ^2 is non-physical, and in fact any real telescope will have a finite bandwidth and will not observe up to $\lambda^2 = \infty$. This problem is solved be introducing a quantity known as the rotation measure spread function (RMSF), which is convolved ($*$) with the true Faraday dispersion function to produce an observed Faraday dispersion function given by:

$$\tilde{F}(\phi) = F(\phi) * R(\phi).$$

This is analogous to the point spread function (PSF) of optical telescopes, which arise from the finite aperture of telescopes. In the case of the RMSF, the finite bandwidth of a radio telescope leads to the spread of the Faraday dispersion function (ϕ), from a compact delta function into a structure with sidelobes reminiscent of a sinc function. For a more rigorous introduction to RM synthesis, see Burn (1966); Brentjens & de Bruyn (2005); Heald (2009).

5.4. Beam Depolarization

Beam depolarisation is one of the effects that can arise from imperfect beam models. A polarised source which undergoes Faraday rotation via a magnetised plasma, is observed to have a sinusoidally oscillating flux in frequency, in both Q & U Stokes parameters. Typical synchrotron radio sources have Stokes I fluxes which follow power-law behaviour with the flux density $S \propto \nu^{\alpha}$, where the typical spectral index is $\alpha = -0.7$. Beam errors can lead to complex couplings between the Stokes parameters, leading to ripples in the I & V fluxes, while decreasing the amplitudes of Q & U fluxes, which is observed as a loss of polarisation. In this section we will build a mathematical framework to understand these effects, based on the Jones matrix formalism described by Hamaker et al. (1996).

We begin by defining a feed Jones matrix for antenna A:

$$\mathbf{J_A} = \begin{bmatrix} G_{Ax} & l_{Ax} \\ -l_{Ay} & G_{Ay} \end{bmatrix}, \tag{5.6}$$

with the diagonal terms G_{Ax}, G_{Ay} representing the complex gains and the off-diagonal terms l_{Ax}, l_{Ay} the leakage terms of the X & Y dipoles respectively. The gain terms account for sensitivity variations, while the leakage terms account for erroneous mixing of signals between the orthogonal X & Y dipoles. For a perfect feed, the complex gains are unity while the leakage terms are zero, reducing the feed Jones matrix to the Identity.

The complex vector amplitudes of a quasi-monochromatic signal propagating through space, evaluated at antenna A, can be represented as:

$$\mathbf{e_A} = \begin{bmatrix} e_{Ax} \\ e_{Ay} \end{bmatrix}.$$

.

The effect of a feed Jones matrix on incoming signals e_A^{in} can be represented as:

$$\mathbf{e}_{A,out} = \mathbf{J}_A \mathbf{e}_{A,in}$$

Consider two antennas A, B, with corresponding feed Jones matrices $\mathbf{J_A}, \mathbf{J_B}$. The visibility matrix for a baseline defined by antennas A and B is the cross-correlation or the outer product of electric field vectors $\mathbf{e_A}$ and $\mathbf{e_B}$ is given by:

$$\mathbf{e} = \mathbf{e}_A \otimes \mathbf{e}_B^* = \begin{bmatrix} e_{Ax}e_{Bx}^* \\ e_{Ax}e_{By}^* \\ e_{Ay}e_{Bx}^* \\ e_{Ay}e_{By}^* \end{bmatrix}.$$

The column vector above represents the complete set of polarised quantities measured by an interferometer such as the MWA, made in the instrumental frame of reference; i.e., aligned with the local EW, NS coordinate system on the ground. We can now observe the effect the two feed Jones matrices have on measurements:

$$\begin{aligned} \mathbf{e}_{out} &= \mathbf{e}_{A,out} \otimes \mathbf{e}_{B,out}^* = \mathbf{J}_A \mathbf{e}_{A,in} \otimes \mathbf{J}_B^* \mathbf{e}_{B,in}^* \\ &= (\mathbf{J}_A \otimes \mathbf{J}_B^*)(\mathbf{e}_{A,in} \otimes \mathbf{e}_{B,in}^*) = \mathbf{J}\, \mathbf{e}_{in}. \end{aligned} \tag{5.7}$$

These measurements are in a local instrumental Altitude and Zenith angle coordinate frame. Stokes parameters are basis dependant, and while valid in any orthogonal basis they are typically presented in a coordinate system aligned with Right Ascension and Declination. Due to the bow-tie nature of MWA dipoles, and projection effects, the local Altitude and Zenith angle coordinate frame is only orthogonal at the zenith. To calculate stokes parameters in any arbitrary direction, we can perform a rotation over parallactic angle to be aligned with the celestial Right Ascension and Declination frame. Measured instrumental visibilities, in the celestial frame, can be related to Stokes visibilities via a linear transformation given by:

$$\begin{bmatrix} XX \\ XY \\ YX \\ YY \end{bmatrix} = \begin{bmatrix} 1 & 1 & 0 & 0 \\ 0 & 0 & 1 & i \\ 0 & 0 & 1 & -i \\ 1 & -1 & 0 & 0 \end{bmatrix} \begin{bmatrix} I \\ Q \\ U \\ V \end{bmatrix} \tag{5.8}$$

Substituting Eqn. 5.8 in Eqn. 5.7, we obtain a set of equations which can be solved to express the observed Stokes parameters I', Q', U' & V' in terms of feed Jones matrices and real Stokes parameters I, Q, U & V. The relevant equations can be found in the Appendix A.

Figure 5.1 demonstrates the efficacy of the developed framework at reproducing beam depolarisation on a toy two element interferometer. We simulate a radio source with a reference Stokes I flux of 7 Jy at 200 MHz, with a spectral index of $\alpha = -0.7$. Stoke V fluxes of real radio sources are often observed to be atypical - in this work we assume a power law to demonstrate how the artificial coupling of I and V fluxes can occur via beam errors. The source has a simulated rotation measure of $+20$ rad/m^2 and a fractional polarisation of 30 %. The black lines in all panels of Fig. 5.1 depict the RM spectra, and the

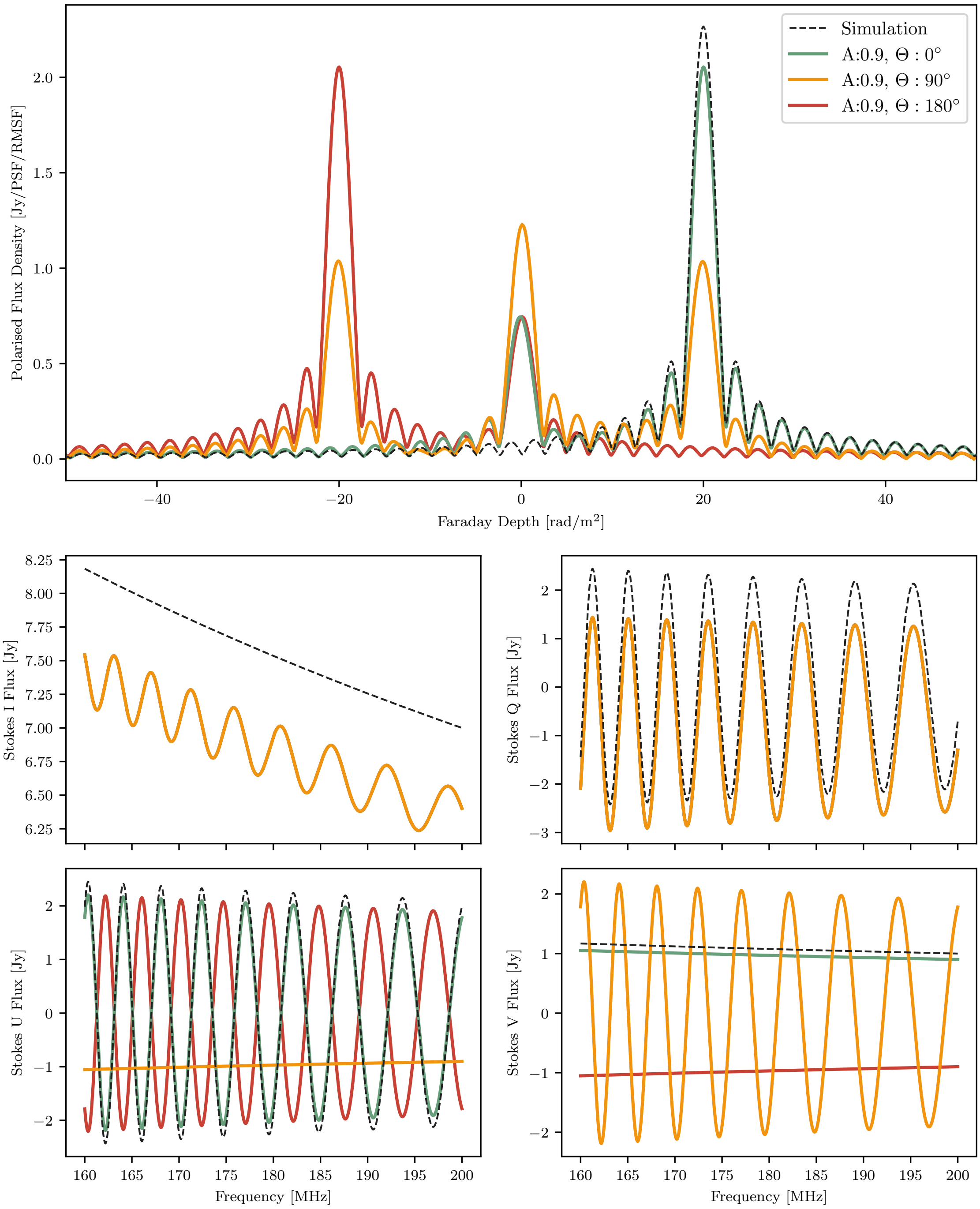

Figure 5.1: Theoretical models of beam depolarisation from a toy two element interferometer based on the Jones matrix formalism described in Section 5.4. The top panel shows the RM spectra of a simulated radio source of RM = +20 rad/m^2 (Black), with the coloured lines depicting various beam errors. In this model, the X dipole of both tiles are reduced to 90%, with the aqua, ochre, orange lines corresponding to phase errors of $\Theta = 0°, 90°, 180°$ respectively. The lower four panels show the effects of the above beam errors on the four Stokes parameters.

I, Q, U, V Stokes fluxes of the simulated source over a 160 to 200 MHz frequency range, where the MWA is most sensitive to large Faraday depths. The coloured lines show various effects that can be produced using the above Jones matrix formalism. Here, the amplitude of the X dipoles in both tiles A & B were reduced to 90%, in addition to a range of phase errors, indicated by Θ in the top panel of Fig. 5.1. The top panel shows that it is possible to almost completely depolarise the signal, or in extreme cases "mirror" the RM spectra peak, with a RM of -20 rad/m^2 measured instead of the true $+20$ rad/m^2. This would falsely be interpreted as a reversal in the direction of the line of sight magnetic field, purely due to beam errors. The bottom four panels of Fig. 5.1 represent the Stokes I, Q, U & V fluxes as a function of frequency. Note the various frequency-dependant effects that are introduces due to beam errors, manifested in the form of ripples or phase errors in the observed I', Q', U' & V' fluxes (see Appendix A).

5.5. Simulation Framework

The primary purpose of this work is to investigate the effects non-uniform and deformed beams across an interferometric array can have on Faraday Rotation Measure Synthesis and the apparent depolarisation of polarised sources via beam errors. Chokshi et al. (2021) measured significant sidelobe distortions in 14 MWA tiles at a 10% level. A framework to model and physically emulate the effect of deformed beams across a 128 tile MWA array was developed and tested in the context of Epoch of Reionisation science in Chokshi et al. (2024). Leveraging the 16 available dipole gain parameters in the MWA FEE beam model (Sokolowski et al., 2017; Sutinjo et al., 2015), Chokshi et al. (2024) used a Bayesian MCMC framework to optimally emulate beam deformations measured by Chokshi et al. (2021) by creating a dipole based weighting scheme. Drawing from this sample of optimal dipole gain parameters, 128 physically motivated deformed (DEF) MWA beams were generated to populate a realistically deformed MWA array. For a more in-depth review of this methodology refer to Chokshi et al. (2024).

`hyperdrive`[*] (Jordan et al., in prep) is a cutting-edge sky based calibration tool designed for the MWA, developed to be the successor to the RTS or the Real Time System (Mitchell et al., 2008). We perform `hyperdrive` simulation with either a perfect FEE beam model, or a unique set of deformed (DEF) beams described above. For each beam type (FEE or DEF), 40 simulations are performed using a calibration source list and a grid of polarised sources with one of 40 possible RM values to determine the all-sky effect of deformed beams on RM Synthesis and depolarisation.

The 20,000 brightest sources from the LoBES survey (Lynch et al., 2021), centered around the EoR0 field (R.A. $0h$, Dec $-27°$), represent the set of fiducial stokes I calibration sources. These are combined with a set of 6144 simulated polarised sources placed on a `HEALPix` (Gorski et al., 2005) grid with (`NSIDE`=32, spacing ~ 110 arcseconds) across the sky (see Figure 5.2). Each polarised source is identical to the one used in Section 5.4 (See black line in Fig. 5.1) – reference Stokes I flux of 7 Jy at 200 MHz, with a spectral index of $\alpha = -0.7$, and a fractional polarisation of 30 %. For each set of simulations, the RM value of all the polarised sources is selected from values spanning -70 to $+70$ rad/m^2 at intervals of 3.5 rad/m^2, with models of each distinct RM being shown in Figure 5.3.

[*] `https://github.com/MWATelescope/mwa_hyperdrive`

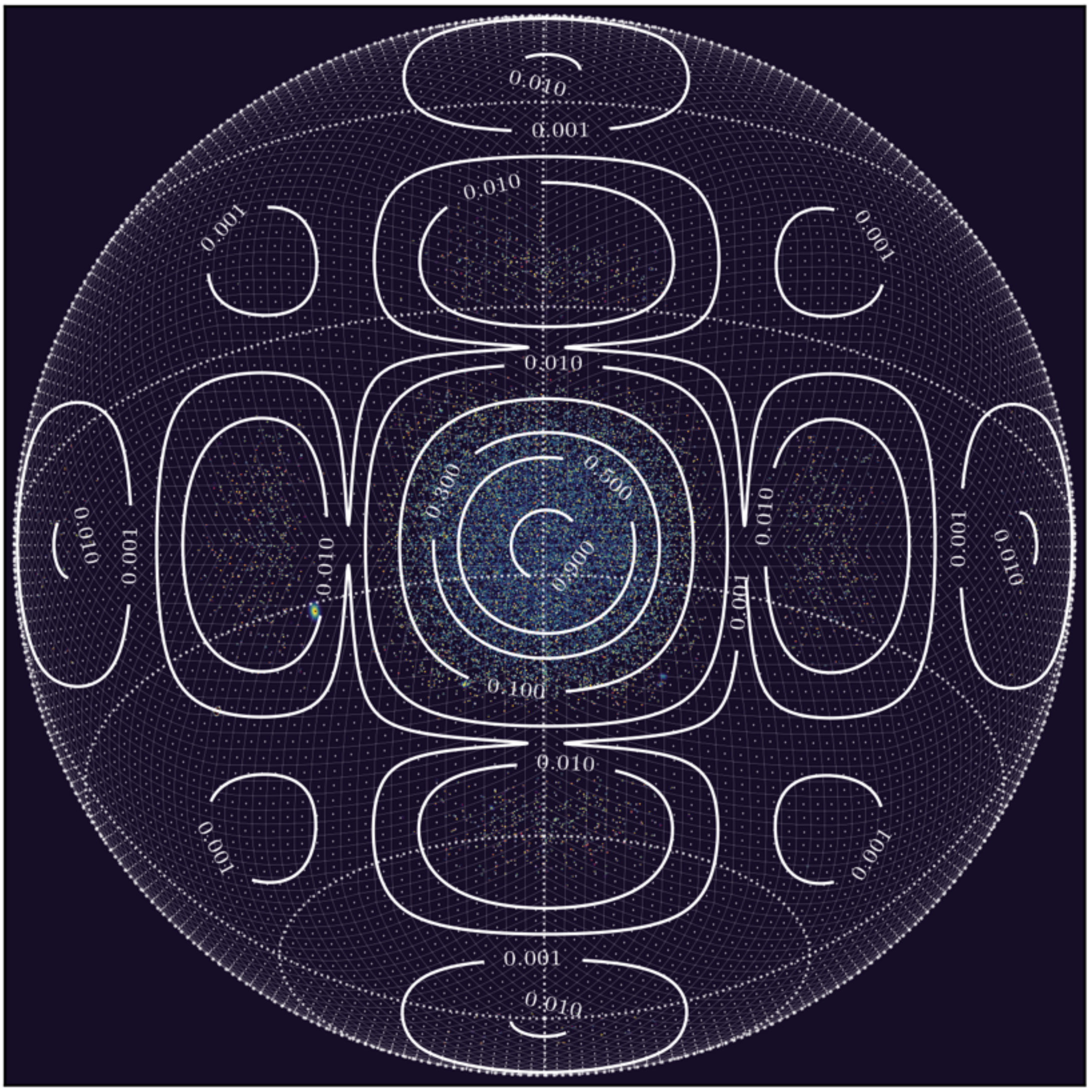

Figure 5.2: A simulated all-sky field-of-view with 20,000 calibration sources distributed across the sky, seen in the coloured background. Each HEALPix pixel with a white dot at its center represents the 6144 polarised sources. The white contours denote levels of zenith normalised MWA beam power.

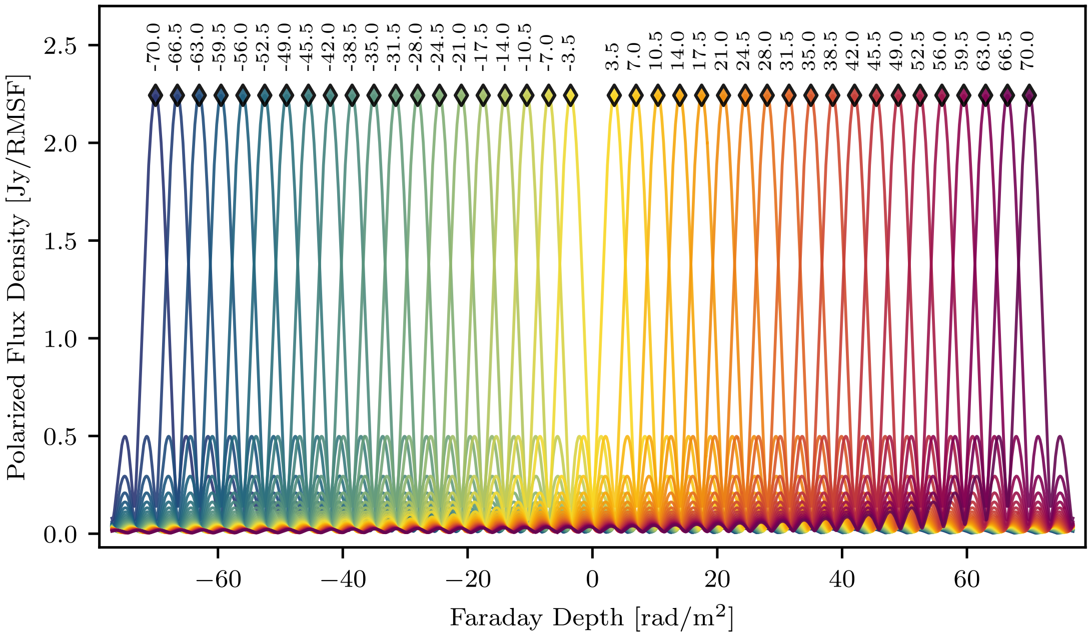

Figure 5.3: Models of the 40 possible RM values which each polarised source in Figure 5.2 can be. Each source displays significant sidelobe flux which is a result of the finite bandwidth and spectral resolution of the instrument, leading to input delta functions being convolved with the RMSF.

The simulations are performed at a 320kHz frequency resolution, over the 169-200kHz band optimised for RM sensitivity as well as computational feasibility.

These simulations contain a combination of flux from real stokes *I* calibration sources along with a grid of bright polarised sources. Any real observation of the sky would never contain this much polarised flux, yet the grid of polarised sources serves as a tool to probe all-sky polarisation leakage. The addition of a significant amount of artificial polarised flux has the scope to impact and bias any sky based calibration strategy. We mitigate any potential calibration bias introduced by the excess polarised flux by performing simulations using the FEE & DEF beams, with only the 20,000 stokes *I* calibration sources. These simulations can then be calibrated with the input simulation source list using either the FEE or DEF set of beams. The resulting spectral structure in the calibration solutions purely encode the effect of the varied simulation or calibration beams. These calibration solutions can be directly applied to the earlier simulations containing the polarised grid of sources, avoiding the issue of calibration biased excess polarised flux. The three calibration strategies explored are described below:

SIM:FEE|CAL:FEE – Each interferometric element in the simulation and calibration is identical to the FEE beam model. This case will reveal baseline beam depolarisation purely from the FEE beam model.

SIM:DEF|CAL:FEE – The simulation is performed with a set of deformed beams, while the calibration assumes a single FEE beam model. This case probes how an incomplete understanding of nuanced beam variations across the array can effect beam depolarisation after calibration.

SIM:DEF|CAL:DEF – Both the simulation and calibration stage encode the set of deformed beams, implying a perfect understanding of a complex interferometric array. This case will reveal baseline beam depolarisation due to a varied range of beam models across the array.

`WSClean` (Offringa et al., 2014; Offringa & Smirnov, 2017) is used to image the calibrated `Hyperdrive` data at the simulation 320kHz frequency resolution. Primary beam corrected dirty images of the entire sky in stokes Q and U channels were generated with `WSClean` using Briggs weighting (Briggs, 1995), with `robust` = -1.0 to minimize sidelobe confusion. Primary beam correction during the imaging stage is required to recover correct flux levels across the sky, and to ensure that the parallactic angle correction mentioned in Section 5.4 is applied, ensuring stokes parameters aligned with Right Ascension and Declination. `WSClean` currently only uses the FEE beam model during primary beam correction, which can result in errors when the simulations being imaged were created with a set of deformed beams. Developing imaging frameworks capable of utilising varied beam models is currently beyond the scope of this work, but is left for future work.

The rotation measure synthesis describes in Section 5.3 is performed with a GPU accelerated software package called `CuFFS`[*](Sridhar et al., 2018), resulting in 3D RM cubes with Faraday dispersion functions for line-of-sight across the entire sky.

5.6. RESULTS

Following the simulations described in Section 5.5, we measure the recovered polarised flux at the expected input RM depth and the leakage flux at the $\phi = 0$ mode to characterise a fractional beam leakage across the sky. Each set of simulations has a HEALPix grid of RM sources peaking at one of 40 possible values ranging from -70 to $+70$ rad/m^2, at intervals of 3.5 rad/m^2 (see Figure 5.3). RM spectra are extracted from each 3D RM cube at the input HEALPix grid centers, from which a fractional leakage $\mathbb{F}$ metric can be calculated for each pixel:

$$\mathbb{F} = \frac{1}{40} \sum_{RM:\langle -70:70 \rangle} \frac{\Delta\mathbb{L}_{RM=0}}{\mathbb{P}_{RM} + \Delta\mathbb{L}_{RM=0}}, \tag{5.9}$$

where $\Delta\mathbb{L}_{RM=0}$ is the flux at the $\phi = 0$ mode in excess of a model RMSF sidelobe seen in Figure 5.3, and $\mathbb{P}_{RM}$ is the peak flux at the expected input Faraday depth from the simulation. The 1/40 factor arises from averaging over the 40 simulations to arrive at a mean fractional leakage surface over a large range of RMs.

Figure 5.4 displays various components of polarisation leakage of simulations described in Section 5.5. The first column (panels *i, iv, vii*) of Figure 5.4 displays peak polarised flux $\mathbb{P}_{RM:\langle -70:70 \rangle}$ from various simulations. The second column (panels *ii, v, viii*) displays leakage flux $\Delta\mathbb{L}_{RM=0}$, while the final column (panels *iii, vi, ix*)shows fractional leakage $\mathbb{F}$ calculated from Equation 5.9. Areas of the sky where the beam sensitivity drops below 0.1% have been masked due to low sensitivity resulting in numerical noise dominated outputs. In the absence of any errors in the beam models, calibration

[*] https://github.com/sarrvesh/cuFFS

and in the stokes imaging phase, we would expect the peak polarised flux our simulations to be 2.243 Jy/RMSF across the sky, given the reference flux, spectral index and fractional polarisation of the simulations. We would also ideally expect no leakage flux, resulting in a zero fractional leakage across the sky. This project aims to quantify the effect of various instrumental beams and calibration on the level and morphology of the fractional leakage plane, across the sky.

The first row (panels *i, ii, iii*) of Figure 5.4 represent the results of a set of simulations performed with the perfect FEE beam model, and calibrated with the same beam model. Given that the calibration is performed with *all* the flux in the simulation, and that the simulations were noiseless, the calibration solutions were identically one. This set of results quantifies the extent and morphology of polarisation leakage in the best case scenario, where every interferometric element is identically perfect and also perfectly represented during calibration. We observe a $\sim 1\%$ leakage error at beam center, rising to $\sim 5\%$ at the full width half maximum (FWHM) of the primary beam ($\sim 22°$ at 180MHz). Leakage increases to between $\sim 5-30\%$ when extending outwards into regions of the primary beam sensitivity $\geq 10\%$. The leakage levels in the first sidelobes in regions with $\geq 1\%$ beam sensitivity range between $\sim 8-50\%$. Any area below a 1% beam sensitivity is considered effectively depolarised with leakages exceeding $\geq 50\%$.

The second row (panels *iv, v, vi*) of Figure 5.4 represent the results of a set of simulations performed with the set of deformed (DEF) beam models described in Section 5.5, and calibrated with the same set of beam models. Due to identical sets of beams being utilised in both simulation and calibration, calibration solutions are identically one. Similar to the case above, this set of results quantifies the extent and morphology of polarisation leakage, in the presence of a set of perfectly characterised but unique deformed beams across an array. While the level of polarisation leakage is not drastically different to the case in the first row, the morphology of the leakage surface is significantly altered. This is most apparent by looking at the third row (panels *vii, viii, ix*) of Figure 5.4, which represent the difference between the first and second rows. In the residual leakage plot (panel *ix*), it is clear that the two cases can differ by $\pm 3\%$ in the primary lobe. It is interesting to note that depolarisation in the simulation with the deformed beams are consistently worse by beyond $\geq 10\%$ in first sidelobes. This intuitively makes sense since the central lobe of the primary beam is extremely well constrained, while environmental factors have been shown to preferentially effect beam sidelobes (see Line et al., 2018; Chokshi et al., 2021), to varied extents and in non symmetric manners.

The results investigated in Figure 5.4 characterise polarisation leakage of either the single FEE beam, or a set of uniquely deformed (DEF) beams. It does not touch upon the effect of calibrating data with beams different than those which produced the simulations. Satellite measurements of MWA beams have revealed sidelobe variation from the FEE beam model at the $\sim 10\%$ level (Chokshi et al., 2021). Any observation made by an interferometric array inherently encoded *all* primary beams of the array. This implies that observations by the MWA must contain imprints of the range of deformed beams which constitute the array. All current MWA calibration strategies assume a single identical beam model across the array which can lead to the introduction of spurious spectral structure into calibrated data. Chokshi et al. (2024) demonstrated how such a simplistic representation of the instrument during calibration can negatively effect the prospect of an Epoch of Reionisation detection. We now aim to gauge the effects of calibrating data which encodes a set of deformed (DEF) beams with a single FEE beam model. Simulations created with the set of deformed (DEF) beams are calibrated with either the same set of deformed beams, or a single perfect FEE beam model. Fraction leakages surfaces are calculated for both using Equation 5.9, as in Figure 5.4, and the difference between the two scenarios is displayed in Figure 5.5. We observe noise-like residuals in fractional leakage between the two scenarios, yet no significant spatial structure across the sky. Least variations are observed in closer to the beam center, increasing in regions of lower beam sensitivity. Figure 5.6 show a histogram of the residual fractional leakage which shows a distinctly peaked symmetric structure centred about zero. The histogram is well described by a Laplacian distribution with mean $\mu = 0$ and scale parameter $b = 0.0027$. This implies that calibrating data which inherently encoded a range of deformed beams, with a single perfect beam model, can result in a noise-like change in the fraction leakage plane at a $\pm 0.3\%$ level. We do not observe any significant variation of the morphology of the leakage plane, which appears to be dictated by the various deformed beam models across the array.

5.7. CONCLUSION

This work explores the impact that imperfect and varied beams across a radio interferometer could have on low frequency polarisation science. We demonstrate how deformed beams across interferometric arrays can introduce complex variations to the extent and morphology of depolarisation across the sky.

In-situ satellite measurements of all-sky MWA beams (Line et al., 2018; Chokshi et al., 2021) have shown significant sidelobe distortions at the $\sim 10\%$ level. Chokshi et al., 2024a developed a Bayesian MCMC framework to utilise satellite measurements to optimally emulate measured beam deformations in the cutting-edge MWA FEE beam model (Sutinjo et al., 2015; Sokolowski et al., 2017). This enables the creation of physically motivated simulated MWA arrays with realistically deformed beam models. Adopting this methodology, this work develops a Jones matrix based mathematical framework to explore depolarisation arising from varied beams across an interferometer in Section 5.4. In Section 5.5 we outline our simulation methodology, which includes using subset of the 20,000 brightest sources from the LoBES (Lynch et al., 2021) catalog in addition to a array of 6144 synthetic polarised sources arraying in a HEALPix grid to simulate all-sky depolarisation effects.

Within the FWHM of the MWA beam ($\sim 22°$ at 180 MHz), the level of depolarisation caused by a set of deformed beams is similar to the inherent depolarisation with the cutting-edge FEE beam model at $\sim 1\%$ at beam center and rising to $\sim 5\%$ at the FWHM, but demonstrating a different morphology. Beyond the FWHM, significant quantitative and structural changes are observed in the depolarisation plane. Within regions of the sidelobe with sensitivity $\geq 1\%$, simulations with deformed beams demonstrate $\geq 10\%$ increases in fractional depolarisation compared to the perfect FEE beam, observed in non-uniform patches and gradients. Our simulations also indicate that in areas of the beam with sensitivity $\leq 1\%$, irrespective of beam type, polarised signal are effectively depolarised with fractional depolarisation exceeding $\geq 50\%$.

Any observation by an inteferometer inherently encodes imprints of *all* primary beams across the array. Give the $\sim 10\%$ sidelobe distortions in MWA beams measured by Chok-

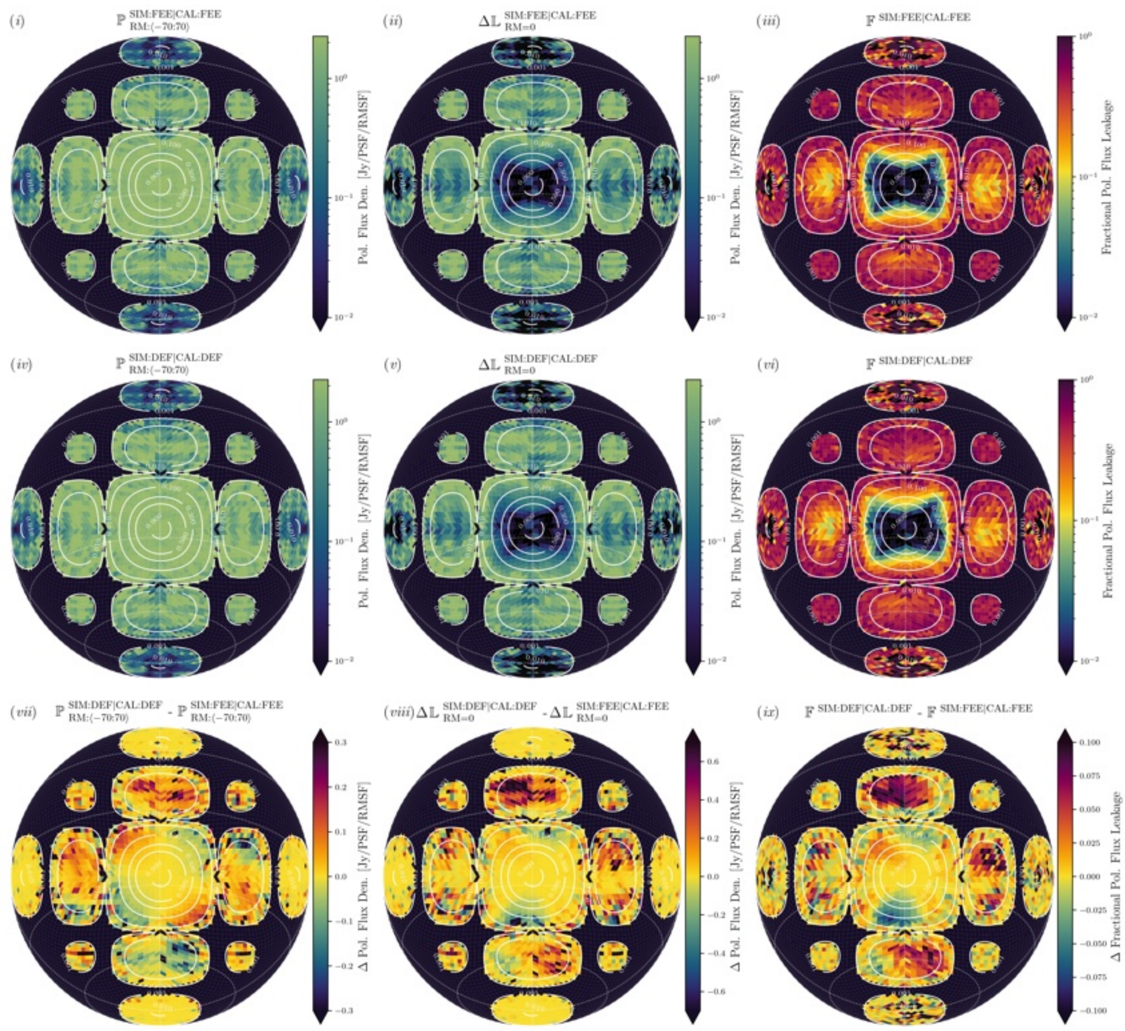

Figure 5.4: All sky maps of various components of polarisation leakage simulations described in Section 5.5. The top row (panels *i, ii, iii*) represents simulations of a HEALPix grid of polarised & calibration sources with a single perfect FEE beam, and calibrated with the same beam model. The second row (panels *iv, v, vi*) are simulations using a set of 128 unique deformed (DEF) beams, and calibrated with the same set of deformed beam models. The final row (panels *vii, viii, ix*) represents the residuals between the two corresponding panels above. The left column (panels *i, iv, vii*) represents polarised flux $\mathbb{P}_{RM:\langle -70:70 \rangle}$ at the expected RM value, averaged over the set of 40 simulations. The central column (panels *ii, v, viii*) represents leakage flux $\Delta\mathbb{L}_{RM=0}$ at the $\phi = 0$ Faraday depth, in excess of modeled RMSF sidelobes. The final column (panels *iii, vi, ix*) represent the fractional polarisation leakage $\mathbb{F}$ given by Equation 5.9, calculated from the two corresponding panels to the left. Areas of the sky where the beam sensitivity drops below 0.1% have been masked due to low sensitivity resulting in numerical noise dominated outputs and are shown in black. The white contours in each panel represent levels of zenith normalised MWA beam power.

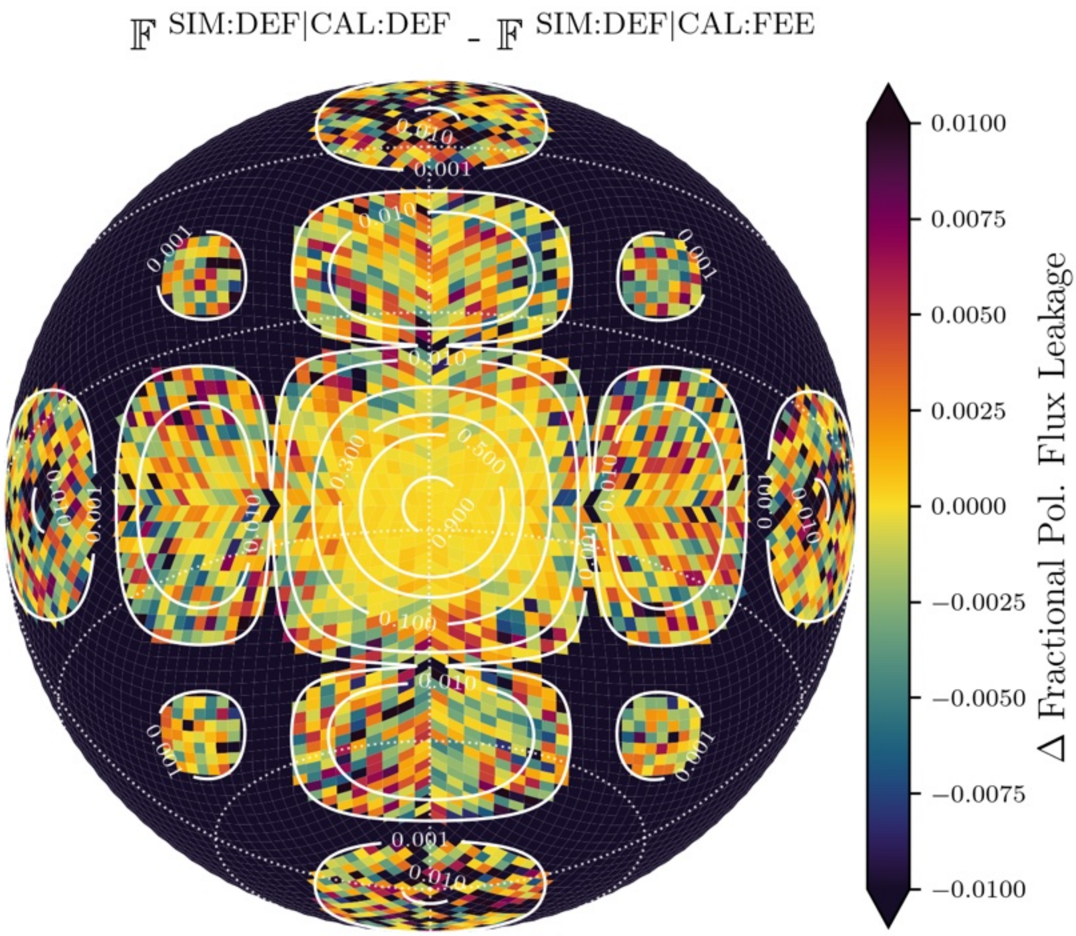

Figure 5.5: The difference between fractional polarisation leakage surfaces for two calibration scenarios. Simulations of a HEALPix grid of polarised sources a performed using a set of uniquely deformed (DEF) beams. The simulations are calibrated using either the input set of DEF beams, or a single perfect FEE beam model. Fraction polarisation leakage is calculated using Equation 5.9, and the difference between the two scenarios is plotted.

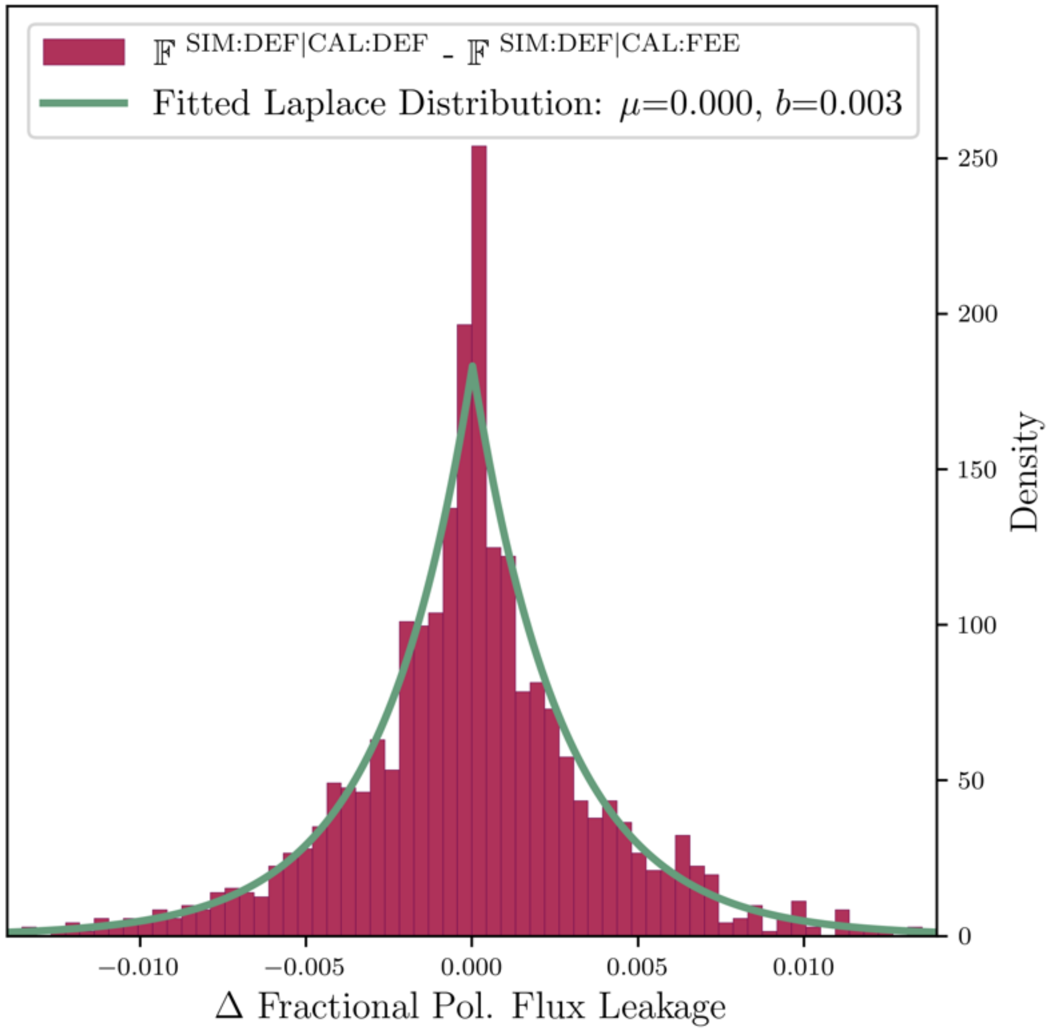

Figure 5.6: A histogram of the noise-like residuals between a set of simulations performed with a set of deformed (DEF) beams, calibrated with either the input set of DEF beams, or a single perfect FEE beam model (Figure 5.5). The histogram is well described by a Laplacian distribution with mean $\mu = 0$, and scale parameter b = 0.003.

shi et al. (2021), all MWA data must encode characteristics of varied beams. To recover true and unbiased sky intensities, calibration processes much account for nuanced instrumental systematics. Unfortunately *all* current MWA calibration strategies only use a single beam model which is assumed to perfectly represent every interferometric element across the array. Chokshi et al. (2024) demonstrated that this mismatch between imperfect instrumental beams, and single assumed calibration beams can lead to spurious calibration artefacts dominating an Epoch of Reionisation power spectrum detection by factors exceeding 1000. In contrast, we find that in the context of polarisation leakage, calibrating with a single beam introduces noise to the all-sky fractional depolarisation as seen in Figures 5.5 & 5.6, but does not appreciable change the extent or morphology of the depolarisation structure introduced by a set of deformed beams. This lack of change in fractional leakage morphology after calibration could potentially arise from the fact that during the imaging stage of the simulation pipeline, `WSClean` performs the crucial primary beam correction using a single perfect FEE beam model. This could lead to calibration effects being sub-dominant, only resulting in the excess noise observed in Figures 5.5 and 5.6.

For widefield instruments with relatively simple primary beam patterns such as the MWA, this work suggest that beam depolarisation resulting from a set of deformed beams is not an insurmountable factor within the FWHM of the primary lobe. Asymmetric variations in the fractional leakage surface show in Figure 5.4 have the potential to introduce biases to populations of observed polarised sources, where dimmer polarised sources could be sufficiently depolarised to disappear within the noise floor. More advanced survey and mosaicing strategies utilising overlapping FWHM sized patches could potentially mitigate or reduce this bias. Quantifying this bias and exploring mitigation strategies are left for future works.

As the astronomical community prepares for the commissioning of the SKA-Low observatory, we must be aware and prepared for increased instrumental complexities. With 256 dipole per station, the potential for station beams to deviate from ideal models, due to environmental factors is significantly exacerbated in comparison to a simple 16 dipole MWA tile. With the plan for multiple pseudo-random dipole layouts for SKA-Low stations, and with each being uniquely susceptible to environmental beam deformations, we expect extremely complex sidelobe structure. This will inevitably lead to high levels of sidelobe depolarisation. With the SKA-Low's narrower $4 \times 4°$ primary FoV, sensitive surveys of cosmic magnetism will be extremely slow and susceptible to population biased due to the expected complex depolarisation morphology. Simulation of the SKA-Low beam deformations are beyond the scope of this work.

We have demonstrated that deformed beams across interferometric arrays can lead to complex and unexpected depolarisation morphology across the sky. We note that direction dependant polarised calibration strategies could be particularly effective in the context of deformed interferometric beams - investigations along this line are left for future work.

Computer spinning,
The segfault tells me nothing,
Goddam GPU.

Jack Line, 2024, *Haiku*

CHAPTER 6

Conclusions & Discussions

The Epoch of Reionisation represents one of the last frontiers of modern cosmology. A crucial transformatory period in our Universe's history, the EoR spans the birth of the first luminous sources via the gravitational coalescence of primordial over-densities. Bubbles of ionising radiation expanded into the Universe, centred around these first luminous objects, heralding a phase transition of matter from neutral to the completely ionised state we observe today. This epoch also encompassed the formation of the morphologically complex and structured galaxies we observe around us today. Observing the EoR promises to aid in the unravelling of mysteries surrounding the birth of the first stars and galaxies, their nature, and their influence on the evolution of the Universe. Prior to the completion of reionisation, the spin-flip 21-cm line of neutral Hydrogen acts as a powerful tool to probe the early Universe. Tracing the morphology of reionisation, it can be leveraged to observe large cosmological volumes (see Figure 1.2). Unfortunately, a range of astrophysical and terrestrial foregrounds obscure signals from the EoR by factors exceeding $\sim 100,000$ (see Figure 1.5). Chapter 1 outlines the history of the Universe, highlights the importance of the EoR and explores challenges to its detection. Low-frequency radio interferometers are powerful modern telescopes designed to achieve unprecedented angular resolution over wide fields-of-view. In Chapter 2 we develop the mathematical tools required to understand interferometry, and discuss its applicability to EoR searches; both in the context of a statistical detection, and for future tomographic imaging efforts.

The journey to a first validated detection of the EoR signal will necessitate a precise understanding of our telescopes. The dominant obscuring foreground flux couples with complex instrumental characteristics in a non-trivial manner. Precisely understanding this coupling will be required to disentangle foreground flux from the cosmological signal five orders-of-magnitude fainter. Current measured upper-limits of the EoR 21-cm power spectrum are still a couple of orders-of-magnitude higher than EoR models.

The focus of this thesis was to explore the possibility of interferometric primary beam models contributing to analysis sytematics, and whether understanding them could improve the prospects of a future EoR detection (see Appendix B for a discussion of often overlooked nuances of primary beam models). The assumption of identical beam models across interferometric arrays is ubiquitous as it enables massive computational simplifications via the convolution theorem. Is this a valid assumption, and if not, at what level are we introducing beam-based analysis systematics into our science? As a first step, we developed and deployed an experiment to measure the all-sky dual-polarised primary beam patterns of 14 MWA beams using communication satellites. This work was described in Chapter 3, and revealed unexpected and significant sidelobe variation at the $\sim 10\%$ level, along with sub-degree rotations in the tiles. These inter-tile variations were primarily attributed to environmental factors; erosion of the soil under the reflective ground screens leading to their deformation, local foliage growth and infrequent animal interactions.

Our measurements showed that interferometric beams deviate from cutting-edge electromagnetic models at a significant level. An obvious next step was to explore the level at which deformed beams across interferometric arrays effect various science cases. In Chapter 4, we develop a physically motivated model of beam deformation capable of emulating beam measurements performed in Chapter 3. Using this framework, we explored the impact of deformed beams on a potential EoR power spectrum detection. We showed that assuming a single perfect beam model during calibration of data which encoded a set of deformed beams introduced foreground spectral leakage greater than the expected EoR level by factors exceeding ~ 1000 between $k = 0.1 - 1\,h\mathrm{Mpc}^{-1}$. This spectral leakage was not appreciably reduced by the subtraction of large fractions of sky-flux models. On the other hand, including knowledge of deformed beams into calibration frameworks reduced this foreground spectral leakage to a sub-dominant effect. This could potentially put an EoR detection within grasp if we can measure instrumental beams across an entire interferometric array and include them into calibration frameworks.

Low-frequency interferometric arrays are fully polarised instruments, making measurements in all Stokes $\{I, Q, U, V\}$ parameters. In Chapter 5, we explore the impact of deformed beams on polarisation science. The ISM and IGM plasma acts as a birefringent medium, rotating the plane of polarisation of radiation in the presence of magnetic fields. Fourier Rotation Measure (RM) synthesis is a novel technique which enables the recovery of multiple magnetic fields along lines-of-sight to polarised sources, providing a powerful probe of cosmic magnetism. Errors in the primary beam model can unfortunately introduce an effect known as “beam leakage”, where polarised signals appear depolarised. In this work, we demonstrate that the presence of deformed beams across interferometric arrays can lead to a change of this beam leakage morphology, particularly significant in beam sidelobes where leakage can be exacerbated by factors $\geq 10\%$. This has the potential to completely depolarise faint polarised sources, as well as bias the population of polarised surveys. This could be of particular import for the future SKA-Low observatory whose sidelobes are expected to be notoriously hard to characterise.

In the rest of this conclusion, we discuss an exploratory investigation as a motivation for future studies, followed by a outline of future investigations of interest.

6.1. At what level do deformed beams matter?

In Chapter 4, we demonstrated the impact that deformed beams can have on a power spectrum EoR detection. Not including knowledge of deformed beams during calibration resulted in spectral leakage of foreground power into cosmologically sensitive modes,

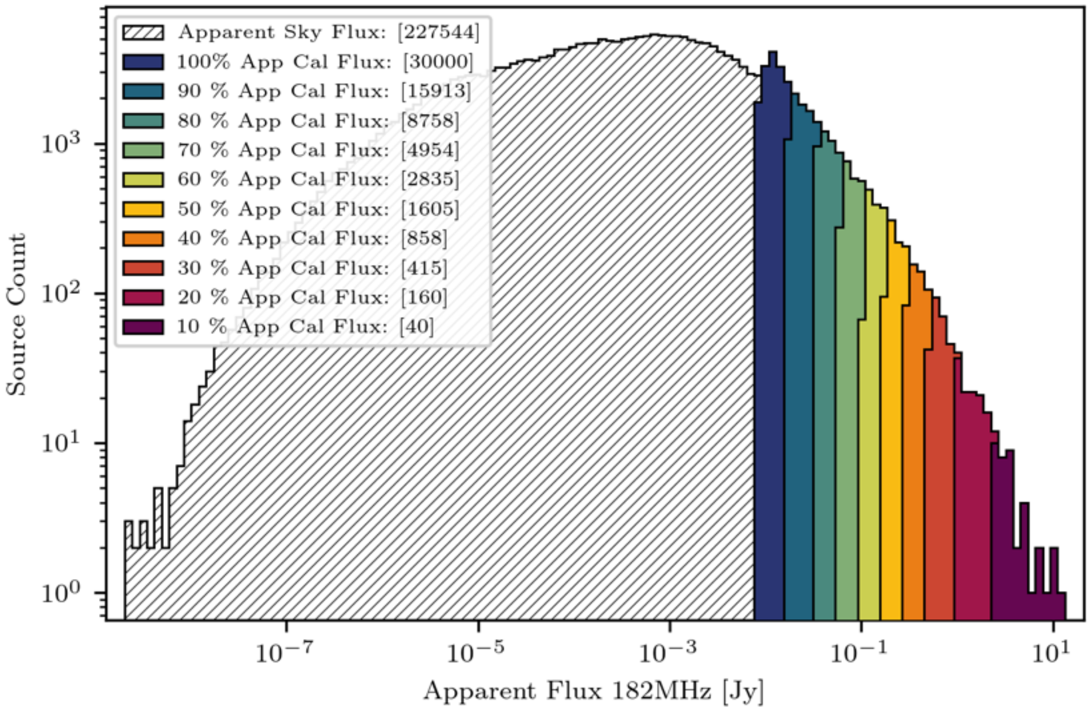

Figure 6.1: A histogram of all almost 300,000 beam-weighted foreground sources in the LoBES catelogue, with the brightest 30,000 used in Chapter 4, Figure 4.5 highlighted to the right.

at levels exceeding ~ 1000 times greater then the expected EoR level. While the work in Chapter 4 demonstrated the critical need to include validated beams during calibration, it only represents a first step into such investigations due to a set of simplifying assumptions:

- The simulations were performed with the set of 30,000 brightest LoBES sources shown in Figure 4.5. Figure 6.1 shows that the selected sources represent a biased sample from the ~300,000 available LoBES sources, which have a significant number of fainter sources.
- Calibration was performed using *all* the flux in simulations (all 30,000 sources), which clearly isolated the effects of deformed beams during calibration.
- The study was noiseless. There is no evidence that instrumental noise introduces spectral structure into calibration solutions, and thus an analysis using noise was omitted.

In reality, it is impossible to include *all* foreground flux during calibration. The hope is that by including large fractions of foreground flux during calibration, we can accurately characterise the instrumental transfer function, and undo it to reveal the true sky. To explore this we perform a set of `WODEN`* simulations, mirroring those in Chapter 4, using all

*https://github.com/JLBLine/WODEN

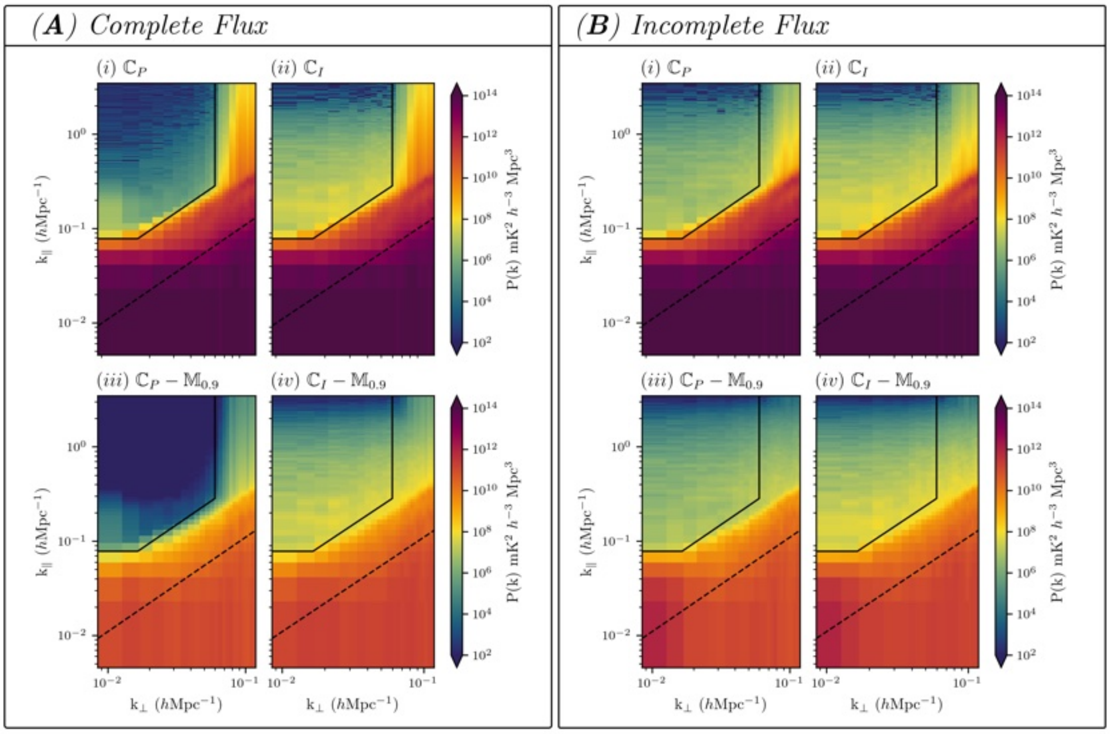

Figure 6.2: Panel (**A**) represents an investigation into beam models when all sky flux is included during calibration, mirroring the results of Chapter 4. Panel (**B**) repeats the previous exercise, with all 300,000 LoBES sources included in the sky simulation, while only the brightest 30,000 were included during calibration.

300,000 LoBES foreground sources, with and without the deformed beams. Calibration is performed using `hyperdrive` and only the brightest 30,000 LoBES sources. Results are depicted in Figure 6.2, with panel (**A**) reproducing the case from Chapter 4 where all sky flux in included in calibration, and panel (**B**) showing when only the brightest 30,000 sources are used during calibration of a simulation containing all 300,000 LoBES sources (see Figure 6.1). The striking difference is that when only a fraction of the sky flux is used during calibration, substantially higher leakage occurs from the foreground wedge to the EoR window. In this case, the calibration process is imperfect for two reasons; both the partial flux model used during calibration and the deformed beams leads to calibration errors.

This simple test shows that foreground-flux-based errors occur at a higher level than beam based errors. Like Figure 1.5, where a variety of celestial and terrestrial foregrounds obscure the EoR, there may be layers of calibration and instrumental errors which become apparent as higher-order effects are addressed. Once sky-flux-based calibration errors are solved, deformed-beam-based errors will become a dominating contaminant, and need to be solved before an EoR detection can be made.

6.2. Future directions

In the following section I outline ideas which will extend the work presented in this thesis.

6.2.1. *Calibrating real data with measured MWA beam models*

In Chapter 4, we demonstrated that including measured models of MWA beams into calibration frameworks has the potential to improve foreground spectral leakage into the EoR window by factors greater than ~ 1000 using simulations. The obvious pressing question is how we apply this to data, and whether the results will be as significant as the simulations predicted. Below are steps which could make this a reality.

All-sky satellite beam measurements across the MWA

We currently only possess measurements of 14 MWA beam models, measured in 2020 by Chokshi et al. (2021). At minimum we require measurements of the 128 compact Phase II MWA tiles (sensitive to the EoR), and hopefully all 256 Phase III tiles. Scaling the original satellite beam measurement (Chokshi et al., 2021) experiment from 14 to 256 will not be feasible without at minimum a redesign of the hardware used.

It is impractical to have a pair of RF Explorer Spectrum Analysers[*] per polarised MWA tile, with many Raspberry Pis[†] running the capture software. One path forward would be to engineer a set of receiver boards which could channelise raw MWA tile power, all of which could be controlled by a single board computer installed into MWA receiver boxes. This system is non-ideal since it is extremely invasive to the telescope, requiring the installation of new hardware into the signal chain of each MWA tile. Any failure in this hardware could lead to the degradation or the complete loss of MWA data.

An alternate avenue would be to emulate a passive observing strategy developed by Sokolowski et al. (2024), leveraging the new MWAX correlator (Morrison et al., 2023). By re-channelising current MWA observations using the commensal MWAX observation mode, we may be able to capture raw voltages from tiles to generate satellite beam models of *all* tiles, without the necessity of signal-chain interruptions. The drawback of this method is that we could only observe at the frequencies of the original MWA observation schedule, which would reduce the time spent in the 138 MHz band where bright communication satellites are active. This would result in a reduced beam mapping efficiency.

Hybrid drone-satellite framework

The nature of satellite beam mapping experiments is that they are inherently narrowband, in comparison to the MWA's 30.72 MHz instantaneous bandwidth. The beam deformation model developed in Chapter 4 assumed that the 16 beam deformation parameters did not change with frequency. Using a test MWA tile, it may be possible to investigate the chromatic scaling of these deformation parameters across the MWA

[*] http://rfexplorer.com

[†] https://www.raspberrypi.org

band, using a drone mounted broadband transmitter. If a empirical scaling relation can be developed, it could be applied to measured narrow-band satellite maps.

Temporal evolution of beam deformation

Finally, the beam deformations measured in Chapter 4 were primarily attributed to environmental factors — erosion of soil below the ground screen, foliage growth around and in the tile, and interaction with animals on site. These are not static, and could potentially change slowly between observing seasons. Long term beam monitoring experiments will be needed to understand the temporal variation and scale of beam deformation. It may be challenging or impossible to apply current measured deformed beams to archival data. In the worst case scenario, we may need to re-observe EoR data and calibrate it with a set of matched beam measurements.

6.2.2. A rising Galactic plane and deformed beams

The MWA beam is sensitive to the entire visible sky (horizon-to-horizon) as seen in Figure 2.5. Measurements of MWA beams have revealed that the largest variations from cutting-edge beam models occur away from the zenith, and are worst along the horizon. The MWA EoR observing fields are chosen to be centred around the quietest patches of the sky with least foreground emission. Unfortunately, even with this careful selection of observing fields, the Galactic plane is unavoidably rising on the horizon (see Figure 2.5). Barry et al. (2024) demonstrated that the presence of the Galactic plane on the horizon could introduce foreground contamination at a level ~ 20 times higher than the EoR power, when the MWA beams were identically perfect.

It would be pertinent to explore how the extremely bright Galactic plane on the horizon couples with a simulated MWA array composed of a set of deformed beams (like those developed in Chapter 4). We could also explore calibration strategies which could mitigate these effects.

6.2.3. Dead dipoles and the SKA-Low

In its Phase I or II configuration, the MWA is composed of 2048 (128 tiles $\times$ 16 dipoles per tile) identical dual-polarisation dipoles. Dipoles occasionally experience failures in their LNAs, or in the connections to the analogue beamformer. These are primarily due to environmental factors such a the slightly acidic soil at the MRO degrading the LNAs and lightning strikes. Figure 6.3 shows the percentage of MWA tiles with either one or two flagged dipoles, between 2013 and 2019. At any time between $\sim 15-35\%$ of MWA tiles have at least one non-functional dipole. Joseph et al. (2019) demonstrated that the unaccounted presence of these non-functional dipoles resulted in calibration-based power spectrum errors at the $\sim 10^3 \mathrm{mk}^2 \mathrm{h}^{-3} \mathrm{Mpc}^3$ level.

The current design of the SKA-Low telescope has a total of 131,072 dipoles (512 stations $\times$ 256 dipoles per station). This represents a staggering increase in the number of dipoles, and a proportional increase in their potential for failure. It would be interesting to quantify the effect of various levels of dipole failure on the SKA-Low's potential for making an EoR detection. This is likely to be a real problem that the SKA-Low observatory will struggle with — the sheer human resources required to keep it in perfect operating condition could be infeasible.

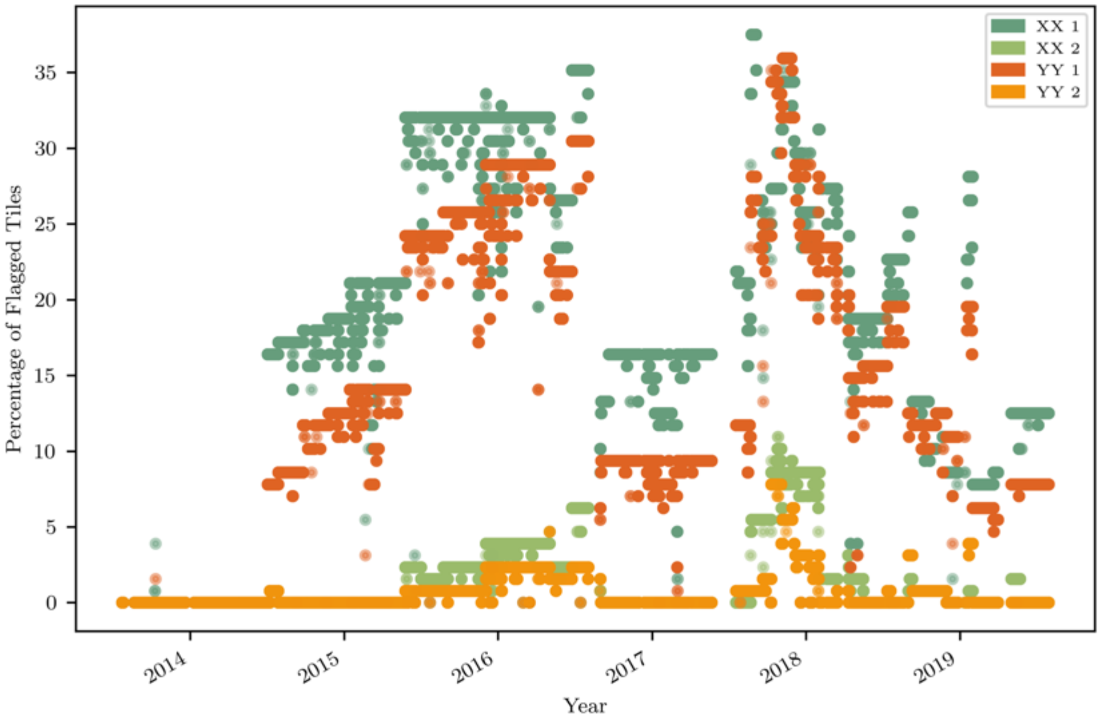

Figure 6.3: The percentage of MWA tiles with either one or two dead dipoles, for each polarisation, between 2013 and 2019. The dark green and dark orange are the percentage of tiles with one XX (East-West) and YY (North-South) dipole flagged respectively. The lighter green and orange represent the fraction of tiles with two dipoles flagged.

6.3. Final Thoughts

The field of 21-cm cosmology is poised to be revolutionised with the arrival of the SKA-Low observatory, which promises to deliver tomographic images of the Epoch of Reionisation. The first stations are currently being constructed at *Inyarrimanha Ilgari Bundara*, our Murchison Radio-astronomy Observatory, with an expected completion within the next 5 years. It is my hope that some of the lessons learnt over the course of this thesis, particularly regarding the complexity of modeling beams, will be valuable in enabling the best science with next-generation telescopes.

APPENDIX A

Beam Depolarisation & Stokes Parameters

This sections build upon the mathematical theory presented in Section 5.4. We pick up by substituting Eqn. 5.8 in Eqn. 5.7, and writing the full form of $\mathrm{J} = \mathrm{J_A} \otimes \mathrm{J_B}^*$:

$$\begin{bmatrix} 1 & 1 & 0 & 0 \\ 0 & 0 & 1 & i \\ 0 & 0 & 1 & -i \\ 1 & -1 & 0 & 0 \end{bmatrix} \begin{bmatrix} I' \\ Q' \\ U' \\ V' \end{bmatrix} = \begin{bmatrix} G_{Ax}G^*_{Bx} & G_{Ax}l^*_{Bx} & l_{Ax}G^*_{Bx} & l_{Ax}l^*_{Bx} \\ -G_{Ax}l^*_{By} & G_{Ax}G^*_{By} & -l_{Ax}l^*_{By} & l_{Ax}G^*_{By} \\ -l_{Ay}G^*_{Bx} & -l_{Ay}l^*_{Bx} & G_{Ay}G^*_{Bx} & G_{Ay}l^*_{Bx} \\ l_{Ay}l^*_{By} & -l_{Ay}G^*_{By} & -G_{Ay}l^*_{By} & G_{Ay}G^*_{By} \end{bmatrix} \begin{bmatrix} 1 & 1 & 0 & 0 \\ 0 & 0 & 1 & i \\ 0 & 0 & 1 & -i \\ 1 & -1 & 0 & 0 \end{bmatrix} \begin{bmatrix} I \\ Q \\ U \\ V \end{bmatrix}.$$

Expanding and rearranging, we obtain expressions for the observed Stokes fluxes I', Q', U' & V', given antennas with feed Jones matrices $\mathrm{J_A}$ & $\mathrm{J_B}$ and source Stokes fluxes I, Q, U & V.

$$\begin{aligned} I' = \frac{1}{2}[&(G_{Ax}G^*_{Bx} + l_{Ax}l^*_{Bx} + l_{Ay}l^*_{By} + G_{Ay}G^*_{By})I + (G_{Ax}G^*_{Bx} - l_{Ax}l^*_{Bx} + l_{Ay}l^*_{By} - G_{Ay}G^*_{By})Q \\ &+ (G_{Ax}l^*_{Bx} + l_{Ax}G^*_{Bx} - l_{Ay}G^*_{By} - G_{Ay}l^*_{By})U + (iG_{Ax}l^*_{Bx} - il_{Ax}G^*_{Bx} - il_{Ay}G^*_{By} + iG_{Ay}l^*_{By})V] \end{aligned} \tag{A.1}$$

$$\begin{aligned} Q' = \frac{1}{2}[&(G_{Ax}G^*_{Bx} + l_{Ax}l^*_{Bx} - l_{Ay}l^*_{By} - G_{Ay}G^*_{By})I + (G_{Ax}G^*_{Bx} - l_{Ax}l^*_{Bx} - l_{Ay}l^*_{By} + G_{Ay}G^*_{By})Q \\ &+ (G_{Ax}l^*_{Bx} + l_{Ax}G^*_{Bx} + l_{Ay}G^*_{By} + G_{Ay}l^*_{By})U + (iG_{Ax}l^*_{Bx} - il_{Ax}G^*_{Bx} + il_{Ay}G^*_{By} - iG_{Ay}l^*_{By})V] \end{aligned} \tag{A.2}$$

$$\begin{aligned} U' = \frac{1}{2}[&(-G_{Ax}l^*_{By} + l_{Ax}G^*_{By} - l_{Ay}G^*_{Bx} + G_{Ay}l^*_{Bx})I + (-G_{Ax}l^*_{By} - l_{Ax}G^*_{By} - l_{Ay}G^*_{Bx} - G_{Ay}l^*_{Bx})Q \\ &+ (G_{Ax}G^*_{By} - l_{Ax}l^*_{By} - l_{Ay}l^*_{Bx} + G_{Ay}G^*_{Bx})U + (iG_{Ax}G^*_{By} + il_{Ax}l^*_{By} - il_{Ay}l^*_{Bx} - iG_{Ay}G^*_{Bx})V] \end{aligned} \tag{A.3}$$

$$\begin{aligned} V' = \frac{-i}{2}[&(-G_{Ax}l^*_{By} + l_{Ax}G^*_{By} + l_{Ay}G^*_{Bx} - G_{Ay}l^*_{Bx})I + (-G_{Ax}l^*_{By} - l_{Ax}G^*_{By} + l_{Ay}G^*_{Bx} + G_{Ay}l^*_{Bx})Q \\ &+ (G_{Ax}G^*_{By} - l_{Ax}l^*_{By} + l_{Ay}l^*_{Bx} - G_{Ay}G^*_{Bx})U + (iG_{Ax}G^*_{By} + il_{Ax}l^*_{By} + il_{Ay}l^*_{Bx} + iG_{Ay}G^*_{Bx})V] \end{aligned} \tag{A.4}$$

APPENDIX B

Musings on beam models

In a perfect world, a beam model of any receiving element perfectly reproduces the variation of sensitivity across the sky at all frequencies of interest. The phased-array receiving elements of the MWA are constructed from a set of simple dipoles which are coherently summed. This can be described by an array factor, AF,

$$AF = \sum_{n=1}^{N} w_n exp[i(k_x x_n + k_y y_n)], \tag{B.1}$$

where w_n is a complex weight applied to each dipole, x_n, y_n are Cartesian coordinates of dipole n from the centre of the tile, otherwise known as the the instrument frame. Directional cosines k_x, k_y are defined in spherical coordinates as:

$$\begin{aligned} k_x &= \frac{2\pi}{\lambda}\sin\theta\sin\phi, \\ k_y &= \frac{2\pi}{\lambda}\sin\theta\cos\phi, \end{aligned} \tag{B.2}$$

where θ, ϕ are zenith angle and azimuth respectively. Multiplying the Array Factor by the response of a single dipole on a ground screen results in an analytic representation of the full MWA tile (described by Balanis, 2016):

$$B_{\mathrm{MWA}} = AF \times B_{\mathrm{dipole}}, \tag{B.3}$$

where B_{MWA} is the beam response of the phased-array MWA tile, AF is the array factor, and the beam response of a single, simple dipole on a ground screen B_{dipole} is typically well characterised, and varies smoothly with frequency. For a regular array of dipoles, such as in the MWA, the array factor can have a strong frequency dependence, leading to a highly chromatic beam model.

The physical reality of a closely packed array of dipoles is that they interact with each other in a non-trivial manner, leading to a deviation from the simple analytic beam model described in Equation B.3. Signals reflected off one dipole can be absorbed by a neighbouring one, and potentially even fractionally re-transmitted - an effect known as mutual coupling. Further, signals reflected off one dipole, can be received by orthogonally polarised dipole, leading to polarisation leakage. Mutual coupling can also introduce frequency dependent effects when resonances in couplings between dipoles occur at particular frequencies.

The cutting-edge Fully-Embedded-Element (FEE) MWA beam model was generated with numerical electromagnetic simulations (Sokolowski et al., 2017; Sutinjo et al., 2015). These simulations are computationally expensive and were only performed at a 1.28 MHz frequency resolution over the MWA band. Any line-of-sight on the sky thus experiences a step-response as a function of frequency. Figure B.1 shows the response of once cross-sectional slice (azimuth=0, zenith angle=$\{0 : 90°\}$) of the FEE beam model, across the MWA high-band ($167 - 197$ MHz). In the upper left panel we observe the simulation frequency discontinuity as a noticeable vertical banding. To gauge the spectral structure encoded by the beam model, we perform a Fourier transform across frequency. This decomposes the beam power as a function of delay modes and is shown in the upper right panel of Figure B.1, with the sharp vertical aliasing arising from the 1.28 MHz frequency resolution. Daniel Ung* has developed a frequency interpolated MWA beam model, which has a much smoother chromatic response. The bottom panels of Figure B.1 repeat the analysis in the upper panels, using the frequency interpolated FEE beam model. The vertical banding and delay aliasing has now been suppressed by the smoother frequency response.

The impact of the non-continuous frequency response of the original FEE beam model is best observed in 2D power spectrum space. We perform a `hyperdrive` (Jordan et, al,. submitted) simulation of 30,000 foreground sources from the LoBES catalogue (Lynch et al., 2021) with both the the FEE and the interpolated FEE beam model, with power spectrum estimation performed using `CHIPS`(Trott et al., 2016). The results of the simulations are shown in Figure B.2, with clear coarse-band harmonics appearing horizontally in the simulations of the FEE model (panel (i)), which are absent in the simulations using the interpolated FEE model (panel (ii)). These simulations demonstrate the necessity of instrumental primary beams with smooth frequency variation, and crucially, instrumental beam models of high fidelity, which capture all actual frequency characteristics.

*https://www.researchgate.net/profile/Daniel-Ung-2

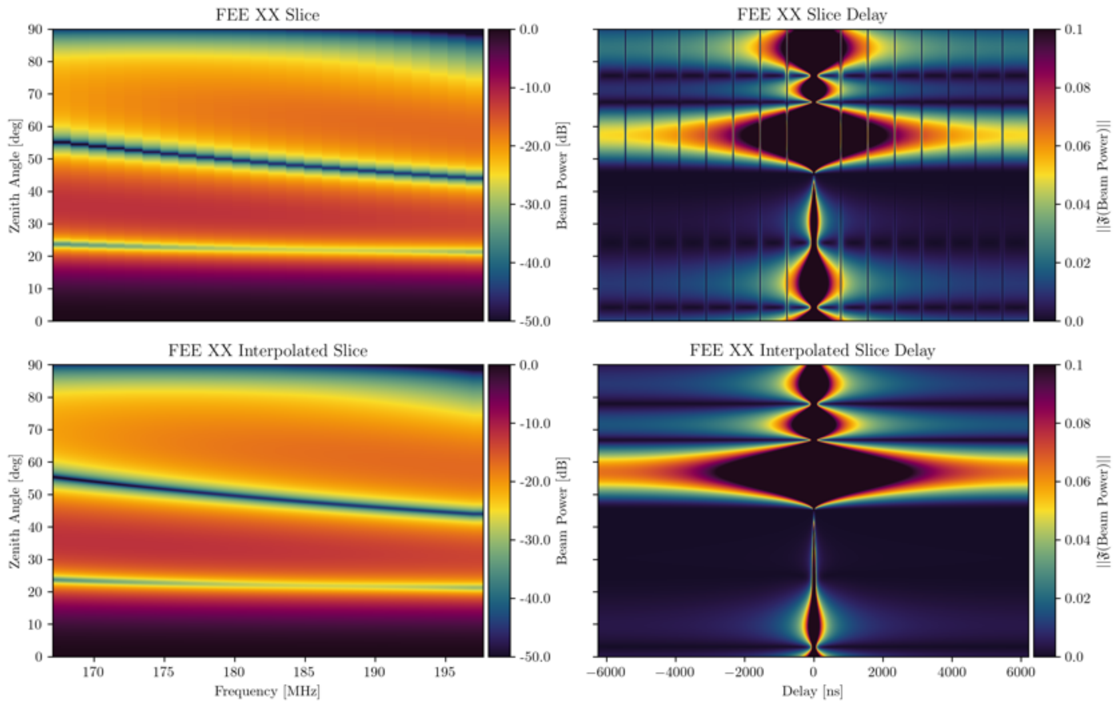

Figure B.1: An investigation into the frequency structure in the FEE beam model. A slice (along azimuth=0, zenith angle={0 : 90°}) of the X (East-West) polarisation of the FEE beam response in the MWA high band (167 – 197 MHz). The upper left panel shows beam power of the FEE model as a function of frequency, displaying marked vertical banding from the 1.28 MHz resolution. The upper right panel shows the the delay transformation of beam power, with sharp vertical aliasing arising from the frequency resolution. The two lower panels repeat the analysis of the upper panels with a frequency interpolated FEE beam model, displaying a much smoother frequency structure.

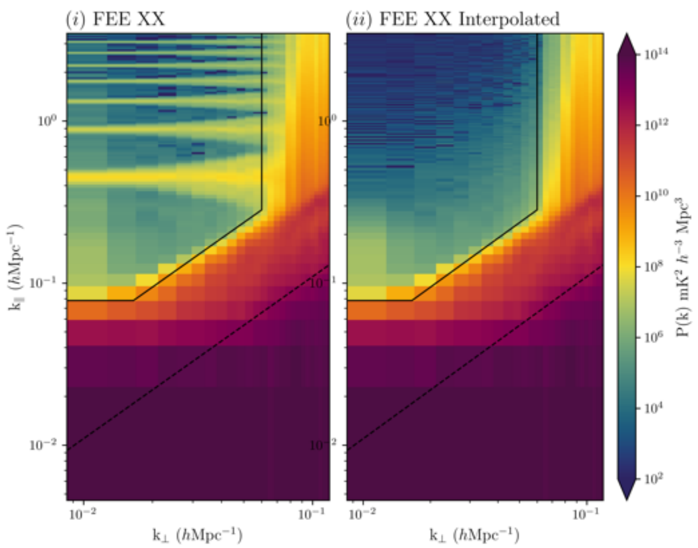

Figure B.2: A power spectrum analysis of 30000 LoBES sources using the FEE model (panel (i)), and the interpolated FEE model (panel (ii)), where XX represents East-West oriented dipoles. Clear coarse-band harmonics are visible in the simulation with the FEE beam model due to the 1.28 MHz frequency resolution.

References

Aghanim N., Desert F. X., Puget J. L., Gispert R., 1996, Astronomy and Astrophysics, 311, 1

Alpher R. A., Bethe H., Gamow G., 1948, Physical Review, 73, 803

Asad K. M. B., et al., 2015, Monthly Notices of the Royal Astronomical Society, 451, 3709

Asad K. M. B., et al., 2016, Monthly Notices of the Royal Astronomical Society, 462, 4482

Asad K. M. B., Koopmans L. V. E., Jelić V., de Bruyn A. G., Pandey V. N., Gehlot B. K., 2018, Monthly Notices of the Royal Astronomical Society, 476, 3051

Balanis C. A., 2016, Antenna theory: analysis and design. John wiley & sons

Barry N., Hazelton B., Sullivan I., Morales M. F., Pober J. C., 2016, Monthly Notices of the Royal Astronomical Society, 461, 3135

Barry N., Beardsley A. P., Byrne R., Hazelton B., Morales M. F., Pober J. C., Sullivan I., 2019a, Publications of the Astronomical Society of Australia, 36, e026

Barry N., et al., 2019b, The Astrophysical Journal, 884, 1

Barry N., Line J. L. B., Lynch C. R., Kriele M., Cook J., 2024, The Astrophysical Journal, 964, 158

Beardsley A. P., et al., 2012, Monthly Notices of the Royal Astronomical Society, 425, 1781

Beardsley A. P., et al., 2016, The Astrophysical Journal, 833, 102

Beardsley A. P., et al., 2019a, Publications of the Astronomical Society of Australia, 36, e050

Beardsley A. P., et al., 2019b, Publications of the Astronomical Society of Australia, 36, e050

Becker G. D., Bolton J. S., Madau P., Pettini M., Ryan-Weber E. V., Venemans B. P., 2015, Monthly Notices of the Royal Astronomical Society, 447, 3402

Berger P., et al., 2016, Ground-based and Airborne Telescopes VI

Bernardi G., et al., 2013, The Astrophysical Journal, 771, 105

Bolli P., Pupillo G., Paonessa F., Virone G., Wijnholds S. J., Lingua A. M., 2018, IEEE Antennas and Wireless Propagation Letters, 17, 613

Bowman J. D., et al., 2007, The Astronomical Journal, 133, 1505

Bowman J. D., Morales M. F., Hewitt J. N., 2009, The Astrophysical Journal, 695, 183

Bowman J. D., et al., 2013, Publications of the Astronomical Society of Australia, 30, e031

Brentjens M. A., de Bruyn A. G., 2005, Astronomy & Astrophysics, 441, 1217–1228

Briggs D. S., 1995, in American Astronomical Society Meeting Abstracts. p. 112.02

Burn B. J., 1966, Monthly Notices of the Royal Astronomical Society, 133, 67

Byrne R., et al., 2019, The Astrophysical Journal, 875, 70

Byrne R., Morales M. F., Hazelton B., Sullivan I., Barry N., Lynch C., Line J. L. B., Jacobs D. C., 2022, Monthly Notices of the Royal Astronomical Society, 510, 2011

Cakaj S., Fischer M., Scholtz A., 2009, Practical horizon plane for low earth orbiting (LEO) satellite ground stations. Wseas, pp 62–67, https://www.researchgate.net/publication/262216867_Practical_horizon_plane_for_low_earth_orbiting_LEO_satellite_ground_stations

Chang C., Monstein C., Refregier A., Amara A., Glauser A., Casura S., 2015, Publications of the Astronomical Society of the Pacific, 127, 1131

Chokshi A., b. Line J. L., McKinley B., 2020, Journal of Open Source Software, 5, 2629

Chokshi A., Line J. L. B., Barry N., Ung D., Kenney D., McPhail A., Williams A., Webster R. L., 2021, Monthly Notices of the Royal Astronomical Society, 502, 1990–2004

Chokshi A., Barry N., Line J. L. B., Jordan C. H., Pindor B., Webster R. L., 2024, The Necessity of Individually Validated Beam Models for an Interferometric Epoch of Reionization Detection (arXiv:2409.19875), doi:10.48550/arXiv.2409.19875

Choudhuri S., Bull P., Garsden H., 2021, Monthly Notices of the Royal Astronomical Society, 506, 2066

Condon J. J., Ransom S. M., 2016, Essential Radio Astronomy, sch - school edition edn. Princeton University Press, http://www.jstor.org/stable/j.ctv5vdcww

Cook J. H., Trott C. M., Line J. L. B., 2022, MNRAS, 514, 790

Datta A., Bowman J. D., Carilli C. L., 2010, The Astrophysical Journal, 724, 526

DeBoer D. R., et al., 2017, Publications of the Astronomical Society of the Pacific, 129, 045001

Di Matteo T., Perna R., Abel T., Rees M. J., 2002, The Astrophysical Journal, 564, 576

Eastwood M. W., et al., 2019, The Astronomical Journal, 158, 84

Feynman R. P., 1965, Feynman lectures on physics. Volume 3: Quantum mechancis. California Institute of Technology

Fixsen D. J., 2009, The Astrophysical Journal, 707, 916

Foreman-Mackey D., Hogg D. W., Lang D., Goodman J., 2013, Publications of the Astronomical Society of the Pacific, 125, 306–312

Furlanetto S. R., Oh S. P., Briggs F. H., 2006, Physics Reports, 433, 181

Geil P. M., Gaensler B. M., Wyithe J. S. B., 2011, Monthly Notices of the Royal Astronomical Society, 418, 516

Goldenberg H. M., Kleppner D., Ramsey N. F., 1960, Phys. Rev. Lett., 5, 361

Gorski K. M., Hivon E., Banday A. J., Wandelt B. D., Hansen F. K., Reinecke M., Bartelmann M., 2005, The Astrophysical Journal, 622, 759

Grazian A., et al., 2018, Astronomy and Astrophysics, 613, A44

Greig B., Wyithe J. S. B., Murray S. G., Mutch S. J., Trott C. M., 2022, Monthly Notices of the Royal Astronomical Society, 516, 5588

van Haarlem M. P., et al., 2013, Astronomy & Astrophysics, 556, A2

Hamaker J. P., Bregman J. D., Sault R. J., 1996, Astronomy and Astrophysics Supplement Series, 117, 137

Haslam C. G. T., Klein U., Salter C. J., Stoffel H., Wilson W. E., Cleary M. N., Cooke D. J., Thomasson P., 1981, Astronomy and Astrophysics, 100, 209

Hazelton B. J., Morales M. F., Sullivan I. S., 2013, The Astrophysical Journal, 770, 156

Heald G., 2009, in Strassmeier K. G., Kosovichev A. G., Beckman J. E., eds, Vol. 259, Cosmic Magnetic Fields: From Planets, to Stars and Galaxies. pp 591–602, doi:10.1017/S1743921309031421

Herman L., et al., 2024, arXiv e-prints, p. arXiv:2407.00856

Hinton S. R., 2016, The Journal of Open Source Software, 1, 00045

Hubble E., 1929, Proceedings of the National Academy of Science, 15, 168

Hurley-Walker N., et al., 2014, Publications of the Astronomical Society of Australia, 31, e045

Hurley-Walker N., et al., 2017, Monthly Notices of the Royal Astronomical Society, 464, 1146

Jacobs D. C., et al., 2017, Publications of the Astronomical Society of the Pacific, 129, 035002

Jelić V., et al., 2008, Monthly Notices of the Royal Astronomical Society, 389, 1319

Joseph R. C., Trott C. M., Wayth R. B., 2018, The Astronomical Journal, 156, 285

Joseph R. C., Trott C. M., Wayth R. B., Nasirudin A., 2019, Monthly Notices of the Royal Astronomical Society, 492, 2017

Kamionkowski M., Kosowsky A., 1999, Annual Review of Nuclear and Particle Science, 49, 77

Kim H., et al., 2022, The Astrophysical Journal, 941, 207

Kohn S. A., et al., 2016, The Astrophysical Journal, 823, 88

Kohn S. A., et al., 2019, The Astrophysical Journal, 882, 58

Koopmans L., et al., 2015, Advancing Astrophysics with the Square Kilometre Array (AASKA14), p. 1

Lemaître G., 1927, Annales de la Société Scientifique de Bruxelles, 47, 49

Lenc E., et al., 2017, Publications of the Astronomical Society of Australia, 34, e040

Lenc E., Murphy T., Lynch C. R., Kaplan D. L., Zhang S. N., 2018, Monthly Notices of the Royal Astronomical Society, 478, 2835

Line J. L. B., et al., 2018, Publications of the Astronomical Society of Australia, 35, e045

Line J. L. B., et al., 2020, Publications of the Astronomical Society of Australia, 37

Liu A., Parsons A. R., Trott C. M., 2014a, Physical Review D, 90, 023018

Liu A., Parsons A. R., Trott C. M., 2014b, Physical Review D, 90, 023019

Lynch C. R., et al., 2021, Publications of the Astronomical Society of Australia, 38, e057

Madau P., Haardt F., 2015, The Astrophysical Journal Letters, 813, L8

Mao Y., Tegmark M., McQuinn M., Zaldarriaga M., Zahn O., 2008, Physical Review D, 78, 023529

Mellema G., et al., 2013, Experimental Astronomy, 36, 235

Mesinger A., ed. 2019, The Cosmic 21-cm Revolution. 2514-3433, IOP Publishing, doi:10.1088/2514-3433/ab4a73, `https://dx.doi.org/10.1088/2514-3433/ab4a73`

Mesinger A., Ferrara A., Greig B., Iliev I., Mellema G., Pritchard J., Santos M., 2015, in Advancing Astrophysics with the Square Kilometre Array (AASKA14). p. 11 (`arXiv:1501.04106`), doi:10.22323/1.215.0011

Mitchell D. A., Greenhill L. J., Wayth R. B., Sault R. J., Lonsdale C. J., Cappallo R. J., Morales M. F., Ord S. M., 2008, IEEE Journal of Selected Topics in Signal Processing, 2, 707

Morales M. F., Hewitt J., 2004, The Astrophysical Journal, 615, 7

Morales M. F., Wyithe J. S. B., 2010, Annual Review of Astronomy and Astrophysics, 48, 127

Morales M. F., Hazelton B., Sullivan I., Beardsley A., 2012, The Astrophysical Journal, 752, 137

Morgan J. S., Macquart J.-P., Chhetri R., Ekers R. D., Tingay S. J., Sadler E. M., 2019, Publications of the Astronomical Society of Australia, 36

Morrison I. S., et al., 2023, Publications of the Astronomical Society of Australia, 40, e019

Munshi S., et al., 2024, Astronomy and Astrophysics, 681, A62

Neben A., et al., 2015, Radio Science, 50, 614

Neben A. R., et al., 2016a, The Astrophysical Journal, 820, 44

Neben A. R., et al., 2016b, The Astrophysical Journal, 826, 199

Newburgh L. B., et al., 2014, Ground-based and Airborne Telescopes V

Ninni P. D., Bolli P., Paonessa F., Pupillo G., Virone G., Wijnholds S. J., 2020, in 2020 14th European Conference on Antennas and Propagation (EuCAP). pp 1–5, doi:10.23919/EuCAP48036.2020.9135792

Nunhokee C. D., et al., 2020, The Astrophysical Journal, 897, 5

Offringa A. R., Smirnov O., 2017, MNRAS, 471, 301

Offringa A. R., McKinley B., Hurley-Walker et al., 2014, MNRAS, 444, 606

Oh S. P., Mack K. J., 2003, Monthly Notices of the Royal Astronomical Society, 346, 871

Ord S. M., et al., 2015, Publications of the Astronomical Society of Australia, 32, e006

Orosz N., Dillon J. S., Ewall-Wice A., Parsons A. R., Thyagarajan N., 2019, Monthly Notices of the Royal Astronomical Society, 487, 537–549

Paonessa F., Ciorba L., Virone G., Bolli P., Magro A., McPhail A., Minchin D., Bhushan R., 2020, in 2020 XXXIIIrd General Assembly and Scientific Symposium of the International Union of Radio Science. pp 1–3, doi:10.23919/URSIGASS49373.2020.9232190

Park J., Mesinger A., Greig B., Gillet N., 2019, Monthly Notices of the Royal Astronomical Society, 484, 933

Parsons A. R., Pober J. C., Aguirre J. E., Carilli C. L., Jacobs D. C., Moore D. F., 2012, The Astrophysical Journal, 756, 165

Patil A. H., et al., 2016, Monthly Notices of the Royal Astronomical Society, 463, 4317

Patil A. H., et al., 2017, The Astrophysical Journal, 838, 65

Penzias A. A., Wilson R. W., 1965, The Astrophysical Journal, 142, 419

Pindor B., Wyithe J. S. B., Mitchell D. A., Ord S. M., Wayth R. B., Greenhill L. J., 2011, Publications of the Astronomical Society of Australia, 28, 46

Planck Collaboration et al., 2016, Astronomy and Astrophysics, 594, A13

Planck Collaboration et al., 2020, Astronomy and Astrophysics, 641, A6

Pober J. C., et al., 2012, The Astronomical Journal, 143, 53

Pober J. C., et al., 2013, The Astrophysical Journal Letters, 768, L36

Pober J. C., et al., 2014, The Astrophysical Journal, 782, 66

Pober J. C., et al., 2016, The Astrophysical Journal, 819, 8

Pritchard J., Loeb A., 2012, Reports on progress in physics. Physical Society (Great Britain), 75, 086901

Rahimi M., et al., 2021, Monthly Notices of the Royal Astronomical Society, 508, 5954

Rand R. J., Lyne A. G., 1994, Monthly Notices of the Royal Astronomical Society, 268, 497

Remazeilles M., Dickinson C., Banday A. J., Bigot-Sazy M. A., Ghosh T., 2015, Monthly Notices of the Royal Astronomical Society, 451, 4311

Rhodes B., 2019, Skyfield: High precision research-grade positions for planets and Earth satellites generator (ascl:1907.024)

Riseley C. J., et al., 2018, Publications of the Astronomical Society of Australia, 35

Riseley C. J., et al., 2020, Publications of the Astronomical Society of Australia, 37

Robertson B., et al., 2024, The Astrophysical Journal, 970, 31

Salvini S., Wijnholds S. J., 2014, Astronomy and Astrophysics, 571, A97

Santos M. G., Cooray A., Knox L., 2005, The Astrophysical Journal, 625, 575

Shaver P. A., Windhorst R. A., Madau P., de Bruyn A. G., 1999, Astronomy and Astrophysics, 345, 380

Sokolowski M., et al., 2017, Publications of the Astronomical Society of Australia, 34, e062

Sokolowski M., et al., 2024, Publications of the Astronomical Society of Australia, 41, e011

Sridhar S. S., Heald G., van der Hulst J. M., 2018, cuFFS: A GPU-accelerated code for Fast Faraday Rotation Measure Synthesis (arXiv:1810.06250)

Sullivan I. S., et al., 2012, The Astrophysical Journal, 759, 17

Sutinjo A. T., O'Sullivan J., Lenc E., Wayth R. B., Padhi S., Hall P. A., Tingay S. J., 2015, Radio Science, 50, 52

Thyagarajan N., Helfand D. J., White R. L., Becker R. H., 2011, The Astrophysical Journal, 742, 49

Thyagarajan N., et al., 2013, The Astrophysical Journal, 776, 6

Thyagarajan N., et al., 2015, The Astrophysical Journal, 804, 14

Tingay S. J., et al., 2013, Publications of the Astronomical Society of Australia, 30, e007

Trott C. M., Wayth R. B., 2016, Publications of the Astronomical Society of Australia, 33, e019

Trott C. M., Wayth R. B., Tingay S. J., 2012, The Astrophysical Journal, 757, 101

Trott C. M., et al., 2016, The Astrophysical Journal, 818, 139

Trott C. M., et al., 2020, Monthly Notices of the Royal Astronomical Society, 493, 4711

Vedantham H., Udaya Shankar N., Subrahmanyan R., 2012, The Astrophysical Journal, 745, 176

Virone G., et al., 2014, IEEE Antennas and Wireless Propagation Letters, 13, 169

Wayth R. B., et al., 2015, Publications of the Astronomical Society of Australia, 32, e025

Wayth R. B., et al., 2018, Publications of the Astronomical Society of Australia, 35, e033

Wilensky M. J., et al., 2024, arXiv e-prints, p. arXiv:2403.13769

Yatawatta S., et al., 2013, Astronomy and Astrophysics, 550, A136

Zarka P., et al., 2020, in 2020 URSI General Assembly and Scientific Symposium.